Università
Ca'Foscari
Venezia

Dottorato di Ricerca in Science and Management of Climate Change

Scuola di dottorato in Global Change Science and Policy

A.A. 2010–2011

23° ciclo

Tropical Extratropical Interaction and Systematic Errors of Climate Models

Settore Scientifico-disciplinare di afferenza: FIS/06

Tesi di dottorato di **GIUSEPPE ZAPPA**, matricola 955468

Direttore della Scuola di dottorato
Prof. C. GIUPPONI

Tutori del dottorando
Dr. A. NAVARRA

Dr. V. LUCARINI

Abstract

The nature of the quasi-stationary waves (QSW) observed in an aquaplanet model, which consists of an Atmospheric General Circulation Model (AGCM) whose lower boundary is given by a swamp ocean, is investigated in detail. In this experimental setting, using Hayashi spectra of atmospheric energetics, QSW are identified as being marginally stable baroclinic waves. This novel theoretical paradigm is then applied for studying QSW in the real world. NCEP-DOE reanalysis reveals that a coherent QSW, of zonal wavenumber four, forms in the Southern Hemisphere austral summer. Its growth seems to be favoured by El Nino tropical conditions, and mechanisms of interaction consistent with the aquaplanet theory are proposed. The ECHAM5 AGCM, set-up in AMIP configuration, does not satisfactorily reproduce the observed QSW activity, and its misrepresentation is analysed as a function of the systematic errors of the model. The role played by the model resolution for better capturing QSW is extensively discussed.

Contents

Chapter 1

Introduction

1.1 Aim of the thesis

Climate is defined by the statistical properties of the climate system, which – in its most complete definition – is composed by a set of non linearly mutually interacting subsystems: the atmosphere, the ocean, the cryosphere and the biosphere (Peixoto and Oort, 1992). The scientific interest of studying climate and the necessity of understanding how the Earth's climate can be modified by increasing levels of greenhouse gases led, during the last decades, to the development of comprehensive numerical models of the Earth climate, nowadays called Earth System Models. By representing the fundamental physical processes characterising each subsystem as a set of discretised differential equations, Earth System Models are the most realistic tools we have for investigating the dynamics of the present climate and its changes in future scenarios. But despite their progressive development, which has been obtained by increasing the model resolution, by representing more physical processes, and by improving the model numerics, state of the art climate models still feature relevant systematic errors that refer to differences between the simulated and the observed climate statistics (Randall et al., 2007).

At least three different classes of metrics can be considered in measuring

the error committed by climate models. First of all, metrics can evaluate the *morphology* of climate which is defined by the spatial distribution of the statistics (including mean, variances and covariances) of basic climate parameters (Boer, 2000). While this approach allows to objectively identify systematic errors of models, it can unlikely point to the source of the error, as little insight is gathered on the physical processes which are actually misrepresented. A more general picture can be instead obtained by analysing climate budgets, which deal with the sources, the sinks and the transport of quantities in the atmosphere and in the ocean (Boer and Lambert, 2008; Lucarini and Ragone, 2010). These metrics evaluate how models are representing the energy, the water and the angular momentum cycles, so that they provide a rigorous physically based description of the climate system. A third approach is based on the analysis of how specific processes (e.g. Madden Julian Oscillation (MJO), El Nino Southern Oscillation (ENSO), storm tracks) are effectively simulated in the models (Lin et al., 2006; Lin, 2007; Catto et al., 2010). A good knowledge of the physical mechanisms characterising their dynamics is important for identifying errors that can affect their simulation, and for determining whether the right climate could be accidentally simulated because of the wrong reasons (Held, 2005). Simplified climate models can be important in this purpose. By setting a specific climate process in an idealised experimental setting, where only the more important dynamical mechanisms participating to the process are retained, simplified models allow to test and formulate theories which satisfyingly captures the essential properties of the process (Hoskins and Karoly, 1981; Valdes and Hoskins, 1989; Schneider, 2004; Held, 2005; Frierson et al., 2006; Lucarini et al., 2007).

This thesis aims to increase the theoretical understanding with regard to the generation of atmospheric quasi–stationary wave activity, and to apply the theoretical results for analysing the error committed by an Atmospheric General Circulation Model (AGCM). With the term *quasi–stationary* we refer to waves with a circumglobal character, featuring an almost zero phase velocity and maintaining coherence for a timescale of at least one month. The

matter is of interest because quasi stationary patterns (Salby, 1982; Branstator, 2002) are often responsible for the maintenance of states of perturbed weather lasting for a sufficiently long time to cause highly damaging floods or droughts. For instance, the summer 2007 featured the recursive formation of a quasi–stationary circumglobal pattern including a cyclonic circulation west of Europe (Blackburn et al., 2008), which caused important floods in the UK. Considering their potential impact on the human society, increasing the understanding about these quasi–stationary features is a relevant topic of climate science and of some importance for evaluating how they might be modified under climate change scenarios.

1.1.1 Methodology

We've first of all developed a theoretical framework for interpreting the formation of quasi–stationary wave patterns and we've identified mechanisms responsible for their maintenance. As previously discussed, simplified models can be useful for this purpose. We've therefore set up an aquaplanet model, which consists of an AGCM set in a zonally symmetric ocean covered world, and we've analysed the quasi–stationary patterns forming in this simplified experimental setting. The development of a self consistent theory of quasi–stationary waves is in fact complicated by the number of different, but interacting, processes that can underlie its dynamics. Many of these mechanisms, as the baroclinic–orographic resonance via the form drag (Benzi et al., 1986; Ruti et al., 2006), the barotropic instability of the stationary waves (Simmons et al., 1983), and the Rossby wave radiation from anomalous tropical convection (Hoskins and Karoly, 1981), require the presence of zonal asymmetries in the forcing of the mean state. But quasi–stationary waves are also observed in models with zonally symmetric boundary conditions (Hendon and Hartmann, 1985; Watanabe, 2005), where for Earth–like equator to pole Sea Surface Temperature (SST) differences, they manifest in the form of peculiar waves of zonal wavenumber five. The aquaplanet model can therefore be an ideal simplified tool for investigating the statistical properties and the

energetics of quasi–stationary patterns that are internally generated by the atmospheric dynamics. A brief introduction to the AGCM that is adopted for performing the experiments discussed in the thesis is given in chapter 2.

A spectral representation of the Lorenz energy cycle (Lorenz, 1967; Hayashi, 1980) is introduced for identifying the organisation of spectral power along privileged dispersion relations and for evaluating the stability properties of atmospheric waves as a function of their frequency, zonal wavenumber and meridional scale. Using this method, we will highlight the limitations of the Rossby wave paradigm that is usually adopted for studying this typology of waves in aquaplanet models. In particular, we will show that a baroclinic theory can be of deeper interpretative value. The dynamics and the energetics of quasi–stationary waves in the aquaplanet model and their interaction with the tropical convection is thoroughly treated in chapters 3 and 4.

In chapter 5, we then use the methodologies and the theory developed in the aquaplanet to look for analogous atmospheric patterns forming in the Earth's climate. The analysis is based on reanalyses data and it is focused on the Southern Hemisphere austral summer. The hemisphere and the season are chosen because featuring the climate with the highest degree of zonal symmetry, so that a comparison with the aquaplanet can be more easily established. A pattern projecting on the zonal wavenumber four is successfully identified. The growth of the pattern and its overall intensity features a strong interannual variability, which is interpreted using the baroclinic theory developed for the quasi–stationary waves observed in the aquaplanet model.

We finally move to examining if a climate model setup in AMIP[1] configuration is able to correctly simulate the quasi stationary baroclinic pattern identified in reanalyses during Southern Hemisphere austral summer. We find that the errors of the model lead to an unsatisfying representation of this process. In particular, the simulated quasi–stationary wave activity features a different spatial scale, horizontal structure and energetics respect

[1] Atmospheric Model Intercomparison Project (AMIP). The project proposes a model setup and a set of boundary conditions for simulating the Earth's climate with an AGCM.

to the one pictured in reanalyses data. The misrepresentation of the quasi–stationary wave activity is put in relation to the systematic error in the mean state and in the energetics of extratropical baroclinic processes of the model. The sensitivity of the errors to the model resolution is investigated in detail. These topics are all covered in chapter 6, while the conclusions are finally given in chapter 7.

In the remaining part of this chapter, fundamental aspects of the general circulation of the atmosphere, that are necessary for understanding the rest of the thesis, will be briefly discussed. The listings of the adopted notations and of the acronyms are reported in Appendix A and B, respectively.

1.2 The time mean state of the atmosphere

Finding qualitative and quantitative explanations for the observed time mean state of the atmosphere is a major issue in the understanding of the general circulation of the atmosphere (Lorenz, 1967; Stone, 1978; Schneider, 2004). Apart from its purely scientific interest, the formulation of appropriate theories and methodologies that explain how the atmospheric mean state is actually maintained is of practical value for evaluating the errors of climate models (Lucarini and Ragone, 2010).

A useful approach for studying the mean state of the atmosphere consists in the separate research of theories explaining the zonal mean circulation from those explaining the deviations from the zonal mean (eddy circulation). The decomposition between a mean and an eddy field is motivated by the following arguments. If the Earth had perfect zonally symmetric boundary conditions, because of the rotational symmetry of the system, it would necessarily feature a zonally symmetric climate. Therefore, the zonal asymmetries in the Earth boundary conditions are necessarily the ultimate reason of the zonal asymmetries in the observed time mean state, which are generally called *stationary waves*. The zonal mean circulation is instead depending on the net meridional transport of heat and momentum by the whole set of atmospheric

motions, which results as instabilities forced by the vertical and meridional distribution in the incoming solar radiation. Because stationary waves are only partially contributing to those transports (Peixoto and Oort, 1992), the physical processes maintaining the zonal mean and the eddy circulation are to a first order different, and the research of separated theories is justified.

1.2.1 The zonal mean circulation

The zonal mean state of the atmosphere is the most basilar climatic property of the atmospheric system, and it has been matter of investigation since the former studies of Halley, Hadley, Thompson and Ferrel who looked for a general theory that could explain, consistently with the laws imposed by fluid dynamics, why surface easterlies and westerlies were observed in the tropics and in the extratropics, respectively (see Lorenz (1967) for a description of these early theories).

Fig. 1.1 depicts the time averaged zonal mean meridional circulation (on the left side) and the structure of the zonal wind field (on the right side) as a function of latitude and height. The circulation in the meridional plane features three overturning cells, which are respectively named, moving from the equator to the pole, the Hadley, the Ferrel and the Polar cell. The Hadley cell is associated to rising air near the equator, poleward flow toward the poles in the upper troposphere and sinking in the subtropics, where an adiabatic warming leads to the formation of the high pressure systems associated to the subtropical deserts. The basic physical process maintaining this circulation, as will be later pointed in sec. 1.3.2, can be explained by zonally symmetric theories of the atmosphere (Held and Hou, 1980). This is untrue for the other two extratropical meridional cells, which are instead a direct consequence of the meridional heat and momentum transport accomplished by extratropical wave motions (Held, 2000). Baroclinic instability is recognised as the dominant process feeding energy in these disturbances (Eady, 1949), which are therefore generally referred to as *baroclinic waves*.

The zonal wind field is characterised by tropical surface easterly opposed

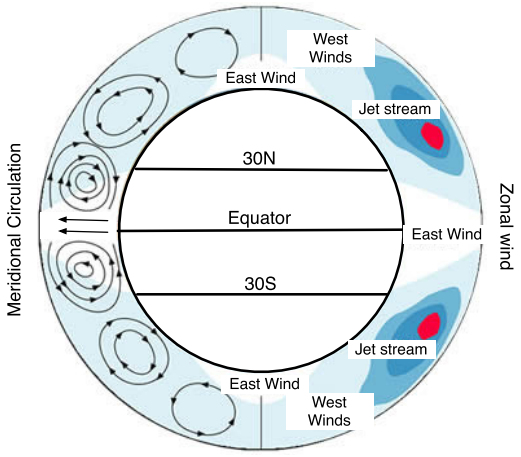

Figure 1.1: Schematic picture of the general circulation of the atmosphere. Adapted from a figure in the website of the bureau of meteorology of Australia: www.bom.gov.au

to extratropical westerlies, which are themselves organised in vertically coherent structures featuring maximum winds in the upper troposphere. These strong, upper tropospheric, westerlies are called *jet streams* and are located at the latitude band of highest average meridional temperature gradient. Weak surface easterlies are again found in the polar regions. Hadley (Lorenz, 1967) correctly realised that a proper interpretation of the surface wind distribution had to rely on considerations regarding the global atmospheric angular momentum cycle. Due to the drag exerted by the Earth surface on the air motions in the lowest layers of the atmosphere, tropical easterlies and extratropical westerlies represent respectively a source and a sink of atmospheric angular momentum. When long enough time averages are considered, the total angular momentum in every latitude band has to remain constant, which requires that atmospheric motions compensate the surface sources and sinks by meridionally redistributing momentum from the tropics to the extratropics. While the redistribution of momentum in the tropics is mainly accomplished by the Hadley cell circulation, extratropical waves provide essential transport in the extratropics (Peixoto and Oort, 1992), as angular

momentum converges toward the latitude where baroclinic waves are generated (Held, 2000).

Theories of the zonal mean circulation are therefore dependent on the theories of the non zonal wave motions, so that the study of the atmospheric mean state can't be really separated from the study of its variability. Section 1.4 will provide results from a linear baroclinic theory of extratropical waves which is able to qualitatively interpret their properties as a function of the spatial scale of the waves.

1.2.2 The stationary waves

The linkage between observed stationary wave patterns and the zonal asymmetries in the Earth boundary conditions have been investigated by a number of simplified models of the atmosphere (Valdes and Hoskins, 1989; Ting, 1994; Jin and Hoskins, 1995; Held et al., 2002). These studies found that latent heat released in the tropical convection, the latent and sensible heat released along the extratropical stormtracks, and the vorticity sources, that via the stretching of atmospheric columns, are created by the flows of air over orography, constitute the main forcing maintaining the observed stationary wave pattern. Moreover, Valdes and Hoskins (1989) has shown that even linearised atmospheric general circulation models can qualitatively reproduce the stationary wave pattern, provided that the observed zonal mean circulation is used as basic state and realistic heating and vorticity sources are used as forcing.

Rossby wave theory is the principal paradigm adopted for interpreting stationary waves, and the reason has to be researched on the kinematic and energetic properties of the Rossby wave (Hoskins and Karoly, 1981; Holton, 2004). It is a linear and neutral wave, so that it has to be maintained against dissipation by an external forcing, which can be provided by convective or by orographic vorticity sources. Moreover, the wave energy can propagate from the tropics to the extratropics, and its phase can remain stationary in a westerly basic state. The kinematics of Rossby waves is entirely described by

the conservation of the total (relative plus planetary) vorticity, assuming the vorticity budget is dominated by the vorticity advection by the zonal wind field, and the conversion between planetary and relative vorticity due to the β effect. Therefore, the simplest fluid dynamic configuration containing Rossby wave dynamics is that of a one layer (barotropic) fluid in a beta channel (Holton, 2004). In such simplified conditions, once the zonal wind of the basic state ($\bar{u}$) is given, the linear Rossby wave obeys to the following dispersion relation:

$$\omega = k\bar{u} - k\frac{\beta - \bar{u}_{yy}}{k^2 + l^2}, \tag{1.1}$$

where ω, k and l are respectively the angular frequency, the zonal and the meridional wave numbers of the wave, $\bar{u}_{yy}$ is the second derivative of u in the meridional direction and β is the meridional derivative of the planetary vorticity (f) at the central latitude of the channel. Therefore $\beta - \bar{u}_{yy}$ gives the meridional derivative of the absolute vorticity of the basic state. This theory has been extended to include spherical geometry (Hoskins and Karoly, 1981) and three dimensional baroclinic basic states (Held et al., 2002), so that it can be of practical value for the analysis of the Earth stationary wave patterns. While the inclusion of spherical geometry, which is accomplished by using Mercator coordinate system, does not particularly alter the structure of Eq. 1.1, a potentially relevant problem results by considering realistic three dimensional basic states. For Eq. 1.1 being valid, $\bar{u}$ has to be evaluated at an equivalent barotropic level, that is defined as the level where the vorticity sources due to the stretching term is zero. In the extratropics, this level is considered being close to the 400mb level (Held et al., 2002). On the contrary, the vorticity sources by tropical convection are principally concentrated near the top of convective clouds, which is approximately located at the 200mb level. This creates an ambiguity on what should be the proper level to be selected, and the 300mb level is considered as a satisfying compromise (Hoskins and Ambrizzi, 1993).

The total wave number of a Rossby wave which is stationary in a westerly

current can be found by imposing ($\omega = 0$) in Eq. 1.1:

$$K_s^2 = \frac{\beta - \bar{u}_{yy}}{\bar{u}} \sim \frac{\beta}{U} + \frac{1}{L^2}, \tag{1.2}$$

where $K_s = (k^2 + l^2)^{1/2}$ is called the *Rossby stationary wavenumber*. The scaling shown on the right side of Eq. 1.2, which is obtained considering $u_{yy} \sim (-U/L^2)$, is particularly useful when the basic state features a well defined zonal jet stream, so that U and L are the intensity and the characteristic meridional width of the jet, respectively. Using ray propagation theory and the Wentzel–Kramers–Brillouin–Jeffreys (WKBJ) approximation, the trajectory and the amplitude of Rossby waves can be determined as a function of the meridional distribution of K_s (Hoskins and Karoly, 1981). Moreover, Hoskins and Ambrizzi (1993) showed that meridional relative maxima in K_s indicate the presence of upper tropospheric wave guides, where stationary Rossby waves can zonally propagate with little meridional dispersion. In particular, wave guides are favoured by the presence of narrow jet streams, as the high value of L^{-2} contributes to the local enhancement of K_s (Ambrizzi and Hoskins, 1997).

1.3 Atmospheric Instabilities and the Meridional Overturning Circulation

To describe the processes that feed kinetic energy into atmospheric motions, it is instructive to discuss how an hypothetical atmosphere would be modified by the onset of the leading atmospheric instabilities and of the tropical Hadley circulation. The atmosphere is considered to start from an axisymmetric state, which means that the atmospheric fields feature no deviations from the zonal mean. Moreover, the initial state is assumed to feature no motions in the meridional plane (i.e $v = \omega = 0$, $u = u(\varphi, z)$), and to be in equilibrium with an incoming zonally uniform equinoctial radiation pattern. In every latitude band there would be an exact balance between the energy

lost by outgoing longwave radiation and the heat absorbed by surface fluxes[2]. Meridional atmospheric heat fluxes would conversely be zero.

Many qualitative aspects of the proposed axisymmetric state can be determined. The surface temperature T_s is expected to scale with the latitudinal profile of the incoming solar radiation, so that

$$T_s \sim \Delta_T \cos^2(\varphi), \tag{1.3}$$

where φ is the latitude and Δ_T an equator to pole SST difference. The vertical temperature profile would be itself in radiative equilibrium. The vertical structure of the zonal wind would be connected to the surface winds through thermal–wind balance, which relates the vertical shear of the zonal wind to the meridional temperature gradients (Holton, 2004). The surface zonal wind is undetermined, but can be set, under no–slip conditions, equal to zero at every latitude.

Under inviscid conditions, even in the absence of any circulation in the meridional plane, such a state would be a steady solution of the primitive equation of the atmosphere (see sec. 2.1). But would such an equilibrium be stable and apply to a slightly viscous atmosphere? It is possible to point to three different reasons making the answer negative.

1.3.1 Convection

The purely vertical radiative equilibrium is unstable respect to convection, which vertically redistributes heat until a radiative–convective equilibrium is reached (Holton, 2004). Convection is therefore of fundamental importance in maintaining the tropical atmospheric stratification. Moreover, the upper tropospheric divergent flux spreading out from regions of strong convective activity can maintain extratropical rotational flow in the form of a forced stationary Rossby wave (Sardeshmukh and Hoskins, 1988).

[2]The incoming solar radiation absorbed in the atmosphere has been for simplicity neglected in the reasoning

1.3.2 Hadley cell overturning

Let's now assume that angular momentum is allowed to disperse diffusively. Under axisymmetric conditions, however weak the diffusion, the Hide's theorem (Schneider, 2006) states that no parcel of air can feature an angular momentum higher than the one of a parcel of air standing motionless at the equator. This poses a constrain on the maximum allowable zonal wind speed and, due to the thermal wind balance, on the maximum temperature difference between the equator and the subtropics. In particular, the meridional distribution of the vertically averaged temperature in the tropics is constrained to decrease at most quartically with latitude (Schneider, 2006). But Eq. 1.3 implies that the tropical atmospheric temperature in radiative–convective equilibrium with the incoming solar radiation decreases quadratically with latitude. This violates the Hide's theorem. A thermally direct circulation, which is the previously mentioned Hadley cell, is necessary to meridionally redistribute heat from its ascending branch, which is adiabatically cooled, to the descending one, which is warmed, so that the meridional temperature gradient in the tropics is flattened and the vertical wind shear becomes at least consistent with the constrain imposed by the Hide's theorem.

1.3.3 Baroclinic instability

The steady state resulting after the adjustments due to the previous processes, is still featuring an axisymmetric circulation but it has a stronger vertical stratification and an Hadley circulation in the meridional plane. The meridional gradient of the vertically averaged temperature would be predominantly confined poleward of the subtropics. This axisymmetric state would result unstable respect to a characteristic wave instability of stratified rotating fluid with westerly vertical wind shear, which is called baroclinic instability. Baroclinic processes convert the potential energy associated to the meridional temperature gradient in the kinetic energy of eddy motions,

so that the previous axisymmetric circulation gets substituted by a chaotic wave–like regime (Lorenz, 1967). If a temporal average over a long enough time interval is taken, a zonally symmetric mean state would be recovered. But the mean state, as a result of the heat meridionally transported by baroclinic waves toward the pole, would feature a weaker meridional temperature gradient and a zonal jet stream which is displaced toward the pole respect to the previous axisymmetric state (Schneider, 2006).

1.4 Extratropical waves theory

The evolution of a typical extratropical baroclinic atmospheric disturbance attends a life cycle which can be pictured as composed by three stages: the baroclinic growth, the propagation and the final dissipation. While a description of the latter stage requires to consider the non–linear evolution of the disturbance (Simmons and Hoskins, 1978), insight into the first two stages can be obtained by a linear approach, which describes the disturbance as a linear wave growing and propagating over a given basic state. The suitability of a wave–oriented approach is confirmed by spectra analysis of atmospheric fields characterising extratropical dynamics. The power spectral density is in fact distributed along preferential regions of the spectral space (Dell'Aquila et al., 2005). This suggests the existence of implicit relations $\omega = \omega(k)$, which are the signature of dispersion relations due to baroclinic wave packet propagation.

Two valuables linear models of atmospheric waves are those introduced by Rossby and Eady (Eady, 1949). While the former, which was discussed in sec. 1.2, is the prototype of the neutral wave, the latter is the prototype of the baroclinic unstable wave. Differently from the barotropic Rossby model, the Eady model is based on three dimensional baroclinic equations. Its basic state features a constant meridional temperature gradient, and a zonal wind field with westerly shear in thermal wind balance with the temperature field. Such a basic state is necessary to provide the available potential energy reser-

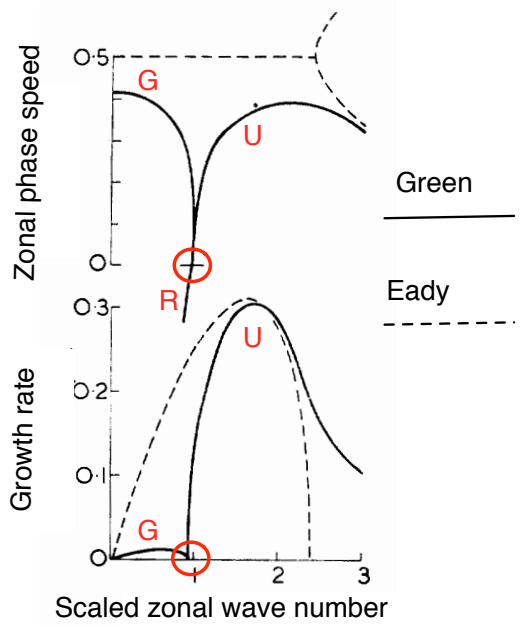

Figure 1.2: Phase speed and Growth rate of the normal modes of the Green's and the Eady's models as a function of the zonal wave number. The red circle refers to the marginally stable wavenumber that, in the Green's model, separates the branch of baroclinic unstable modes (indicated with U) and those of neutral Rossby waves (indicated R). (G) refers to the weakly unstable Green modes. As Rossby waves are neutral they only appear in the zonal phase speed diagram. Adapted from Green (1960)

voir which can be converted in the kinetic energy of the growing disturbance by baroclinic processes. In particular, the Eady model analyses the linear stability properties of a stratified rotating fluid, which is confined at the top and at the bottom between two parallel rigid surfaces in an f–channel. The meridional variation of the Coriolis parameter, namely the β effect, is in fact not necessary for generating unstable baroclinic modes.

Nonetheless, it is possible to frame simple models able to set in a common framework Rossby–like waves and unstable baroclinic waves. For instance, Green (1960) repeated the Eady's linear stability analysis in presence of the

β effect. Fig. 1.2 compares the growth rate and the phase speed of the most unstable waves in the Green's and in the Eady's model as a function of a scaled zonal wave number (k) of the wave. For values of k between one and two, waves are unstable in both the Green's and the Eady's models. The smaller phase speed in Green's model is the result of the conversion of planetary into relative vorticity which, similarly to Rossby wave dynamics, works to retard the eastward propagation of the disturbance. As k decreases, a very different behaviour is found. In the Eady model long waves are still unstable, while in the Green's model the unstable branch merges into a branch of westward propagating neutral Rossby waves. The transition between the two regimes, which is for clarity highlighted with a red circle in Fig. 1.2, occurs at a marginally stable wavenumber (K_c) that features zero growth rate and zero phase speed. Moreover, a secondary branch of weakly unstable eastward propagating waves (the Green modes), which differ from the main branch of instability in the vertical structure of the waves, is observed on $k < 1$. It is important to stress that the Eady model, which does not contain the beta effect and therefore the essential mechanism of Rossby wave dynamics, can't be of any interpretative value for describing the dynamics of baroclinic waves near the condition of marginal stability.

In the Green's model (Green, 1960), there is a fundamental non dimensional parameter (γ) that determines the stability property of the fluid:

$$\gamma = \frac{v\beta}{f\frac{\partial\omega}{\partial z}} \sim \frac{gBH^2\beta}{f^2\Delta_U}, \tag{1.4}$$

where $B = c_p\frac{\partial s}{\partial z}$ is a static stability parameter and s is the entropy of the basic state, H is the depth of the fluid, and $\Delta_U = U(H) - U(0)$ is the basic state zonal wind difference between the top and the bottom of the model. γ measures the relative importance of the advection of planetary vorticity respect to vortex tube stretching in the vorticity budget. $\gamma = 0$ implies the β effect is negligible and the Eady model is recovered. As γ increases planetary vorticity advection becomes more important and long neutral Rossby waves can develop. Essentially, increasing γ is equivalent to shifting K_c toward

higher wavenumbers, so that the Rossby wave regimes extends, while the unstable regime is compressed toward shorter waves. Therefore, increasing the basic state parameters H and B or decreasing Δ_U works to stabilise weakly unstable baroclinic waves into Rossby waves, and vice versa.

1.5 Tropical–Extratropical interaction

The heat and momentum transport by atmospheric motions determine the observed time mean state of the atmosphere, but, as discussed in the previous sections, very different physical processes sustain these transports in the tropical and in the extratropical regions. Convection and Hadley cell overturning are dominating in the tropics, while baroclinic waves are more important in the extratropics. Eminently tropical and extratropical processes can nonetheless interact, and at least three different mechanisms of interaction can be taken in consideration:

1. Direct forcing of Extratropical waves by tropical convection (Hoskins and Karoly, 1981). As previously noted, tropical convection can feed vorticity in a stationary extratropical neutral Rossby wave which propagates from the injection point toward the extratropics. The trajectory of the wave is strongly dependent on the upper tropospheric zonal wind. In particular, jet streams can work as Rossby wave guides that channel the wave energy into a preferential zonal propagation (Ambrizzi and Hoskins, 1997)

2. Direct forcing of tropical convection by extratropical waves (Kiladis and Weickmann, 1992). Baroclinically active or Rossby waves propagating into the tropics can trigger tropical convection by lifting air ahead of the trough of the waves. The meridional propagation of the wave can be limited by non linear wave breaking that on average occurs at the latitude where the zonal wind speed of the mean state approximately equals the zonal phase speed of the wave (W Randel, 1991). As

typical extratropical baroclinic waves are eastward propagating they tend to break over the subtropics, so that the interaction results inhibited. Conversely, stationary Rossby waves can propagate closer to the equator so that convection is more easily excited.

3. Indirect forcing of baroclinic wave activity by tropical convection mediated by the Hadley cell. Because the meridional gradient of the vertically averaged temperature has to remain sufficiently *weak* across the tropics, positive persistent anomalies of tropical convective activity can force an increased meridional Hadley cell overturning, which warms the subtropics and increases the extratropical average baroclinicity. As a result, the energetics of extratropical baroclinic waves, especially those near the condition of marginal stability, can be substantially changed.

Chapter 2

The numerical model and data

This chapter provides a description of the numerical model and of the datasets that have been used in the thesis. In particular, section 2.1 gives a general overview of the architecture of the AGCM while section 2.2 describes the specific implementations used to perform the AMIP and the aquaplanet simulations. The datasets of observations that have been used for analysing the Earth's climate are described in section 2.3.

2.1 The Atmospheric General Circulation Model

2.1.1 General features

The experiments have been performed with the ECHAM5 AGCM (Roeckner et al., 2003). This is a moist primitive equation global spectral model of the atmosphere on hybrid levels (Washington and Parkinson, 2005). The model includes state of the art parameterisations of all major physical process, i.e. orographic gravity waves drag, shallow and deep convection, large scale precipitation, radiative heat transfer, vertical and horizontal diffusion processes and boundary layer physics.

The dynamical core of the model consists on the primitive equation of the atmosphere in the formulation derived from the weather forecasting model used at the European Centre for Medium–Range Weather Forecast

(ECMWF). Primitive equations are a set of differential equations that determine the motions of a stratified fluid in a rotating system of spherical geometry, under the approximation that the horizontal scale of motion is smaller than the vertical one, and that each column of air is in hydrostatic equilibrium. Both these conditions are well satisfied at the relatively coarse horizontal resolutions adopted for climate studies (Holton, 2004). Moist primitive equations are the mathematical transcription of the following fundamental physical conservation laws:

1. The zonal and meridional momentum balance equations
2. Vertical momentum balance equation, which, under the cited approximation, becomes the hydrostatic equation
3. Heat balance equation
4. Conservation of mass
5. Conservation of water species: vapour, liquid and ice phase

The equation of state of ideal gases closes the problem by creating a system of nine equations in nine variables: the vorticity (ξ) and the divergence (D) of the horizontal wind field, the temperature T, the logarithm of surface pressure p_s, the concentrations of vapour (q_v), liquid (q_l) and ice (q_i) water, the vertical velocity (ω) and the air density (ρ). The last two variables do not appear as time derived quantities of corresponding prognostic equations. Therefore the thermodynamical state of the atmosphere is defined by the following state vector (X):

$$X = (\xi, D, T, \log(p_s), q_v, q_l, q_i), \tag{2.1}$$

while ω and ρ are diagnostically computed at every timestep from the state vector itself.

The *physics of the model* includes all those processes participating to atmospheric dynamics which are not explicitly resolved by the primitive equations. They can be separated in two classes:

1. Physical processes that don't pertain fluid dynamics, i.e. radiative heat transfer.

2. Physical processes that pertain fluid dynamics but that can't be resolved by the primitive equations. For example, they can be filtered by the hydrostatic approximation or they can feature spatial or temporal scales which are smaller than those resolved at the model resolution, i.e. clouds, convection, boundary layer turbulence, surface fluxes.

The physics of the model determines the sources and sinks of heat, momentum and moisture which are the fundamental drivers of the atmospheric circulation. Such processes, which are essential for a realistic climate simulation, are therefore parameterised in function of the resolved state of the atmosphere via best estimate approximate formulas derived by semi–empirical theories and expert judgement.

The model can be thus considered composed of two parts: the dynamical core, which by integrating the primitive equations control the time evolution of the atmosphere due to resolved fluid dynamical processes, and a set of parameterised physical processes which provide a forcing on the resolved state of the atmosphere.

2.1.2 The Discretisation

The model equations are numerically time forward integrated by discretising the atmospheric in both the vertical direction and in the horizontal plane. In the former case the atmosphere is divided into layers corresponding to selected values of the vertical coordinate, while in the latter the fields are approximated by a truncated series of spherical harmonics. This allows to transform the partial differential equation composing the primitive equations, in a huge set of ordinary differential equations, which can be solved by numerical techniques. Temporal integration is performed by a semi implicit leap–frog time differencing scheme (Robert, 1982).

Horizontal representation

A generic square integrable function $\zeta(\lambda, \varphi, t)$ defined on a spherical domain can be expressed as a series of spherical harmonics $\mathrm{Y}_{\mathrm{l}}^{\mathrm{m}}$:

$$\zeta(\mu, \lambda, t) = \sum_{l=0}^{\infty} \sum_{|m|=0}^{l} \zeta_l^m(t) \mathrm{Y}_l^m(\mu, \lambda) \tag{2.2}$$

$$\mathrm{Y}_l^m(\mu, \lambda) = \mathrm{P}_l^m(\mu) e^{im\lambda}, \tag{2.3}$$

where $\mu = \sin\varphi$, P_l^m are the associated Legendre polynomials, and ζ_l^m are the complex spherical coefficients. Every spherical component is identified by the (l,m) couple of wavenumbers. m is the zonal wave number so that $2 \cdot m$ is the number of nodes along a parallel. l is a measure of the total (zonal plus meridional) wavenumber, and $(l - m + 1)/2$ gives the number of nodes in the meridional direction excluding the two fixed nodes at the poles (Washington and Parkinson, 2005).

In the model, all the variables in the atmospheric state vector X, apart for the water concentrations q_w, q_l, q_i, are represented in the horizontal plane as a truncated series of spherical harmonics. The couples of (l,m) spherical harmonics that are retained in the truncation are defined by the triangular scheme (Washington and Parkinson, 2005). Therefore, the truncated series results to be:

$$\zeta(\mu, \lambda, t) = \sum_{l=0}^{J} \sum_{|m|=0}^{l} \zeta_l^m(t) \mathrm{Y}_l^m(\mu, \lambda), \tag{2.4}$$

where the parameter J, which is used to indicate the model horizontal resolution, is the greatest total wavenumber represented in the model.

In spectral models, the linear differential operators, as the hyper laplacian and the zonal and meridional gradients, can be exactly computed in the space of the spherical harmonics. On the contrary the calculation of non linear terms in spectral space is not computationally efficient, and better performances are obtained by the *transform method* (Bourke, 1972). At every timestep the fields are transformed (Legendre plus Fourier) into a gaussian

Truncation	N. lon	N. lat	Δ_{max}	r_G
T31	96	48	420	1020
T42	128	64	310	750
T106	320	160	130	300

Table 2.1: Features of the model grid at the horizontal truncation indicated in the first column. The second and third columns indicate the number of grid points in the zonal and meridional directions, respectively. The forth column indicates the distance between the grid points in the largest model cell. The last one contains the radius of the smallest localised resolved feature. Distances are expressed in Km

grid[1], the products are locally computed at each grid point, and the resulting tendencies are finally transformed back to the spectral space. The tendencies of the state vector produced by the parameterised physics are as well computed on the grid space.

The spectral horizontal resolutions adopted in this work and the corresponding number of points in the grid space are reported in Table 2.1. Interpreting the spatial resolution corresponding to each spectral truncation requires attention. One approach is to simply consider the spatial resolution roughly equals to the maximum distance between neighbouring grid points. This quantity is reported as Δ_{max} in Table 2.1. As noted by Lander and Hoskins (1997), Δ_{max} underestimates by a factor of 2.6 the radius of the smallest localised resolvable feature in the spectral space, which is indicated as r_G in Table 2.1. Therefore, while Δ_{max} can be considered the spatial resolution of the physics, which is defined on the grid space, r_G is the resolution of the dynamics, which is solved in the spectral space. For example, despite the T31 truncation computes precipitation every 420 Km, no cyclones with a diameter smaller than 2000 Km can be resolved at that resolution.

[1] A grid is said to be Gaussian when the latitudes of its points are the zeros of an associated Legendre polynomial. These grids allows faster spectral–grid points transformations

	1000–850	850–100	100-top
L19	4	11	4
L31	5	21	5

Table 2.2: Number of vertical levels falling in the pressure ranges indicated in the first line (mb) for the L19 and the L31 configurations of the model. The surface pressure, which determines the specific pressure of hybrid levels, has been considered equal to 1000mb.

Vertical representation

To represent the vertical variations of a variable the atmosphere is divided into layers called *hybrid levels* (Roeckner et al., 2003). These layers are terrain following in the lower troposphere but get progressively flatter as the height increases.

Simulations have been performed with 19 and 31 vertical levels, which are respectively indicated as L19 and L31. In both the configurations the highest level is located at 10 hPa. The number of levels falling in the pressure ranges roughly corresponding to the boundary layer (1000mb–850mb), to the free troposphere (850mb–100mb) and to the stratosphere (pressure smaller than 100mb) are reported in Table 2.2. Increasing the vertical resolution leads to a doubling of the number of vertical levels in the 850–100mb pressure range, while very little changes are found in the boundary layer and in the stratosphere. Therefore the main advantage of adopting 31 vertical levels is a better representation of tropospheric dynamical processes. Boundary layer turbulence is similarly parameterised in the two configurations, and the dynamics of the stratosphere is only crudely represented with both 19 or 31 vertical levels.

The systematic error of the ECHAM5 AGCM with respect to changes in the horizontal and in the vertical resolution has been analysed in detail by Roeckner et al. (2006). Their results stress the importance of consistently increasing both the vertical and the horizontal resolution for minimising the

systematic error of the model. When the vertical resolution is set at L19, increasing the horizontal resolution above T42 does not lead to relevant improvements in the simulated mean state. On the contrary, the T63L31 model performs remarkably better than the T63L19, and a further slow, but constant, reduction in the systematic error is observed up to T159L31. Roeckner et al. (2006) suggested that the substantial benefit of refining vertical and horizontal resolutions at the same time could be related to the existence of preferential *aspect ratios*[2] for the representation of extratropical baroclinic processes. In particular, a benefit could be expected if the aspect ratio of the grid is close to the aspect ratio of the paths of the parcels of air in extratropical baroclinic waves (Lindzen and Fox-Rabinovitz, 1989). According to scaling arguments by Quasi–Geostrophic (QG) theory (Pedlosky, 1979), the slope of the paths is given by the following relationship:

$$(\tan\alpha)^{-1} = \frac{N}{f} \sim 120 - 200, \tag{2.5}$$

where α is the angle between the path and the horizontal plane, while N and f are the local values of the atmospheric static stability and of the planetary vorticity, respectively.

The experiments that will be analysed in this thesis feature the following spatial resolutions: T31L19, T42L31, T106L31. However, we should note, that at T106 even an higher vertical resolution would be needed to keep the aspect ratio of the grid close to the typical extratropical values of N/f (Roeckner et al., 2006). L19 might instead have been enough at T42. We will come back on these considerations in the conclusion of the thesis.

2.1.3 Boundary fluxes

Boundary fluxes result from the interaction of the atmosphere with its neighbouring systems, namely the ocean and land at the surface and the space at the Top Of the Atmosphere (TOA). But most of the incoming

[2]With this term we refer to ratios between vertical and horizontal space intervals. When referring to models the intervals are given by the grid spacing.

solar radiation is absorbed at the Earth surface, so that the atmosphere is essentially warmed from the surface heat fluxes. Therefore, the surface temperature is one of the leading parameters controlling the atmospheric motions.

The vertical surface flux of a generic quantity χ, namely momentum, water or heat, is due to subgrid scale turbulent processes, and it is parameterised in the model by the following bulk transfer relation (Roeckner et al., 2006):

$$(\overline{w'\chi'})_S = -C_S(X_S)|\vec{V}_L|(\chi_L - \chi_S), \tag{2.6}$$

where the subscripts S and L refer to the values at the surface and at the lowest model layer respectively, $\overline{w'\chi'}$ is the vertical turbulent transport of χ, $|\vec{V}|$ the intensity of the horizontal wind, and C_S is a transfer function obtained by Monin–Obukhov similarity theory (Louis, 1979). C_S is a function of the convective stability properties of the atmosphere at the lowest layer of the model and of the *rugosity* of the ground (Holton, 2004). The intensity of the flux is thus a function of the resolved state of the atmosphere, of the difference in the transported variable between the lowest model layer and the surface, and of the physical characteristics of the ground.

The surface heat flux, as determined by equation 2.6, works to relax the temperature at the lowest layer of the model toward the surface value. But in the Earth's climate, especially over regions of low thermal inertia as continents, the surface temperature is itself evolving and responding to the atmospheric state. Therefore, the AGCM incorporates a simple model of Earth's soil which, using an implicit scheme, synchronously determines the surface prognostic variables and the surface fluxes so that the surface energy balance is closed. The temporal evolution of the monthly SST is instead read from an external file. The daily linear interpolation of these monthly values is effectively used at the lower boundary condition and it constitutes a prescribed external forcing to the atmospheric system.

2.2 Model set up

The default parameterisations of ECHAM5 (sub–version 4.0), unless differently stated, are adopted in the experiments. In particular, convection is represented by the Nordeng (1994) mass–flux scheme. The cloud cover is determined by the statistical scheme introduced by Tompkins (2002) which includes prognostic equations for the distribution of moments. Advection of water components is computed by a flux–form semi–Lagrangian scheme (Lin and Rood, 1996).

2.2.1 Earth's climate simulations

Simulations of the Earth's climate have been realised performing AMIP style simulations. The salient feature of AMIP simulations is the use of monthly mean observed SST and Sea Ice Concentration (SIC), i.e. the percentage of area covered by sea ice, as model lower boundary conditions over the oceanic regions. The performed simulations start on 1st January 1978 and terminate on 31st December 2009, which covers the time period when globally accurate satellite derived observations of SST are available (Rayner et al., 2003). Data are gathered after 1 year of spin up so that 31 years long simulations are effectively analysed. Monthly mean climatological values of the ozone, and a constant CO2 concentration equal to 348 ppmv are used.

Coupled Atmosphere–Ocean General Circulation Models (AOGCMs) often feature bias in the simulated SST (Lin, 2007; Richter and Shang-Ping, 2008). These bias are instead, by definition, absent in AMIP simulations. Therefore AMIP studies are a powerful tool for analysing atmospheric processes that are crucially dependent on a good representation of SST. Moreover the systematic errors of the AGCM can be analysed by comparing the simulated and the observed atmospheric climate over a common time period. On the other hand, the atmospheric processes that are influenced by atmospheric–oceanic feedbacks are negatively affected by the stiff representation of SST, and may thus be not well represented in AMIP experiments (Slingo et al.,

1996; Waliser et al., 1999; Kemball-Cook et al., 2002).

To increase the accuracy in the estimation of climate statistics, an ensemble of three identical experiments, which are just differing in the starting date by one month, have been realised for each adopted resolution (i.e. T31L19, T42L31 and T106L31). Each experiment of the ensemble follows a different dynamical evolution, so that indipendent estimations of the statistical properties of the simulated climate can be computed.

2.2.2 The Aquaplanet model

The expression "aquaplanet model" refers to an AGCM whose lower boundary is given by a flat swamp ocean (motionless and of infinite heat capacity). An aquaplanet setup of the AGCM has been realised using the parameters and suggestions given in the AquaPlanet Experiment (APE) project. The setting features a permanent equinoctial incoming radiation, which is realised by modifying the orbital parameters. In particular, eccentricity and Earth obliquity are set to zero. The radiation pattern, which includes the diurnal cycle, and the prescribed zonally symmetric SST constitute the two, indipendent, forcing of the system. Sea ice is absent and SST values are above freezing over all the domain.

The aquaplanet model has been chosen as a simplified tool for investigating tropical–extratropical interaction processes that can potentially lead to systematic errors in AGCMs. Atmospheric waves that rely on the presence of orography, as the stationary forced Rossby waves and the baroclinic–orographic resonances, are absent in the aquaplanet, and its climate is expected to be zonally symmetric simply after considerations about the symmetry of the system. Moreover, the absence of the seasonal cycle, of an interactive ocean, of land areas and of sea ice implies that the aquaplanet model is free of all the slow components of the climate system. This allows a faster estimation of climate statistics, and eleven years long simulations are sufficient for a very accurate computation of the energetic and of the kinematic properties of extratropical baroclinic waves. Data are gathered every six hours

after one year of spin up, so that ten 10 years of simulation are examined. The 6 hourly data are used to compute daily averages which are effectively analysed.

In this simplified framework, once the functional dependance of SST on latitude is defined, the overall state of the climate system is determined by few climate parameters, as the SST value at the equator (T_e), and the equator to pole SST difference (Δ_T). By varying these parameters we have framed the following set of SST distributions which drive the experiments analysed in chapters 3 and 4:

$$\mathrm{SST}(\lambda,\varphi) = \begin{cases} T_e - \Delta_T \cdot \sin^2(\frac{3\varphi}{2}) & -\frac{\pi}{3} < \varphi < \frac{\pi}{3} \qquad 0 < \lambda \leq 2\pi \\ T_e - \Delta_T & \text{otherwise} \end{cases} , \quad (2.7)$$

where the control experiment of the APE project is recovered for $T_e = \Delta_T = 27°\mathrm{C}$. The SST distribution is zonally and hemispherically symmetric and the prescribed temperature is constant on latitudes poleward of 60°. Experiments with different values of T_e and Δ_T have been performed to study the impact of changing the intensity of the hydrological cycle and of the average baroclinicity of the system, respectively. In particular, T_e has been set equal to 25°C, 27°C and 29°C. For each value of T_e, Δ_T has been decreased in 2°C steps from T_e down to 5°C. The results from this set of 36 experiments will be presented in chapter 4. The global mean temperature, which is increased by decreasing Δ_T, will result a quantity of secondary relevance for the topic addressed in the thesis, so that the choice of fixing the equatorial SST is justified. Moreover, this choice makes basic features of the tropical atmosphere, as the lapse rate and the mid tropospheric temperature, less affected by changes in Δ_T. The resolution T31L19 has been adopted to perform all the aquaplanet simulations that will be discussed in the thesis. The only difference with the model setting adopted for the AMIP simulations, is that cloud cover is here computed by the diagnostic scheme of Lohmann and Roeckner (1996). We verified that aquaplanet results are not particularly sensitive to the specific choice of the cloud cover scheme.

2.3 Observed data

2.3.1 Reanalyses

Reanalyses are the best available homogeneous global and self–consistent dataset of the observed state of the atmosphere for climate studies and for the validation of climate models. Reanalyses are generated by assimilating observations of the state of the atmosphere and of the Earth's surface into an AGCM, so that its dynamical evolution is bounded to remain close to the actual evolution of the atmosphere. The self consistency is guaranteed by the use of a same data assimilation scheme over the whole analysed time period. Differences between Reanalyses can result because of differences in the set of assimilated observations, in the data assimilation technique or in the numerics and the physics of the AGCM.

The National Center for Environmental Prediction (NCEP), together with the Department Of Energy (DOE), has started to release in May 2001 the NCEP–DOE reanalysis (Kanamitsu et al., 2002) which aims at updating and correcting some known errors found in the previously released NCEP-NCAR reanalysis (Kalnay et al., 1996). In particular, the AGCM is a T62L28 global spectral model, and assimilation is performed using a 3Dvar scheme (Parrish and Derber, 1992). Global rawinsonde data, aircraft data, surface land synoptic data and satellite sounder data compose the observational dataset. The surface marine state is taken from the Comprehensive Ocean Atmosphere Data Set (COADS). The NCEP–DOE dataset covers the timespan 1979–2009 so that it is an excellent benchmark to be compared with the performed AMIP simulations. Daily averaged values defined on a 2.5° x 2.5° regular latitude longitude grid and on 8 pressure levels ranging from 1000hPa to 100hPa will be analysed in the thesis.

ERA–INTERIM reanalysis (Simmons et al., 2007), which is the latest reanalysis product realised by the ECMWF, differs in the atmospheric model, in the data assimilation system, and in the set of assimilated observations from the NCEP–DOE reanalysis. For instance, the AGCM adopted in ERA–

INTERIM has a much higher spatial resolution (T255L37), and the data assimilation is based on a 12 hour 4Dvar scheme. Unfortunately, ERA–INTERIM reanalysis, which starts on 1st January 1989, does not cover the first ten years simulated by the AMIP experiments. Therefore, to be consistent with the performed simulations, we will adopt NCEP–DOE reanalysis for evaluating the formation of quasi–stationary patterns and the energetics of extratropical baroclinic waves in the Earth's climate. Nonetheless, some climate statistics will be computed on both NCEP–DOE and ERA INTERIM reanalyses. This will be needed to make some conclusions more robust and to get a gross estimate of the uncertainty in the state of the climate system pictured by different Reanalyses.

2.3.2 Outgoing Longwave Radiation

Outgoing Longwave Radiation (OLR) gives a measure of the temperature, and therefore of the height, at which the photons reaching the space have been on average emitted. When clouds are present, the average emission level is close to the top of the cloud itself. Therefore, in tropical areas and on timescales longer than five days, low values of OLR are usually associated to precipitating cumulonimbus clouds extending up to the tropopause (Gruber and Krueger, 1984).

In the thesis we will use observations of OLR from the National Oceanic Atmospheric Administration (NOAA) polar–orbiting satellites as a proxy of tropical convective activity. The whole dataset covers the 1974–2009 period, with the exception of the satellite failure during 1978. Only data after 1979 will be however used in this work to be consistent with the timespan covered by AMIP simulations and reanalyses data. The dataset provides daily averaged values of OLR defined on a 2.5° x 2.5° regular latitude longitude grid. A linear interpolation in both the spatial and the temporal directions (Liebmann and Smith, 1996) is applied to fill the gaps due to satellite problems, archival problems or incomplete coverage, so that the dataset presents no missing values.

Chapter 3

Tropical–Extratropical resonance in an aquaplanet model

This chapter describes the kinematical properties of the quasi–stationary wave five activity that is observed in the aquaplanet model setup according to the control simulation of the APE project. The persistence of the pattern in both tropical and extratropical dynamical fields is analysed, and it reveals that the wave has to be considered as a form of coupled tropical–extratropical mode of variability (3.2). Further experiments are realised to determine whether tropical convection is passively excited or it is providing an active forcing sustaining the wave (3.3). The mechanism of interaction and the relations to the time mean state of the atmosphere are finally discussed (3.4).

3.1 Low frequency variability in symmetric models

Aquaplanet models, forced by Earth–like but zonally symmetric SST, have been observed to feature a strong and persistent quasi–stationary wave on the zonal wave number five (Watanabe, 2005), which has recently been found (Williamson 2009, personal communication) in most of the models participating in the AquaPlanet Intercomparison project (Neale and Hoskins,

2001). The matter is of interest because wave five quasi–stationary circumglobal patterns are also observed along the jet stream in summer SH (Salby, 1982; Kidson, 1999), and in the NH during both the boreal winter (Branstator, 2002; Chen, 2002) and the summer (Ding and Wang, 2005; Blackburn et al., 2008) seasons. While the strong wave guiding effect provided by the jet is known to be responsible for the zonal orientation of these teleconnection patterns, their dynamics is still not well understood, and the leaky normal mode theory proposed for the SH (Salby, 1982; Lin and Chan, 1989) has no clear counterpart in the NH. The attracting possibility to use aquaplanet models as interpretative tools of these low frequency modes calls for a deeper understanding of their properties.

A low frequency wavenumber five had been previously observed by Hendon and Hartmann (1985) (hereafter HH) in a two level dry primitive equation model with zonally symmetric boundary conditions, and forced by newtonian relaxation. The constant presence of a dominant low frequency wave five in a variety of models and for different boundary conditions suggests that there must be a fundamental atmospheric process leading to its formation. HH proposed a QG inverse turbulent energy cascade (Charney, 1971; Rhines, 1975; Basdevant et al., 1981; Larichev and Held, 1995), feeding energy at the latitude of the jet in a slowly propagating Rossby wave. The mechanism, which has been verified in observations (Lau, 1988; Kug et al., 2010), simplified models (Vautard and Legras, 1988; Cai and Mak, 1990; Robinson, 1991) and full GCMs (Branstator, 1992), relies on the organisation of high frequency transients by the low frequency wave in such a way that vorticity fluxes due to wave-wave interactions provide a positive feedback to the low frequency flow itself. In a QG model Cai and Mak (1990) showed that low frequency variability was entirely maintained by inverse energy cascade, while, when more realistic GCMs and observations are considered, its energetic contribution appears weaker than that provided by baroclinic and barotropic instability (Sheng and Hayashi, 1990a,b).

Schneider et al. (Schneider, 2004; Schneider and Walker, 2006) pointed

out that in dry primitive equations models the heat vertically redistributed by the baroclinic eddies can reequilibrate the system by lifting the tropopause so that the atmosphere remains in a state of weak eddy-eddy interaction where the inverse energy cascade becomes inhibited. The two level primitive equations model of HH is likely to behave as a QG one, because the "tropopause" coincides with the top of the model and cannot be adjusted by the dynamics. Moreover GCMs feature an e–folding damping time due to horizontal diffusion in the free troposphere orders of magnitude bigger than in HH model, and cumulus convection schemes that can provide vorticity sources interacting with the low frequency wave (Sardeshmukh and Hoskins, 1988). Therefore the dynamics and the energetics of the quasi–stationary waves in an aquaplanet could require a different interpretation from what proposed in HH.

If the persistent wave five could be satisfactorily interpreted as a neutral Rossby wave an equivalent barotropic vertical structure would be expected and an external energy source would be needed to maintain it against dissipation (Hoskins and Karoly, 1981; Held et al., 2002), while if it were an unstable baroclinic wave (Eady, 1949) a westward tilt with height of the geopotential and a phase speed equals to the zonal wind at a certain level of the basic flow would be rather expected. It is possible to frame simple models able to set in a common framework Rossby–like waves and unstable baroclinic waves. The Green (1960) model, which describes the linearized dynamics of a stratified rotating fluid with vertical shear, shows that marginally stable waves, associated to the transition between the two regimes, have a phase speed equal to the zonal surface wind speed, so that LFV may not be incompatible with a stationary baroclinic process (see sec. 1.4).

In this chapter the kinematic properties of the quasi–stationary waves in the aquaplanet will be discussed in relationship to their interaction with the tropical convection. This will allow to clarify whether the source of energy maintaining the wave has to be researched in extratropical or tropical dynamics.

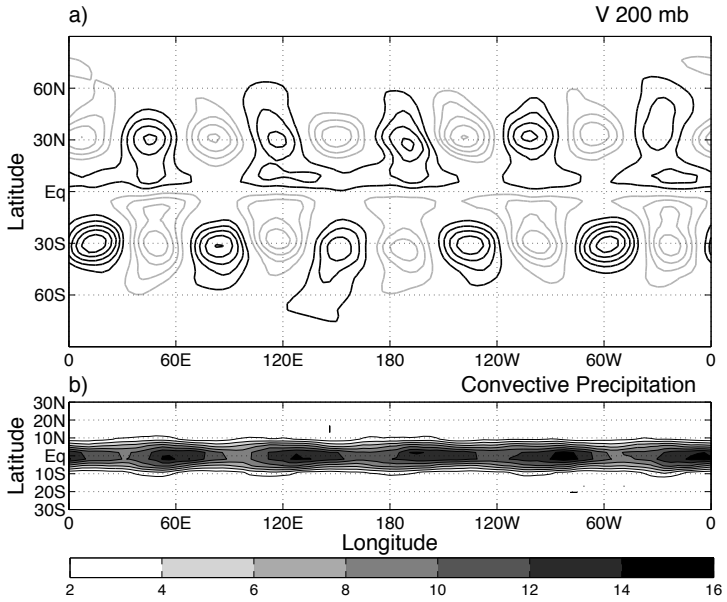

Figure 3.1: A six months average of the (a) meridional velocity at 200mb ($\mathrm{m\,s^{-1}}$) and of the (b) convective precipitation in the tropical region (mm/day) computed on an aquaplanet model setup according to the control experiment of the APE project ($T_e = \Delta_T = 27°\mathrm{C}$). In (a) the c.i.. is 2 $\mathrm{m\,s^{-1}}$ and dark (grey) lines indicate positive (negative) values. Zero contour is omitted.

3.2 The quasi–stationary wavenumber five

The simulation performed with the setting of the control experiment of the APE project (see sec. 2.2.2), shows a pattern dominated by the zonal component $k = 5$, which persists over timescales much longer than the atmospheric internal low frequency variability (Blackmon et al., 1984). To give a qualitative picture of the feature, Fig. 3.1a shows, as an example, a typical six months average of the meridional velocity at 200mb. A wave five of striking intensity peaks around 30°N/S and it extends over the latitude band 20°–50°. Under the same time period, an analogous pattern is found in the tropical convective precipitation, featuring a deviation from the zonal mean of the order of 30% (Fig. 3.1b). The two hemispheres appear to be coupled with

an upper tropospheric equatorial outflow (inflow) just west of the longitudes where tropical precipitation is enhanced (reduced). Selecting a different 6 months time period would have given us an average field with a dominating wave five pattern with similar amplitude but, in general, different phase.

Therefore, a quasi–stationary wave five is present in both the tropics and the extratropics despite very different dynamical constraints governing the atmosphere at low and high latitudes. We have thus introduced two bidimensional fields that allow to separately analyse the wave motions in the tropical and in the extratropical regions:

$$\hat{\Omega}(\lambda, t) = \{\omega(p_\omega, \lambda, \varphi, t)\}_0^{15} \tag{3.1}$$

$$\hat{V}(\lambda, t) = \{v(p_v, \lambda, \varphi, t)\}_{20}^{50}, \tag{3.2}$$

where ω is the vertical velocity ($\mathrm{Pa\,s^{-1}}$), v the meridional velocity ($\mathrm{m\,s^{-1}}$), $p_\omega = 500$mb and $p_v = 200$mb the pressure levels at which the variables are respectively evaluated, and $\{\}_{\varphi_1}^{\varphi_2}$ is an area weighted average between the latitudes φ_1 and φ_2. The latitudinal bands (both hemispheres are considered) and the levels have been chosen in order to contain the bulk of the low frequency power for all the set of simulations realised by varying Δ_T and T_e.

3.2.1 Wave persistence

A quantitative evaluation of the persistence of a wave can be obtained by the plot of the mean amplitude of the zonal Fourier components of the wave averaged over different time windows. The calculation is performed by partitioning the time domain in M non overlapping blocks of length τ days, and by averaging over all the blocks the amplitude of the mean wave component on each block. The averaging time (τ) has been chosen equal to the powers of 2, ranging from 1 to 256 days, and the results plotted in a bi-log scale. Therefore, the most persistent component will appear as having the slowest average amplitude decrease as τ is increased.

This method has been applied to the zonal wave numbers 3–7 in $\hat{V}$, and results are shown in Fig. 3.2. The variance of the unfiltered (daily mean,

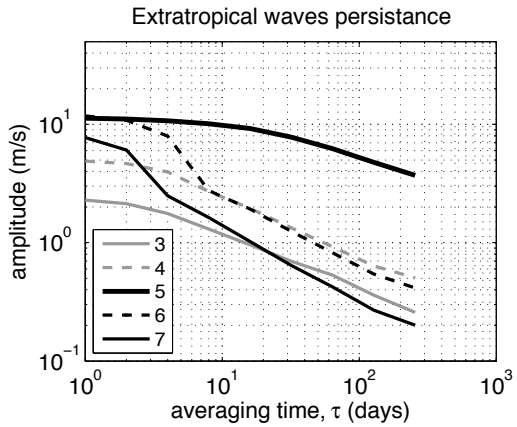

Figure 3.2: Mean amplitude of the zonal Fourier components in the extratropical 200mb meridional velocity ($\hat{V}$) averaged over as many non-overlapping time windows of τ days length. The amplitudes of zonal waves 3–7 are presented in a bi-log scale as a function of the averaging time τ itself. The wave $k = 5$ features the smallest amplitude decrease with time, and it is therefore the most persistent wave.

$\tau = 1$) $\hat{V}$ has an equal contribution from wavenumber five and six, but as the averaging time is increased the amplitude of the wave six drops down leaving the wave five notably stronger than all the other components on time scales longer than 10 days. A sharp drop in the wave amplitude over the synoptic timescales is visible for all the waves with $k > 5$, while for $k \leq 5$ a smoother decrease is observed, with the wave five featuring the smallest decrease for increasing τ. When $\tau = 32$ is considered, the amplitude of the wave five is $\sim 70\%$ of its $\tau = 1$ value, whereas for $k = 6$ the relative value realised for τ=32 is just 10% of the $\tau = 1$ value. Such a strong persistence can be only realised if the wave five features very low frequency and high temporal coherence. The amplitude of $\hat{\Omega}$ as a function of τ leads to similar conclusions, and has not been plotted.

3.2.2 Spectra

The Hayashi spectra (Hayashi, 1971) of $\hat{V}$ and of $\hat{\Omega}$ have been calculated and results are presented in Fig. 3.3. This technique, which is briefly described in appendix C.2, allows one to represent the variance of a longitude–time field as a function of the zonal wavenumber and the frequency of the eastward and westward propagating waves composing it. Hayashi spectra have been used to analyse and compare atmospheric variability in GCMs and reanalyses (Hayashi and Golder, 1977; Fraedrich and Böttger, 1978; Hayashi, 1982; Dell'Aquila et al., 2005; Lucarini et al., 2007; Dell'Aquila et al., 2007). Here, a two–sided representation has been adopted, in which the positive (negative) frequencies correspond to eastward (westward) propagating waves.

The Power Spectral Density (PSD) function of $\hat{V}$ shows that clear peaks in the zonal wavenumbers 3–7 are organised along a non dispersive dispersion relation, which has been put in evidence in Fig. 3.3a by an ellipse enclosing the bulk of its spectral power. At the reference latitude of 30° it corresponds to a group speed of about $+40\,\mathrm{m\,s^{-1}}$. Specifically we observe a spectral peak centered at $k = 5$ and frequency close to zero, which is consistent with the picture of a quasi–stationary wave provided before. Spectral peaks with $k < 5$ ($k > 5$) are westward (eastward) propagating. When inspecting the time evolution of the wave five phase (not shown), we discover that the wave alternates coherent periods of slow eastward and westward propagations which are the main causes of the slow loss of coherence of the wave presented in Fig. 3.2. The distribution of spectral power on higher frequencies as the zonal wavenumber increases is a typical feature of extratropical waves spectra (Dell'Aquila et al., 2005), and it is usually interpreted as the signature of baroclinic unstable waves.

As expected from the inspection of Fig. 3.3b, a quasi–stationary wave five appears as a dominant feature also when considering the spectrum of $\hat{\Omega}$. Relevant low frequency spectral density is as well observed at wavenumbers $k = 2$–3, while the dispersion relation on wave numbers 1–5, which is un-

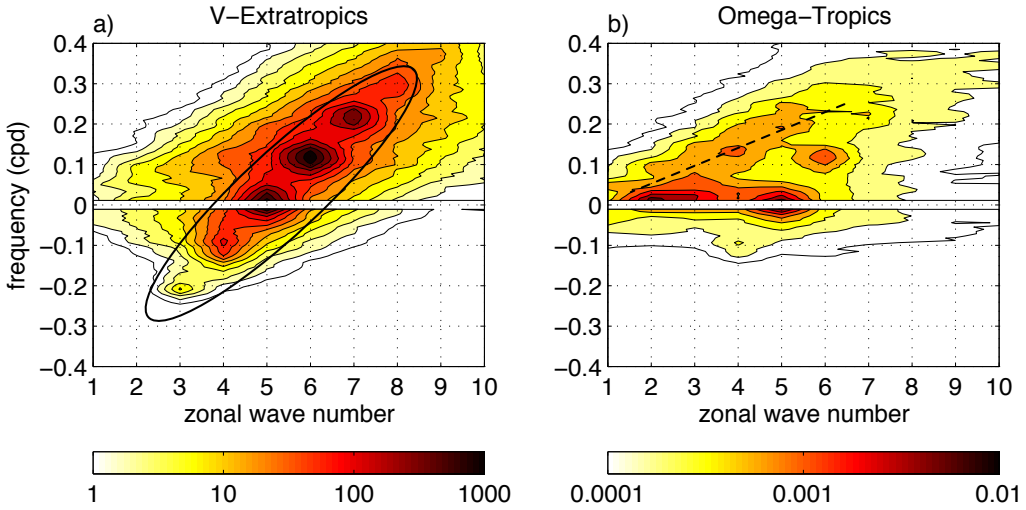

Figure 3.3: Hayashi power spectrum of (a) the 200mb meridional velocity averaged in the extratropics ($\hat{V}$) and (b) of the 500mb vertical velocity averaged in the tropics ($\hat{\Omega}$) for the control experiment. The spectrum is represented in a linear and two–sided representation, where frequencies are expressed in cycles per days (cpd), with positive (negative) values corresponding to eastward (westward) propagating waves respectively. The spectral density is presented in a logarithmic scale, and four contours are plotted every order of magnitude. Units are in $\mathrm{m^2\,s^{-2}\,day}$ (a) and $\mathrm{Pa^2\,s^{-2}\,day}$ (b). The ellipse in (a) indicates the main spectral region where extratropical wave activity is distributed, while the dotted line in (b) indicates the dispersion relation of tropical kelvin waves.

derlined by the dotted line in Fig. 3.3b, can be explained in terms of Kelvin waves propagating at the group speed of about $20\,\mathrm{m\,s^{-1}}$. This is in agreement with the speed observed in the actual climate system (Kiladis et al., 2009). As opposed to the extratropical case, spectral features for wavenumbers $k > 5$ are barely present, consistently with the fact that baroclinic active waves are absent in the tropics.

In order to test the presence of some coherence between the dominating patterns observed for the two fields described above, we estimate the

Probability Distribution Function (PDF) of the phase difference between the wave five components in $\hat{\Omega}$ and in $\hat{V}$. The PDF results to be bell-shaped and peaks around zero. This clarifies the presence of a phase lock between the wave five in $\hat{\Omega}$ and in $\hat{V}$. For $k \neq 5$ the PDF is instead roughly flat. Two possible distinct interpretations of the phase locking, which are differing in the location of the forcing process, can be hypothesised:

- The stationary extratropical wave is maintained by eminently local extratropical processes and induces a tropical convective pattern. Convection could eventually provide a positive feedback on the extratropical wave

- The source of energy is eminently tropical, with the stationary convective pattern forcing the extratropical stationary wave by feeding vorticity

The experiment described in the next section is designed to identify the right picture of the process.

3.3 The role of tropical convection

In order to clarify the location of the wave energy source, we perform an experiment where the non-zonal atmospheric forcing due to the tropical convection is suppressed and the zonal mean state of the atmosphere is not substantially altered. If the energy source were entirely in the tropics we would expect the quasi–stationary pattern to disappear, while if the tropical convection provides a feedback a change in the amplitude would be rather observed.

This experiment is realised by zonally redistributing at every time step the tendencies produced by the convection scheme in the tropical region:

$$\left.\frac{\partial \zeta}{\partial t}\right|_{conv}^{R} = \alpha(\varphi)\left[\frac{\partial \zeta}{\partial t}\right]_{conv} + (\alpha(\varphi) - 1)\left.\frac{\partial \zeta}{\partial t}\right|_{conv}, \tag{3.3}$$

where ζ represents a generic variable, namely q, u, v and T, *conv* refers to the contribution to the tendency given by the mass flux convective scheme, the square brackets stand for a zonal average and $\alpha(\varphi)$ is the degree of redistribution. A complete zonal redistribution ($\alpha = 1$) has been applied between 0° and 15° N/S, followed by a linear decrease to reach $\alpha = 0$ at 20° N/S, where the minimum in convective precipitation is located for all the experiments. The linear decrease has been introduced in order to reduce dynamical shocks due to discontinuities in the forcing. It must be remarked that we have redistributed only the tendencies due to the parameterised moist convection, so that the dynamical tendencies are still locally determined at every longitude, and zonally asymmetric tropical motions are still generated, but are heavily reduced. The terms SC and CTL will be used to address the experiment with and without the symmetrized tropical convection, respectively.

The difference in the zonal mean zonal wind $[\bar{u}]$ between the SC and CTL experiments (contours), and the $[\bar{u}]$ of the CTL experiment (shaded) are plotted in Fig. 3.4. We choose to compare the two experiments by using the $[\bar{u}]$ diagnostics because of its relevance as a parameter controlling the Rossby waves propagation and the link of its vertical shear to the baroclinicity of the system. Except for the upper equatorial region, the differences in $[\bar{u}]$ are smaller than 5%, and to a first order of approximation the mean state of the atmosphere remains reasonably unchanged by redistributing the convection.

We now use the same analysis performed in Fig. 3.2 but to compare the amplitude of the low frequency waves in $\hat{\Omega}$ and $\hat{V}$ between the two experiments. Fig. 3.5 shows that in the SC experiment the tropical wave five is highly damped, while a persistent extratropical wave five still remains. Remembering that vertical velocity is necessary for sustaining the tropical divergent flow which forces extratropical Rossby waves (Sardeshmukh and Hoskins, 1988), it is concluded that an extratropical energy source must be maintaining the low frequency mode, and the first hypothesis proposed in section 3.2 is found to be appropriate.

The lower values in the extratropical wave amplitude for $\tau \sim 15$ days

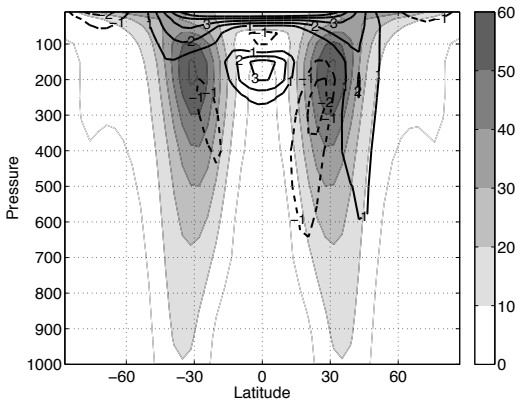

Figure 3.4: Zonal mean of the time mean zonal wind ($[\bar{u}_{CTL}]$) in the control (CTL) experiment (shaded) and difference in the same field (contours) between the zonally redistributed tropical convection (SC) experiment and the control ($[\bar{u}_{SC}]-[\bar{u}_{CTL}]$). Continuous (dashed) lines indicate positive (negative) values, and c.i. is 1 $\mathrm{m\,s^{-1}}$. The difference in the mean state between the two experiments in the extratropics is generally smaller than the 5%.

in the SC experiment (Fig. 3.5b) is consistent with the picture of a positive feedback generated by the interaction with the tropical convection, which is confirmed by an analysis of the SC experiments over the whole set of Δ_T values (not shown). Moreover the synchronisation in the wave five activity between NH and SH (see Fig. 3.1) is weaker in the SC experiments (not shown), so that the organisation of tropical convection on $k = 5$ is one of the mechanisms linking the two hemispheres.

3.4 The mechanism of interaction

Spectral analysis revealed that the quasi–stationary wave five belongs to a well defined eastward propagating wave packet. We therefore use lead–lag correlation maps (Kiladis and Weickmann, 1992; Lee and Held, 1993) to investigate the trajectory of the wave packet and to find out how the extratropical quasi–stationary wave effectively interacts with the tropical convection.

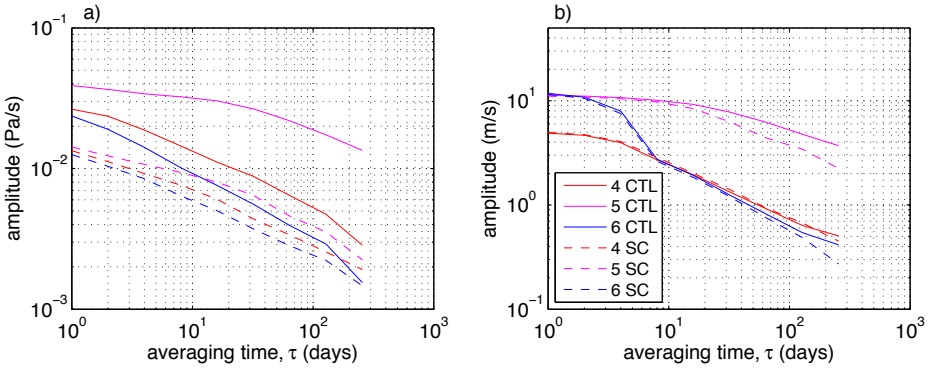

Figure 3.5: As in Fig. 3.2, but to compare the amplitude of the waves between the control (CTL, full line) and the zonally redistributed tropical convection (SC, dotted lines) experiments. The comparison is performed on (a) the tropical vertical velocity ($\hat{\Omega}$) and on (b) the extratropical meridional velocity ($\hat{V}$). The symmetrization of convection inhibits the wave five in the tropical convection while it just weakens its persistence in the extratropics.

Lead lag correlation maps have been constructed as follows. For each longitude–latitude grid point, the temporal correlation between the meridional velocity at 200mb at that grid point and the time series of the same field at a reference point is computed. Reference points of latitude equal to 32° and 46° degrees have been considered. Due to the zonal symmetry of the aquaplanet, correlation maps have been repeated for reference points with longitude positioned at every grid point of the model and the averaged map is computed. The temporal evolution of the wave packet is inferred by using time lags equal to -6, 0 and +6 days. Moreover, the field as been pre–processed by applying a 7 days low pass Lanczos filter (see appendix D), which retains the dominant components (k=5, k=6) participating in the wave packet. The results are presented in Fig. 3.6a–b, where the black dot indicates the position of the reference point.

The expected eastward propagating wave packet can be clearly seen in Fig. 3.6a–b, as the envelope of the wave proceeds eastward with increasing time lag. Nonetheless, the wave trajectory changes remarkably with the latit-

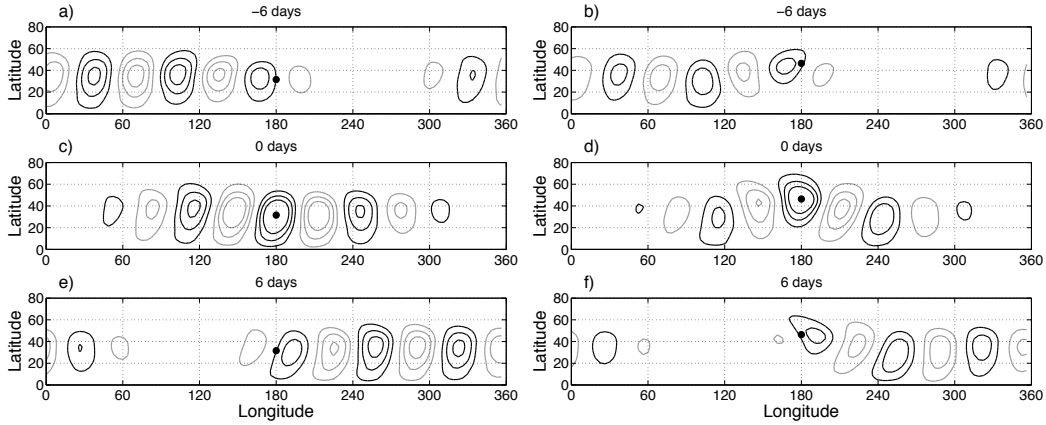

Figure 3.6: At each grid point, it is shown the time correlation between the meridional velocity at 200mb and the time series of the same field at the reference point which is indicated by the black dot added to the figure. In (a), (c) and (e) the latitude of the reference point is 32° while in (b), (d) and (f) is 46°. The titles indicate the lag of the correlation between the two time series. Contour interval is 0.2, the zero line has been omitted, and positive (negative) values are shown in black (grey)

ude of the reference point. The average structure of the wave passing through 32° (Fig. 3.6a), which is the latitude where the jet stream peaks, is predominantly zonally oriented, while the wave passing through 46° (Fig. 3.6b) propagates in an arching structure which escapes and returns to the subtropical latitudes around 70 degrees ahead and after the turning point. The formation of the arches has been found to be associated to a local weakening of the jet stream.

This suggests that the wave could kinematically behave as a Rossby wave zonally propagating along the upper tropospheric wave guide maintained by jet stream (see Fig. 3.4), and escaping from such a wave guide at the longitudes where the jet stream weakens (Hoskins and Ambrizzi, 1993). This is demonstrated in Fig. 3.7, where the stationary Rossby wave number at 200 mb (Hoskins and Karoly, 1981) is plotted against latitude. The zonal channel delimited by the latitudes at which $k = 5$ is stationary is centered at

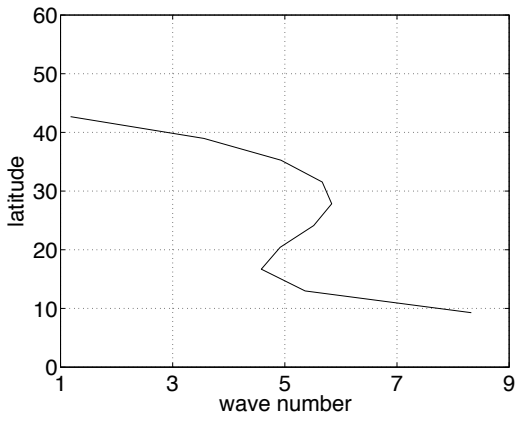

Figure 3.7: Meridional distribution of the stationary Rossby wavenumber (K_s) at 200mb as a function of latitude. K_s is computed on the time mean state of the control simulation of the aquaplanet. An upper tropospheric wave guide for a stationary Rossby wave five is found at about 30°

30°, in qualitative agreement with the latitude where the amplitude of the wave five peaks. This interpretation may be improved noting that the wave is more meridionally extended than the channel ($\sim 30°$ for the wave, against $\sim 15°$ for the channel), so that the wave five may rather see the climatological mean jet as a PV jump. Under this conditions, Rossby waves are trapped and their propagation non dispersive (Schwierz et al., 2004), in agreement with the observed main dispersion relation.

Lead–lag correlation maps will now be used to picture the average structure of the extratropical wave in relation to events of anomalous tropical convective activity. This is realised by computing the correlations between the meridional velocity at 200mb and the reference time series given by the meridionally averaged convective precipitation in the 0°–10° latitude band. The results, which are presented in Fig. 3.8, reveal that six days ahead of the convective episode, an extratropical wave of zonal wavenumber five, is arching toward the tropics. This suggests that tropical convection is forced by the extratropical wave, which is consistent with the results obtained from the SC experiment. At lag zero the wave arches back toward the extratropics,

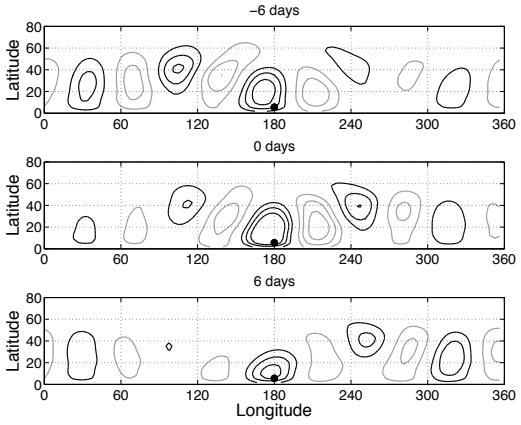

Figure 3.8: As in figure 3.6, but the reference time series is given by the meridional average of the convective precipitation in the 0°–10° latitude interval. This region can be individuated by the black dot added to the figures. Contour interval is 0.1

while six days after it is bending again toward the subtropics. This arching structure reminds of the trajectory of the average wave passing at 46° of latitude, but in this case the pattern has a more clear k=5 signature, and its phase remains essentially unchanged over the 12 days period.

These results suggest that the extratropical wave packet can enter in resonance with the tropical convection. The wave energy, thanks to the upper tropospheric wave guide, recirculates all around the globe in a zonally oriented or in arching trajectories. In this last configuration, the tropical approaching wave can trigger convective activity. This mechanism is consistent with the forcing of tropical convection by extratropical Rossby waves which is observed in the central pacific and over the maritime continent (Kiladis and Weickmann, 1992; Kiladis and Feldstein, 1994; Kiladis, 1998; Straub and Kiladis, 2003). As the wave packet includes a quasi–stationary k=5 component, the meridional and poleward motions tend to reform at approximately the same longitudes at every circumglobal transition of the wave packet. This component creates a coherent quasi stationary forcing on the tropical convective activity, which leads to its organisation on the same zonal

wavenumber.

The symmetrised convective experiment has shown that convection is not just passively excited but it actually exerts a positive feedback on the wave. Nonetheless the primary mechanism sustaining the quasi–stationary wave activity has to be extratropical. The next chapter will explicitly tackle this point by identifying the dominant energy source maintaining the wave against dissipation.

Chapter 4

A quasi–stationary baroclinic process

This chapter starts by analysing the energetic properties of the extratropical waves propagating in the aquaplanet model (4.1). This allows to formulate an interpretative theory on the nature of the quasi stationary wave five which explains not only its kinematics, as shown in the previous chapter using Rossby theory, but also its energetics (4.2). Sensitivity experiments will be later performed (4.3–4.4) to better asses the validity of the proposed theory. Finally, the implications of these results in the context of the Earth's climate and of the analysis of systematic errors of climate models are discussed in (sec. 4.5).

4.1 Energetics of the quasi–stationary wave

Previous analyses have proposed that barotropic mechanisms should maintain the quasi–stationary waves forming in models with zonally symmetric boundary conditions against dissipation (Hendon and Hartmann, 1985; Robinson, 1991; Watanabe, 2005). Instead, it is here suggested that baroclinic energy conversion is responsible for feeding energy into the wave. The very basic ingredient of baroclinicity, i.e. the presence of phase tilt with

height (baroclinic wedge) between the temperature and the meridional velocity of the wave, will be therefore tested. As well known, in barotropic conditions, such a tilt is absent.

4.1.1 Vertical wave structure

The zonal tilt with height of the average phase of the meridional velocity and of the temperature in the low frequency wave five has been computed for the averaged wave in the 40°–50° (hereafter referred as region a), 30°–40° (region b) and 20°–30° (region c) latitudinal bands. The calculation has been performed as follows. At each pressure level ($\hat{p}$), the relative phase difference with respect to the reference level $p_{ref} = 1000$mb is computed as:

$$\gamma(\hat{p}) = \arg < \zeta_5(t, \hat{p}), \zeta_5(t, p_{ref}) >, \tag{4.1}$$

where $\arg(z) = \arctan(\Im(z)/\Re(z))$ is the phase of the complex number z, $< \cdot, \cdot >$ stands for the correlation in time[1] and ζ_5 is the complex Fourier amplitude of the component $k = 5$ of a generic variable, namely v or T. The fields are preprocessed by applying a 10 days, 101 points long, Lanczos low pass filter (see appendix D) in order to get rid of the high frequency fluctuations. The relative phase γ_{rel} between the v and T wave is further obtained as:

$$\gamma_{rel} = \arg < v_5(t, p_{ref}), T_5(t, p_{ref}) > . \tag{4.2}$$

We've verified that the results, which are plotted in Fig. 4.1, are not sensitive to the choice of the reference level.

We first observe that the v and T waves have opposite tilt, as typical of baroclinic unstable waves. The baroclinic wedge is especially evident in region a, where baroclinicity is apparent throughout the troposphere, with vertical phase differences (about 1/12 of cycle, i.e 6 degrees) corresponding to about half of what observed in the dominant Earth's baroclinic waves (Lim

[1]The phase of the correlation between complex wave amplitudes — also know as complex correlation — is equivalent to the weighted time mean of the phase difference between the two waves, where the weight is the product of the respective amplitudes

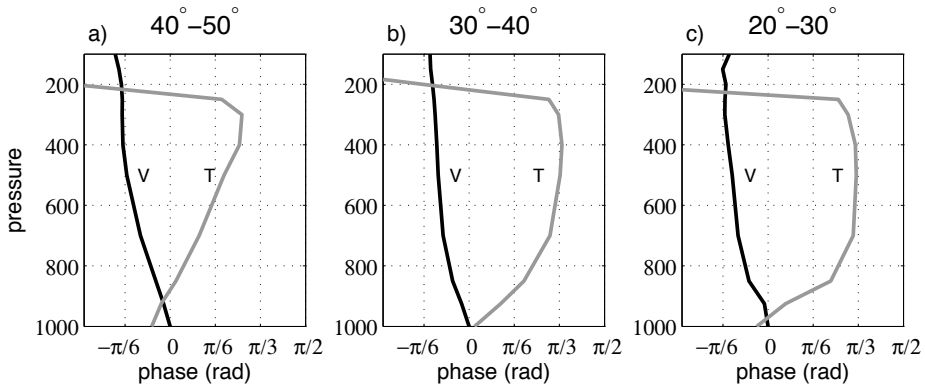

Figure 4.1: Mean zonal tilt with the height of the phase of the meridional velocity and of the temperature fields in the low frequency wave five. The vertical structure is separately calculated for the meridionally averaged wave on the latitude bands (a) 40°–50°, (b) 30°–40° and (c) 20°–30°.

and Wallace, 1991). As expected, in region c the baroclinicity is lower since we are close to the tropical region, and almost all of the phase tilt for the v and T fields is located in the lowest levels. Surprisingly, the baroclinicity is even weaker in region b which corresponds to the latitude band where the wave peaks: this will be addressed in a later section. A more quantitative analysis of the baroclinic conversion processes requires estimating the various terms relevant for the Lorenz energy cycle (Lorenz, 1967). A spectral approach has been therefore used to highlight the contributions to the heat transport and to the energy conversion terms projecting on the various frequencies and wavenumbers.

4.1.2 Heat transport

The eddy contributions to the meridional heat transport $[\overline{vT}]$ at 750 mb and to the vertical heat transport $[\overline{-\omega T}]$ at 500mb (where we have neglected c_p) have been calculated by the cospectral technique introduced by Hayashi (1971) which is reviewed in appendix C.2. A meridional average in the 20°–50° latitude band has been preliminarely applied to v, T, and ω. In Fig. 4.2

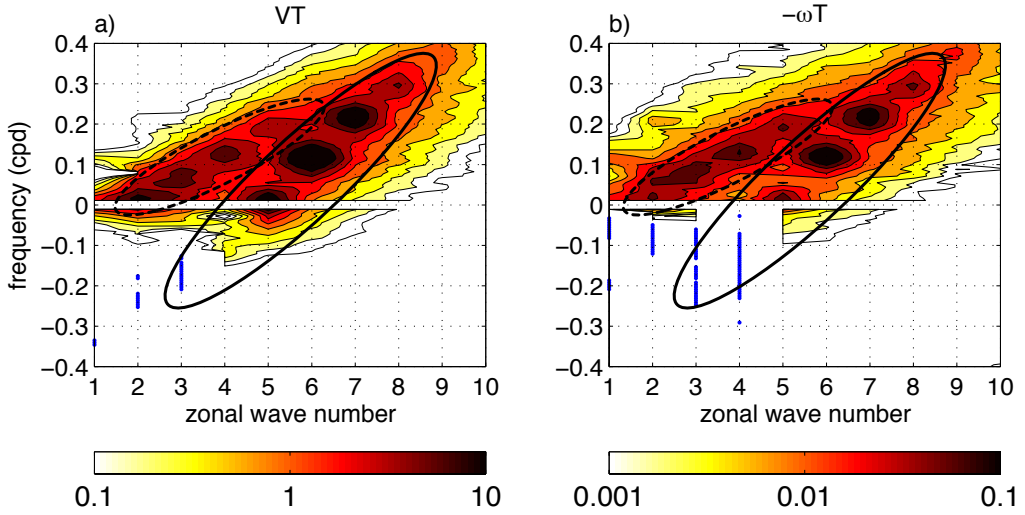

Figure 4.2: Spectral representation of (a) the meridional heat transport at 750mb and of (b) the vertical heat transport at 500mb as calculated by an Hayashi cospectral technique. Units are in $\mathrm{m\,s^{-1}\,K\,day}$ (a) and $\mathrm{Pa\,s^{-1}\,K\,day}$ (b). The multiplication by the specific heat c_p has been neglected and a meridional average in the 20°–50° latitude band as been previously applied to data. The plotting conventions are the same as those in Fig. 3.3, and the dotted areas correspond to regions featuring negative values significantly different from zero. The continuous and the dotted ellipses indicate the main and the secondary extratropical dispersion relations, respectively.

we show the positive values of the two cospectra $P_k^\nu(v,T)$ and $P_k^\nu(-\omega,T)$ using a logarithmic scale. The spectral components that feature negative values significantly different from zero at the 5% confidence level have been simply indicated by dots. Their values are however at least an order of magnitude smaller than the plotted positive ones.

$P_k^\nu(v,T)$ and $P_k^\nu(-\omega,T)$ show an overall similarity on a large part of the spectrum, whose positive valued part can be regarded as the region of active baroclinic waves. In fact, following the theory of the Lorenz's energy cycle, baroclinic unstable waves convert mean available potential energy into eddy potential energy, with a rate proportional to $P_k^\nu(v,T)$ times the meridional

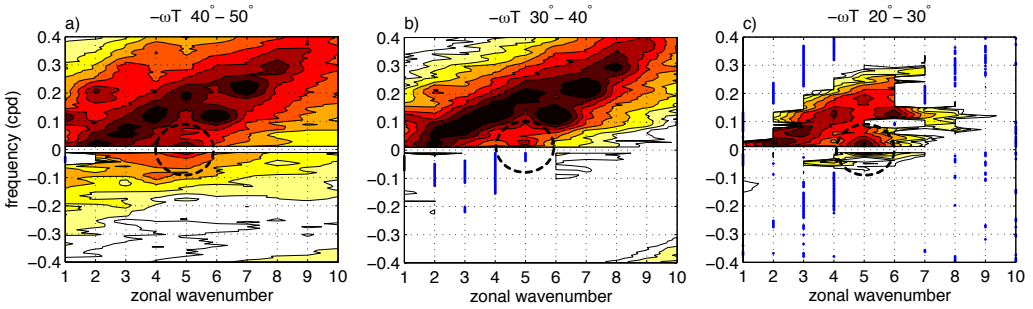

Figure 4.3: As in Fig. 4.2b but for the the vertical heat transport at 500mb due to the meridionally averaged waves in the (a) 40°–50° , (b) 30°–40° and (c) 20°–30° latitude bands. The dotted circle points to the baroclinic energy conversion by the low frequency wave five. Note the inhibition in the central latitude band.

temperature gradient, whereas eddy potential energy is converted into eddy kinetic energy, with a rate proportional to $P_k^{\nu}(-\omega, T)$ (Lorenz, 1967).

The analysis will now focus on the region delimited by the continuous ellipse drawn in Fig. 4.2a–b, which corresponds to the area where the spectral power in $\hat{V}$ is preferentially distributed (see Fig. 3.3a). All the spectral peaks of the selected region with $k > 5$ feature positive values in both $P_k^{\nu}(v, T)$ and $P_k^{\nu}(-\omega, T)$. This proves rigorously their baroclinic nature. Instead, the part of the region with $k < 5$ features weak or negative energy conversion, so that the spectral peaks there individuated in Fig. 3.3a are energetically equivalent to neutral Rossby waves. The low frequency wave five, which is found close the neutral boundary separating unstable and neutral waves, is the longest wave of the region which converts energy via baroclinic processes.

Outside of the main dispersion relation delimited by the continuous ellipse, a spectral region characterised by intense meridional and vertical heat transport, which is delimited by the dotted ellipse drawn in Fig. 4.2a–b, is observed on k=2–5 and frequencies 0.05–0.2 days^{-1}. This *secondary* dispersion relation, which does not dominate the PSD function of $\hat{V}$ shown in Fig. 3.3a, corresponds to baroclinic active, shallow and meridionally narrow

waves, as will be clarified by the arguments given in the subsection called *interpretation*.

To investigate the dependance on the latitude of the baroclinic energy conversion performed by the low frequency wave five, $P_k^\nu(-\omega, T)$ has been separately computed on the three previously defined latitudinal bands. The three resulting spectra are shown in Fig. 4.3a–c, and dotted circles have been drawn on the figures to indicate the spectral peak corresponding to the low frequency wave five. While in region *a* its energy conversion is comparable to the one performed by the other spectral peaks, and the same applies for region *c*, even if the baroclinic processes are overall much weaker, a reduced conversion is observed in region *b*. In particular, the energy conversion is completely suppressed on the negative frequencies, which suggests that baroclinic energy conversion is there realised only during periods of eastward propagation. This latitudinal structure is in agreement with the tilts in the v wave observed in Fig. 4.1. A similar analysis for $P_k^\nu(v, T)$ (not shown) reveals that the low frequency wave five transports heat meridionally in all the latitude bands. Therefore, the wave five is an active baroclinic wave, but its energy conversion is concentrated on some latitudes and it is sensitive to the zonal phase speed of the wave.

Whether baroclinic conversion is really the leading process maintaining the wave will be clarified by the energy balance presented in the next subsection.

4.1.3 Spectral energy balance

Barotropic instability and forcing by transient eddy fluxes are the atmospheric processes, other than the already mentioned direct baroclinic energy conversion, that could feed kinetic energy in the quasi–stationary wave five. The energetic contributions due to these processes have been quantified by the cross–spectral method proposed by Hayashi (1980), which essentially provides a spectral picture of the Lorenz energy cycle. For each spectral component, this method estimates the linear energy transfer between the eddy

kinetic and the eddy potential energy reservoirs, which results from barotropic and baroclinic processes, and the redistribution of eddy kinetic energy among spectral components due to non linear wave interactions, which includes the low–frequency forcing by transient eddy fluxes.

Using the Hayashi (1980) notation, the kinetic energy prognostic equation for the spectral component (k, ν), after integration over the whole atmosphere, can be written as:

$$\frac{\partial K_k^\nu}{\partial t} = \underbrace{< K \cdot K >_k^\nu}_{\text{wave–wave}} + \underbrace{< K_0 \cdot K_k^\nu >}_{\text{wave–mean}} + \underbrace{(-P_k^\nu(\alpha, \omega))}_{\text{baroclinic}} + D_k^\nu, \qquad (4.3)$$

where K_k^ν is the total kinetic energy on the spectral component (k, ν). $< K \cdot K >_k^\nu$ stands for the redistribution of energy into spectral component (k, ν) as a result of non linear interactions between different waves. In particular, the energy transfer occurs among triads of waves which are related in frequencies (and in wavenumbers) as ν, μ, $\nu \pm \mu$ (k, l, $k \pm l$). $< K_0 \cdot K_k^\nu >$ stands for the transfer of energy between the wave of spectral component (k, ν) and the kinetic energy of the time mean flow by barotropic processes. $< K \cdot K >_k^\nu$ and $< K_0 \cdot K_k^\nu >$ have been respectively computed by the formulae (3.12a–b) and (3.14a) of Hayashi (1980), and consist in the sum of terms involving cospectra between momentum and the convergence of momentum (see appendix C.3 for details). α is the specific volume and, as previously introduced, $P_k^\nu(\cdot, \cdot)$ indicates a 2D space–time cospectrum. Therefore, the term $-P_k^\nu(\alpha, \omega)$ gives the spectral estimation of the direct baroclinic energy conversion performed by the spectral component (k, ν). The last term refers to the kinetic energy lost on (k, ν) by dissipative processes. The only difference with the method described in Hayashi (1980) is that 1D space or time cospectra have been substituted by 2D space–time cospectra computed as in Eq. C.23. The derivation of Eq. 4.3 and the explicit expressions of its terms can be found in appendix C.3.

We have directly computed the first three terms on the rhs of Eq. 4.3. Global mean values are obtained by a vertical integration over eight pressure levels, ranging from 1000 mb to 100 mb, and a meridional area weighted

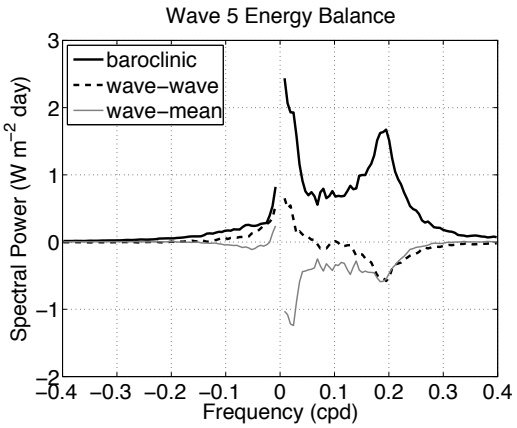

Figure 4.4: Spectral distribution of kinetic energy sources on k=5 as a function of frequency by fundamental atmospheric processes. Contributions by direct baroclinic energy conversion (black full line), non linear wave–wave interactions (black dashed line) and barotropic wave–mean flow processes (grey full line) are plotted in the figure. See the text for a description of the methodology. Units are in $\mathrm{W\,m^{-2}\,day}$.

average over all the latitudes of the model. Because we adopt a space–time decomposition, the lhs of Eq. 4.3 is zero, and dissipation can be estimated as the residual of the energy balance. The resulting spectral contributions to the energetics of the waves with $k = 5$ are plotted in Fig. 4.4 as a function of frequency. Fig. 4.4 clearly reveals that baroclinic conversion is the dominant process feeding kinetic energy in the [-0.1,0.1] (cpd) frequency range, where the power of the low frequency wave five is distributed. As typical of inverse energy cascade, high frequency transients, through the wave–wave interaction term, force positive kinetic energy in the low frequency band, but it represents just a minor contribution respect to the predominant baroclinic energetics of the wave five. Barotropic wave–mean flow interactions are instead on average draining kinetic energy out of the wave five and are reinforcing the time mean jet. Representative values for the three processes, which have been obtained by integrating the spectra over the [-0.1,0.1] frequency band, are reported in Table 4.1.

Table 4.1: Kinetic energy sources (+) and sinks (-) on the low frequency $k = 5$ wave due to fundamental atmospheric processes. Dissipation has been estimated as the residual closing the energy balance. The energetic contributions have been computed by integrating the unsmoothed energy transfer spectra over the [-0.1,0.1] (cpd) frequency band.

Process	Energetic contributions ($\mathrm{W\,m^{-2}}$)
Baroclinic	0.16
Wave–Wave	0.04
Wave–Mean	-0.06
Dissipation*	-0.14

Another peak in baroclinic energy conversion is present at $\nu \sim 0.2$ cpd. This is due to a fast propagating wave five that belongs to the secondary dispersion relation already mentioned when discussing Fig. 4.2.

4.2 Interpretation

These results lead us to introduce a new paradigm that describes the extratropical quasi–stationary wave five as a marginally stable baroclinic wave, and to look for theoretical models to justify its low phase speed and the latitudinal dependance of the efficiency of the energy conversion.

As previously discussed in the introduction, Green (1960) analysed the linear stability properties of an infinitely meridional extended wave ($l = 0$) when the beta effect is added to the Eady's model. Due to the long wave stabilization provided by the beta effect, his model contains both the neutral Rossby waves for $k < K_c$, and the baroclinically unstable waves for $k > K_c$, where K_c is the critical total wavenumber separating the two regimes. A marginally stable wave of phase speed equal to the surface zonal wind is found for $k = K_c$ (see Fig. 1.2), so that quasi–stationarity and marginal stability are two properties that coexist in the same wave. Components

with $k < K_c$ ($k > K_c$) are respectively westward (eastward) propagating. These features are in agreement with the previously described kinematic and energetic properties of the waves in the main dispersion relation around the marginal condition $k = 5$.

The fixed ($l = 0$) meridional wavenumber of the Green's model does not limit its interpretative value, because the waves in the main dispersion relation feature a meridional scale (L_b) close to the width of the jet stream, and thus nearly independent of k. The width of the baroclinic zone is indeed a favourite meridional scale for the most unstable wave (Hoskins and Revell, 1981), provided that the zonal wavenumber is sufficiently high to satisfy the necessary condition for baroclinic instability

$$k^2 + {l_b}^2 > {K_c}^2, \tag{4.4}$$

where l_b is a meridional wavenumber associated to L_b.

The presence of the secondary streak of peaks in Fig. 4.2 (see the dotted ellipse) can also be explained in terms of linearized baroclinic models. As k is decreased under five, relation 4.4 is no longer satisfied, and the meridional scale of the most unstable baroclinic wave has to become smaller than L_b to allow further baroclinic conversion. As a result, the secondary dispersion relation can be interpreted in terms of active baroclinic waves that are zonally longer and meridionally narrower respect to the active waves in the main dispersion relation (Hoskins and Revell, 1981).

In Fig. 4.3 we have seen that the energy conversion by the low frequency wave five has a peculiar latitudinal structure with relevant inhibition in the 30°–40° latitudinal band. An explanation is provided considering the bounds on the zonal phase speed (c_r) of unstable baroclinic waves calculated by Pedlosky (1979) in QG β channel conditions:

$$U_{min} - \frac{\beta}{2(\frac{\pi^2}{4L^2} + k^2)} \leq c_r \leq U_{max}, \tag{4.5}$$

where U_{min} and U_{max} are respectively the minimum and maximum of the zonal wind in the meridional plane, and L the width of the channel. Due to

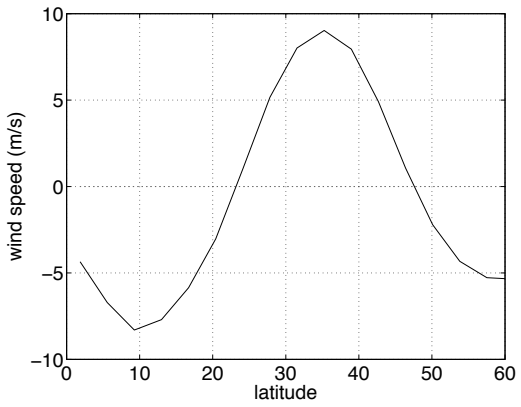

Figure 4.5: Meridional cross section of $[\bar{u}]$ at the lowest model level. The maximum in the surface zonal wind corresponds with the latitude band where the wave five has a more barotropic vertical structure and a weaker baroclinic energy conversion.

the β effect, relation 4.5 states that in presence of a westerly vertical shear unstable waves can propagate even slower than the minimum zonal surface wind. If a channel centered at 35° of latitude and 30° wide is taken as representative of the extratropical baroclinic zone of the aquaplanet, the correction[2] due to the β effect for $k = 5$ is of the order of 6 $\mathrm{m\,s^{-1}}$. Subtracting this value from the zonal mean zonal wind at the lowest model level, which is shown in Fig. 4.5, reveals that a quasi–stationary wave five can be unstable thanks to the presence of the weak westerly winds on the northern and southern flank of the surface jet stream, which is the latitude range where baroclinic conversion indeed occurs. On the contrary, in the 30°–40° latitude band the lower bound on the phase speed implies that waves with frequency $\lesssim +0.025$ should be stable, which is consistent with the weak conversion observed in Fig. 4.3b.

[2]Variations of ten degrees in the channel parameters lead to changes in the correction due to the β effect < 1 $\mathrm{m\,s^{-1}}$

4.3 Sensitivity to the baroclinicity of the system

Changing the equator to pole SST difference (Δ_T) amounts to altering the mean baroclinicity of the system. Analysing how the properties of the low frequency variability of the system depend on the temperature gradient allows us to test the robustness of our interpretation based on the Green's model.

In Fig. 4.6 we plot the mean amplitude of $\hat{V}$ for the zonal waves five, six and seven at the averaging time of 1 day (left) and 32 days (right) as a function of Δ_T. The two timescales have been chosen to measure the total and the low frequency mean wave amplitude respectively. As Δ_T is decreased the total wave amplitude decreases, in agreement with the reduced baroclinicity of the system (Stone, 1978), while the dominant low frequency mode drifts toward higher wave numbers. Wave five, six and seven reach their optimal stationary condition for $\Delta_T = 27$, $\Delta_T = 15$ and $\Delta_T = 11$ degrees respectively. This shift is in agreement with the displacement of the Green's model marginally stable baroclinic wave toward higher wavenumbers as the vertical shear of the basic state is decreased (see Eq. 1.4).

The stabilized waves six and seven feature a structure close resembling the one already described for the wave five. As an example, Fig. 4.7 shows a six months average of the experiment $\Delta_T = 15$ (compare it with the case $\Delta_T = 27$ shown in Fig. 3.1). An equatorward displacement of about 5° of the peak in the extratropical V wave, linked to the displacement of the jet stream itself, and a different tropical convective pattern of precipitation, are the only two remarkable differences of an otherwise similar pattern projecting on the zonal wavenumber six instead of five. SC experiments verified that the tropical convection is again responding and not forcing the extratropical wave.

The cospectra $P_k^\nu(v,T)$ and $P_k^\nu(-\omega,T)$ are shown in Fig. 4.8 for the selected simulations $\Delta_T = 21$, $\Delta_T = 17$ and $\Delta_T = 11$. The waves considered in

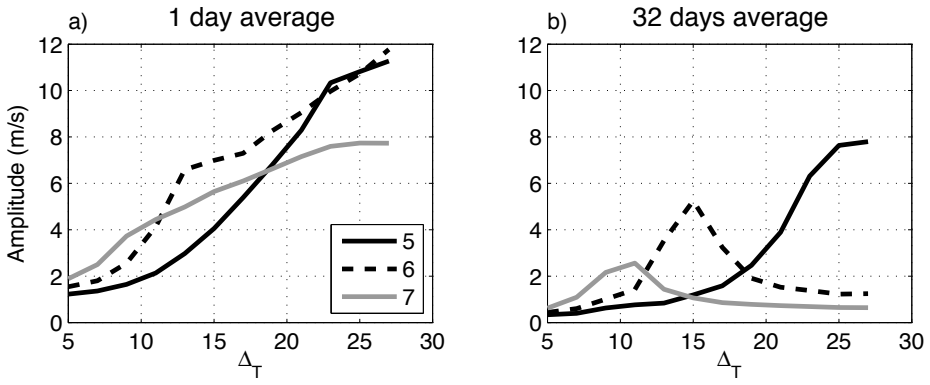

Figure 4.6: Mean amplitude of the zonal waves $k = 5$, $k = 6$ and $k = 7$ in $\hat{V}$ as a function of the equator to pole SST difference (Δ_T). $\hat{V}$ has been filtered, as described in Fig. 3.2, by averaging over time windows of length (a) 1 day and (b) 32 days, so that a measure of the total and of the low frequency wave amplitude is respectively selected.

the following discussion are those identified by the spectral power contained in the main dispersion relation of each experiment, which have been for clarity indicated in Fig. 4.8 by ellipses. For $\Delta_T = 21$ the wave five is still both the dominant low frequency wave and an active baroclinic wave vertically and meridionally transporting heat, but as Δ_T decreases its energy conversion is reduced and gets completely suppressed for $\Delta_T = 17$. The wave five has become a neutral westward propagating Rossby wave, which is only meridionally transporting heat and it is mainly forced by inverse energy cascade. But at this stage the wave six, which is both meridionally and vertically transporting heat, is the dominant low frequency wave, and the new marginally stable baroclinic component instead of wave five. By further decreasing Δ_T also the wave six becomes neutral, and the wave seven takes its place as the marginally stable quasi–stationary baroclinic component (Fig. 4.8e-f).

In all the experiments, a weak but significant counter baroclinic energy conversion is observed on the westward propagating components of the main dispersion relation (see Fig. 4.8b,d,f and in Fig. 4.2b). This inversion of the Lorenz energy cycle may not be surprising, because those components, which

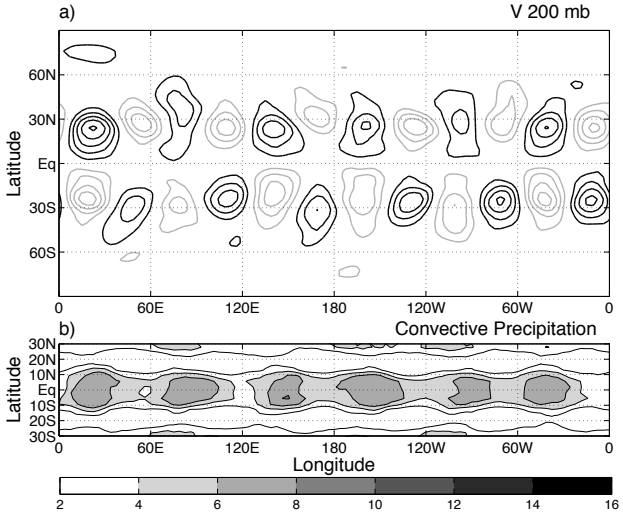

Figure 4.7: Same fields shown in Fig. 3.1 for a 6 months average taken form the aquaplanet simulation with SST parameters $T_e = 27, \Delta_T = 15$. For such a lowered baroclinicity of the system, the wave number six is quasi–stationary in place of the previously found wave five.

are baroclinically neutral, are principally forced by inverse energy cascade of kinetic energy, so that they have a source of kinetic energy but miss a source of potential energy. Therefore, a counter baroclinic energy conversion is necessary to produce the eddy available potential energy required to maintain thermal wind balance.

4.4 Sensitivity to the Equatorial Temperature

Increased tropical SST, via changes in the tropical moist adiabatic lapse rate, can lead to increased vertically averaged temperature in the Hadley cell region, so that the extratropical baroclinicity of the system is implicitly enhanced. Tropical SST could therefore impact the properties of the marginally stable component of the system. To determine whether the relationship between the marginally stable wave and the equatorial SST fits the proposed interpretative theory, two other sets of experiments, featuring $T_e = 25°$ and

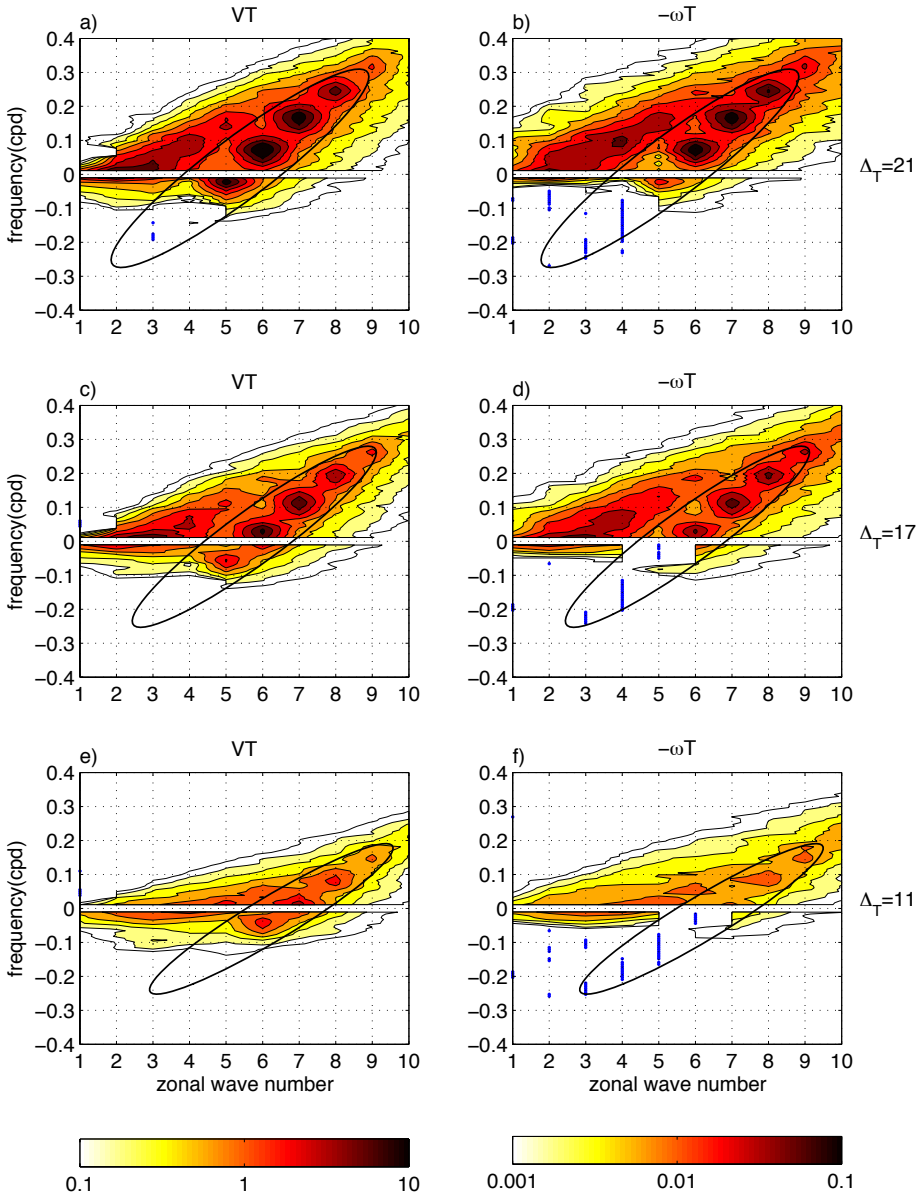

Figure 4.8: As in Fig. 4.2 but for simulations differing in the equator to pole SST difference: (a) $\Delta_T = 21°C$, (b) $\Delta_T = 17°C$ and (c) $\Delta_T = 11°C$. The equatorial SST is kept fixed at 27°C. As Δ_T decreases the wave five becomes stable, and the waves six (b) and seven (c) become the new marginally stable quasi–stationary baroclinic wave.

$T_e = 29°$ have been analysed. In each set of experiments, Δ_T ranges from 2° to T_e so that extratropical SST is above freezing for each simulation. Spectral analysis (not shown) verified that marginally stable and quasi stationary waves are also still present in this extended set of experiments.

The problem will be tackled by the same diagnostic adopted in Fig. 4.6b. In particular, Fig. 4.9a (b) shows the amplitude of the zonal wave k=5 (k=6) as a function of Δ_T and for different values of T_e. For both the k=5 and the k=6 component, increasing T_e moves the peak in the wave amplitude toward lower values of Δ_T. This implies that increasing Δ_T or T_e has similar effect on the properties of the marginally stable wave, and confirms that tropical SST, while keeping Δ_T fixed, can act as a forcing on the baroclinicity of the system. Instead, the global mean surface temperature, which increases with T_e but decreases with Δ_T, does not seem an adequate parameter for describing this problem.

To verify that the given interpretation is correct, in Fig. 4.9c (d) we have plotted the same quantity as in Fig. 4.9a (b), but as a function of the meridional maximum in the climatological zonal mean zonal wind at 200mb (U_{max}). This quantity is also a measure of the baroclinicity of the equilibrated state of the atmosphere. While, for different values in T_e, the peaks of the wave amplitude occur at different values of Δ_T, we note that they tend to be associated to reasonably similar values of U_{max}. This proofs that the properties of the marginally stable wave of the system are, to a first order of approximation, determined by the baroclinicity of the time averaged state of the atmosphere, which can be modified by manipulating both the surface extratropical meridional SST gradient or the tropical SST.

4.5 Discussion

The analysis of the energetic and of the kinematic properties of the extratropical waves in the aquaplanet model has revealed an unexpected new mechanism leading to the formation of quasi-stationary waves. Two pre-

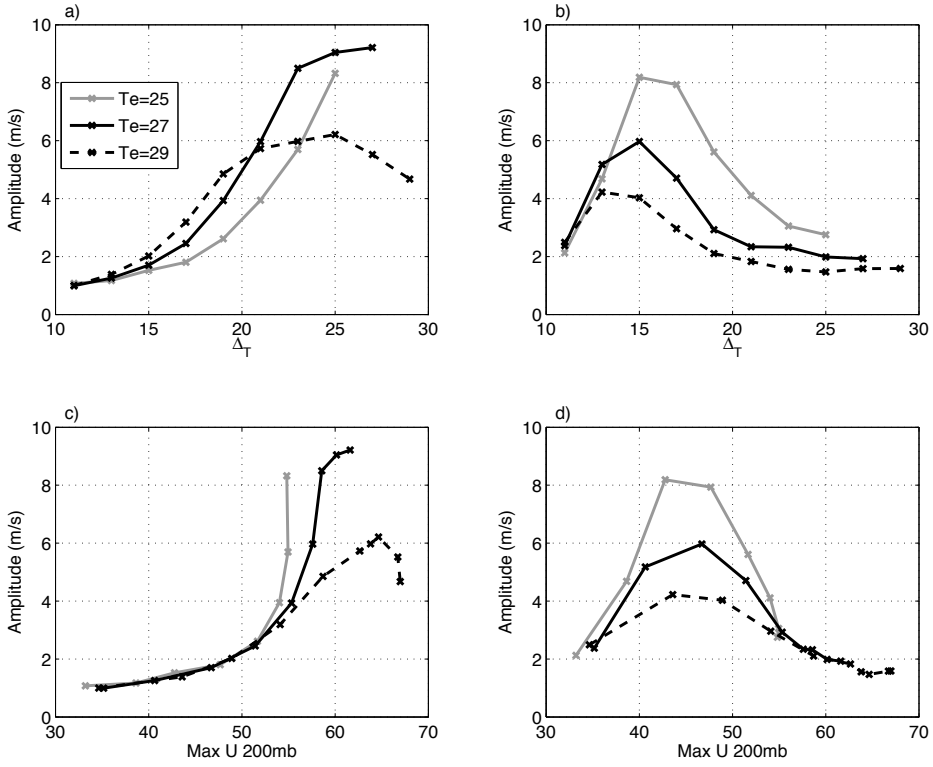

Figure 4.9: Mean amplitude of the zonal wave k=5 (a,c) and k=6 (b,d) in $\hat{V}$ as a function of the equator to pole SST difference (a,b) and of the maximum zonal wind at 200mb (c,d) $\hat{V}$ has been filtered as in Fig. 4.6b, and the three plotted lines correspond to different values of the equatorial temperature.

requisites have been identified as contributing to its establishment: a circumglobal wave guide, which allows for the recirculation of energy in the form of a baroclinic wave packet, and a marginally stable component which provides energy to the pattern via direct baroclinic energy conversion. Under these conditions, extratropical dynamics can itself maintain strong and persistent quasi–stationary wave activity even in the absence of external orographic or convective forcing.

These patterns, consistently with the zonal symmetry of the model, do not have a fixed longitudinal phase. After their establishment, they tend to remain approximately stationary for an average time scale of a few months,

until they disappear and later develop again with, in general, a different longitudinal phase. This is why the terminology *quasi–stationary* has been found appropriate. Nonetheless a breaking of the zonal symmetry of the system, which could be for instance due to a local longitudinal enhancement of the tropical convection, could determine a preferential phase for the formation of the quasi–stationary pattern. Under these settings, the mechanism could therefore lead to the development of a proper stationary wave of the system, which persists even when long time averages are considered. On the contrary, the breaking of the symmetry could preclude that the necessary conditions for the wave onset, as the circumglobal wave guide, are satisfied.

These considerations pose some interesting questions. Is the mechanism of any relevance for the formation of stationary or quasi–stationary patterns in the Earth's climate? Previous investigators (Watanabe, 2005) speculated that the circumglobal pattern identified in the NH by Branstator (2002), and the ubiquitous wave five observed by Salby (1982) in the SH, could share the same mechanism maintaining the quasi-stationary wave in the aquaplanet. In spite of the results here presented, the SH, which is mainly ocean covered and features surface boundary conditions closer to those employed in the aquaplanet, seems the ideal region to start looking for quasi–stationary marginally stable waves. This will be investigated in the next chapters. The strong zonal asymmetries of the NH climate might instead limit the relevance of this mechanisms to the maintenance of circumglobal patterns. Nonetheless, specific cases as the NH summer 2007 (Blackburn et al., 2008), where a dynamical similarity with aquaplanets models is realised because a closed jet stream pattern is observed as a result of a negative NAO pattern, should be worth further investigation.

If the mechanism were important in the Earth's climate, it is of interest to understand whether climate models are able to correctly reproduce the spatial scale, the horizontal structure and the energetics of these patterns. If they could, this would represent an important validation of the model's ability to adequately simulate baroclinic processes, as marginally stable baroclinic

waves can be expected to be very sensitive to the overall error of the model. If they couldn't, it would be of interest to relate the mis-representation of the marginally stable waves to the other errors of the model. Moreover, remembering that these waves can in principle lead to a stationary pattern, it would be of interest to understand whether their misrepresentation could be itself source of systematic error in the simulated time mean state.

The research of quasi–stationary patterns in the Southern Hemisphere that can be interpreted according to the theory developed in the aquaplanet, and the analysis of the errors committed by AGCMs in simulating such patterns, will be the topics of the next two chapters.

Chapter 5

The Southern Hemisphere wave four and El Nino

In this chapter we analyse NCEP–DOE reanalysis to determine whether the marginally stable wave paradigm is appropriate for interpreting quasi–stationary waves in the Earth's climate. The analysis focuses on the SH austral summer. The choice of the season and of the hemisphere is motivated in sec. 5.1. The quasi–stationary component of the system, which projects on the zonal wavenumber four, is identified in sec. 5.2 by means of spectral analysis and empirical orthogonal function (EOF) decomposition. A novel index that allows to measure the power on the quasi–stationary wave four is introduced in sec. 5.3, and by inspecting its interannual variability a potential link between the wave growth and El Nino is suggested. In sec. 5.4, the relationship between El Nino and the quasi–stationary wave four is further analysed according to the theory of the marginally stable wave developed in the aquaplanet model. A final discussion is given in sec. 5.5.

5.1 The Southern Hemisphere climate

Southern Hemisphere is for the 80% ocean covered. The Andes, the South African and the Antarctic plateau, which are the dominant orographic fea-

tures of the hemisphere, are substantially smaller than those of the Northern Hemisphere. The Antarctic continent, which is the biggest land area after South America, is distributed in a zonally symmetric shape around the South Pole. The latitude band between 40S and 60S is almost free of land, so that the low level westerly atmospheric flow proceeds strong and zonally oriented over the whole Southern Ocean. The time averaged stormtrack, which refers to a region of enhanced baroclinicity where extratropical cyclones preferentially grow and propagate, is located near 50S and, despite being more intense over the southern Atlantic and Indian oceans, it has a predominantly circular and zonally oriented structure (Trenberth, 1991). All these characteristics make the Southern Hemisphere climate more zonally symmetric than the Northern Hemisphere one, where orography and land–sea contrast excite vigorous stationary waves and lead to the formation of localised stormtracks over the Pacific and Atlantic oceans.

The seasonal cycle can lead to some relevant changes in the specific location and orientation of the stormtracks of the SH. In particular, the austral winter (JJA) is characterised by a peculiar double jet structure. A subtropical jet, which ranges from Australia to central South America at about 30S, forms next to an extratropical eddy-driven jet which ranges from South America to Australia at about 50S. The two jets, rather than being perfectly zonally oriented, are slightly tilted toward the pole, so that baroclinic wave activity is predominately organised along two spiralling stormtracks which from the Pacific and Atlantic oceans respectively converge toward a subpolar wave guide (Berbery and Vera, 1996; Chang and Yu, 1999; Rao and Carmo, 2002; Hoskins and Hodges, 2005). Inatsu and Hoskins (2004) investigated the reasons for the observed zonal asymmetries of the JJA SH climate, and they attributed to the latent heat released in the South–Asia monsoon the energy source forcing a stationary Rossby wave propagating in the SH. The Rossby wave, in turn, creates preferential regions for the development of baroclinic unstable waves, thus leading to the peculiar distribution of the stormtrack described above.

The austral summer (DJF) features instead a well defined, circular, high latitude stormtrack, which is located near 45S and which is notably stronger in the Atlantic and Indian sectors (Trenberth, 1991; Hoskins and Hodges, 2005). Therefore, the SH climate is much more zonally symmetric during the summer season than during the winter one. Moreover, the equator to pole SST differences used to perform the experiments in the aquaplanet (maximum $\Delta_T = 27$) are more reminiscent of typical summer like conditions, and the idealised experiments performed by (Chang and Yu, 1999) suggest that a weaker average baroclinicity enhances the temporal coherence of extratropical wave packets. The SH austral summer seems therefore a good testbed to look for the development of quasi–stationary marginally stable baroclinic waves.

5.2 Southern Hemisphere extratropical waves

5.2.1 Spectra

The spectral approach that has been adopted to identify the marginally stable quasi stationary waves in the aquaplanet, will be now used again to look for the presence of such waves in the Southern Hemisphere austral summer. Fig. 5.1a–b show the Hayashi spectral power in the meridional velocity at 200mb and the cospectral power in the vertical heat transport at 500mb respectively. The data has been previously meridionally averaged in the 30°S–60°S latitudinal band, so that the signals associated to zonally propagating wave packets in the extratropical jet are better highlighted. The plotting conventions are the same as those adopted in the previous chapters.

The PSD function of V at 200mb is less precisely distributed along a well defined non dispersive dispersion relation respect to what we have observed in the aquaplanet (compare with Fig. 3.3a), and in particular it misses the clear streak of peaks that characterised the aquaplanet extratropical spectrum. Nonetheless it is possible to identify a preferential region of the spectral space where the PSD is slightly more concentrated. This is highlighted by

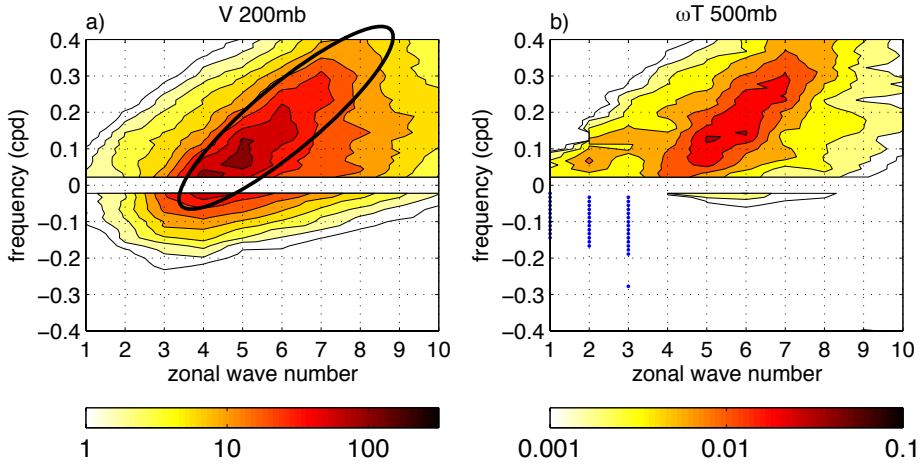

Figure 5.1: Hayashi Power spectrum of V at 200mb (a) and cospectrum of the vertical heat transport (b), for the meridionally averaged wave in the 30°S–60°S latitudinal band. The spectra are computed on DJF data from NCEP–DOE reanalysis in the time period 1979–2009.

the ellipse plotted in Fig. 5.1a, and it is consistent with the signature of eastward propagating wave packets. The dispersion relation covers the zonal wavenumber interval from $k = 4$ to $k = 7$, and it features two distinct maxima in the spectral power. One is located on a quasi–stationary k=4 component and the other on an eastward propagating component, of period approximately equal to 12 days, which projects on k=5. The distribution of the PSD on k=5 is consistent with the ubiquitous low frequency wave five observed by (Salby, 1982) during the austral summer 1978–1979.

The baroclinic nature of the dispersion relation found in the spectrum of V at 200mb is confirmed by analysing the cospectrum of the vertical heat transport at 500mb, which is plotted in Fig. 5.1b. Using this diagnostic, the dispersion relation gets very well defined and clearly resembles the organisation of spectral power along the *main dispersion relation* previously observed in the aquaplanet model (compare with Fig. 3.3b). In particular, the k=4 wave is the longest spectral component of the dispersion relation vertically transporting heat, and it could therefore be interpreted, in agree-

ment with the theory developed for the aquaplanet, as a marginally stable quasi–stationary baroclinic component. Differently from what speculated by other investigators (Watanabe, 2005), the wave five component of the SH austral summer is properly unstable and, despite the dynamical and structural similarities, it is energetically different from the quasi–stationary wave activity observed in the aquaplanet model.

5.2.2 EOF analysis

To investigate the structure of the k=4 wave, we now compute an Empirical Orthogonal Function (EOF) analysis of the DJF filtered meridional velocity at 200mb (Navarra and Simoncini, 2010). The EOF is area weighted by the cosine of the latitude (North et al., 1982) and it is defined over the same spatial domain (30°S–60°S) that we have previously adopted for spectral analysis. The daily V at 200mb has been preprocessed by a 30 days low pass Lanczos filter with 101 weights (see Appendix D), which retains in the filtered data the frequency range where the spectral power of the wave four is mainly distributed. Moreover, the anomalies are computed with respect to the seasonal mean of each year, so that only contributions from intraseasonal variability participate to the EOF decomposition. The resulting sequence of DJF data, over the 1979–2009 period, constitute the time series which is effectively analysed. Thanks to this methodology, the first EOFs, which can be interpreted as the preferred spatial patterns of covariability across the given domain, are expected to provide information on the horizontal structure of the quasi–stationary wave four.

Homogenous correlation maps are used to picture the patterns associated to the first and the second EOF. In this representation technique, the principal component (PC) of the EOF is correlated, at each grid point, with the time series of the analysed field at that grid point. The correlation map can therefore give informations on the structure of the pattern even outside of the domain of analysis. In particular, in Fig. 5.2 we plot the resulting maps over the whole SH. As expected, the first two EOFs, which are approximately

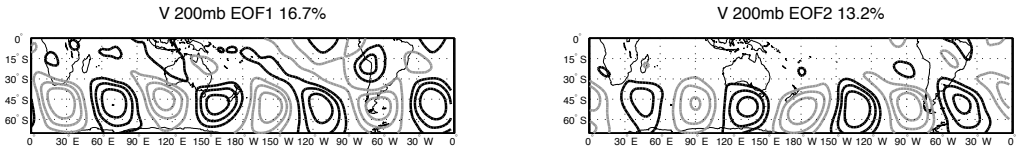

Figure 5.2: Homogeneous correlation maps of the first two EOFs computed on the DJF low pass filtered V at 200mb over the 30S–60S latitude band. The explained variance is added to the titles. See the text for more details about the methodology.

in spatial quadrature and well confined to the extratropical baroclinic band, are characterised by a signal with a zonal wavenumber four. This could be consistent with the feature of a propagating wave.

To verify this hypothesis, we have computed the cross-correlation function between the first and the second PCs, and the result is presented in Fig. 5.3a. The grey lines indicate the two sigma interval of confidence, which has been computed by the moving block bootstrap technique (Efron and Tibshirani, 1993), using a block length equals to the time interval between effectively independent samples (Trenberth, 1984). The values of the cross-correlation function are relatively small and a maximum value of only about 0.25 is observed at lag equals ± 12 days. Statistical significant values are however found on the lag interval from 5 to 20 days. Moreover the function is odd, and because positive (negative) values are observed on positive (negative) lags we can expect that, at least episodically, the first two EOFs compose the orthonormal phases of an eastward propagating wave.

The slightly propagating nature of the wave four could have also been identified from Fig. 5.1a, as the PSD is more concentrated on the positive rather than on the negative frequencies. To estimate its average period of propagation, on Fig. 5.3b we plot the normalised quadrature spectrum between the PC1 and PC2 time series. The quadrature spectrum has been separately computed on each austral summer, and the average spectrum is presented. Grey lines give the two sigma standard deviation interval. The

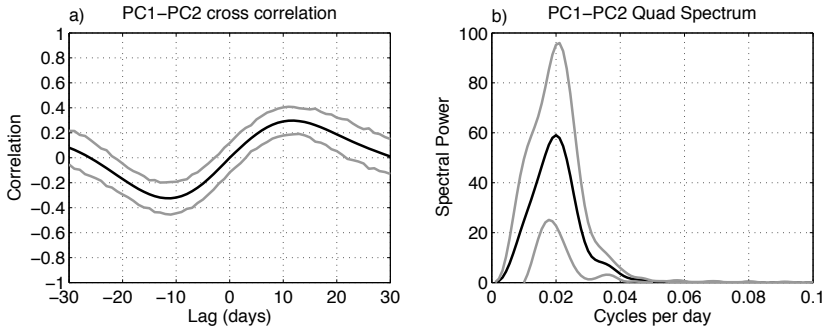

Figure 5.3: Cross correlation function (a) and quadrature spectrum (b) between the PC1 and the PC2 associated to the two EOF patterns shown in Fig. 5.2. Grey lines indicate 2 sigma confidence level.

spectral power is bell shaped and peaks around 0.02 cycles per day. This is approximately equal to a period of 50 days, thus confirming the very slowly eastward propagating average character of the wave four.

Correlating the PCs with v at 200mb allowed to picture the horizontal structure of the EOFs. Further informations on the structure of the patterns can be gathered by correlating the PCs with other fields and with different levels. Using this approach, we have examined the vertical phase tilt with height of the meridional velocity and of the temperature fields which, has we've seen in the aquaplanet (see sec. 4.1.1), is a basilar feature of baroclinicity. The vertical structure of the two EOFs (not shown) feature a weak baroclinic tilt that is well defined over the whole troposphere, with the overall picture being similar to what is shown in Fig. 4.1b for the aquaplanet wave five.

5.3 The propagating power index

The quasi–stationary waves observed in the aquaplanet model feature an impressive temporal coherence, as the propagation of their phase could be tracked for a timescale of the order of months. Whether such a property is

shared by the slowly eastward propagating wave four identified in the SH has not been proved yet. To answer this question, we have introduced an index that measures the propagating power of the wave four associated to the EOFs patterns displayed in Fig. 5.2.

The definition of the index, which will be shortly specified, is motivated by the following arguments. A 2D (space–time) signal $v(x,t)$, which contains for the sake of simplicity a single wave in the zonal direction of wavenumber k, can be decomposed in the sum between its sine and cosine zonal expansion as follows:

$$v(x,t) = \sum_m A_m \cos(kx - \omega_m t) = \tag{5.1}$$

$$= \sum_m \underbrace{(A_m \cos(\omega_m t))}_{\mathrm{C(t)}} \cos(kx) + \sum_m \underbrace{(A_m \sin(\omega_m t))}_{S(t)} \sin(kx), \tag{5.2}$$

where m is an index over a discrete set of frequencies, and $C(t)$ and $S(t)$ are the timeseries of the cosine and sine zonal expansion, respectively. The Quadrature spectrum between $C(t)$ and $S(t)$ (see appendix C.1) gives:

$$Q_m(C(t), S(t)) = A_m^2/2, \tag{5.3}$$

so that after integration over the whole range of frequencies, it gives the power of the propagating wave in the analysed time period. The reasoning is not altered if two EOF patterns are considered in place of the sine and cosine function, and the respective principal components in terms of the $C(t)$ and $S(t)$ timeseries. Therefore, at each timestep, the propagating power index ($I(t)$) is defined as the frequency integrated quadrature spectrum (Q_m) between the PC1 and PC2 time series on a 45 days long window centered at that timestep:

$$\widehat{PC1}(t;\hat{t}) = PC1(t), \qquad t \in [\hat{t} - 22, \hat{t} + 22] \tag{5.4}$$

$$\widehat{PC2}(t;\hat{t}) = PC2(t), \qquad t \in [\hat{t} - 22, \hat{t} + 22] \tag{5.5}$$

$$I(\hat{t}) = \sum_m Q_m(\widehat{PC1}(t;\hat{t}), \widehat{PC2}(t;\hat{t})), \tag{5.6}$$

where $\widehat{PC}(t, \hat{t})$ is the restriction of $PC(t)$ to the 45 days window centered on $\hat{t}$, and Q_m is computed on the variable t.

The time series of the index over the 30 analysed austral summers is plotted in Fig. 5.4. The line is discontinuous, as the index only covers the DJF season of each year. As expected, the index on average features positive values, which is necessary for the wave being eastward propagating. More interestingly, strong and coherent eastward wave propagation occurs in an episodic fashion. In particular we observe that during the austral summers 87-88, 95–96 and 97–98 the index features very high values, which are well exceeding the two standard deviation threshold indicated by the dotted horizontal line added to the figure. Two of these episodes, namely the 87-88 and the 97–98, feature a growing power during the course of the season, and they happen in correspondence of two of the strongest El Nino events on the time series (Trenberth, 1997). Whereas also other El Nino events are associated to a growing power of the wave (i.e. 91–92, 93–94, 04-05, 06-07), the very strong 82–83 El Nino episode features relatively small values of the index.

A qualitative picture of the coherent propagation on k=4 , can be gathered by looking at the strongest episode on the time series. Fig. 5.5 shows the Hovmöller diagram of v at 200mb meridionally averaged in the 40°S–60°S latitude band during the 97–98 austral summer. A wave four, which features a remarkable temporal coherence and a very slow eastward propagation, is well visible in the diagram. The amplitude of the signal, consistently with the monotonic growth of the index, is stronger on the second half of the season. When analysing the Hovmöller diagram of the same field computed during the other episodes of strong wave four activity, we observe a similar slowly propagating pattern whose coherence is only maintained for approximately one month.

These results confirm that the wave four activity during the austral summer in the SH is analogous to the quasi–stationary wave activity studied in the aquaplanet, with the exception than it is episodic and that it preferentially forms as a very slowly eastward propagating pattern. Moreover, if the

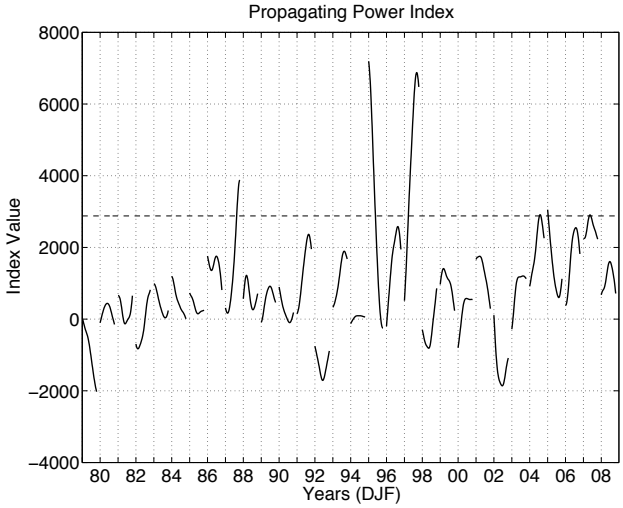

Figure 5.4: Time series of the power of the propagating wave four during 30 austral summers from december 1979 to february 2009. The line is discontinuous as only data from the DJF months of each year are plotted. For instance, the piece of line going from label 97 to label 98 refers to the index values during the 97–98 DJF season. The horizontal dotted line indicates the 2 sigma level.

aquaplanet results apply, the process is eminently extratropical. Nonetheless, we've already noted from a qualitative inspection of Fig. 5.4 that the growth of the pattern could be favoured by the tropical SST conditions associated to El Nino. The seasonal growth of the pattern can be quantified as the difference between the last and the first value in the propagating power index during each DJF season. Let's call DPP the resulting interannual index. To quantify the statistical robustness of the relationship between ENSO and the wave four growth, we now compute, for each grid point, the interannual correlation between the DJF seasonal averaged OLR and the DPP index. The resulting correlation map is shown in Fig. 5.6. Bootstrap resampling is used for estimating the significance level, and correlation values statistically significant at the 5% level have been shaded.

The typical OLR pattern associated to ENSO, which is characterised by

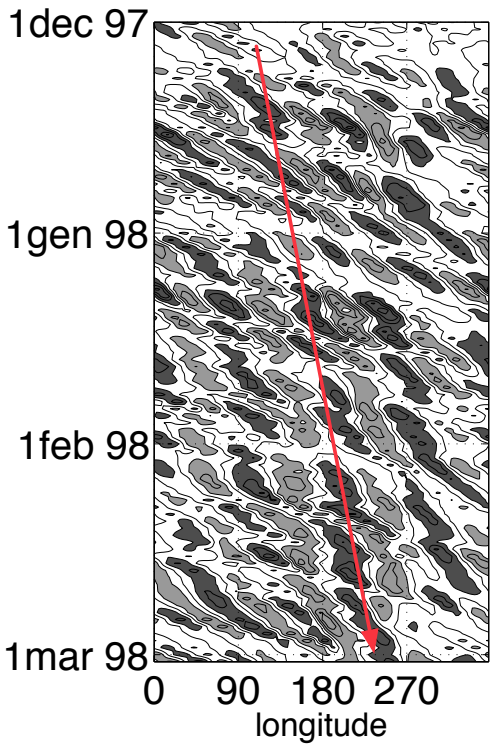

Figure 5.5: Hovmöller diagram of v at 200mb meridionally averaged in the 40°-60° latitude band from December 1997 to March 1998. The contour interval is 10 m/s and a dark (light) shading is applied on values greater (smaller) than +10 m/s (-10 m/s). The red arrow indicates the propagation of the wave four pattern.

opposing OLR anomalies between the central and the west tropical Pacific is found in Fig. 5.6. This result increases the confidence that El Nino can, on a statistical basis, favour the organisation of extratropical baroclinic activity on a quasi–stationary k=4 wave. Of course, direct experimentation with an AGCM would be important to dynamically asses the relation of causality between ENSO and the wave four. Nonetheless, as we will note in the next chapter, no model, among those examined, is able to correctly capture the structure of the quasi–stationary wave four. This might preclude experimentation as a valuable approach. More interestingly, the theoretical framework developed in the aquaplanet model suggests some approaches to evaluate whether a relationship between El Nino and growing power on a quasi–stationary wave four could be physically plausible. This is discussed in the next section.

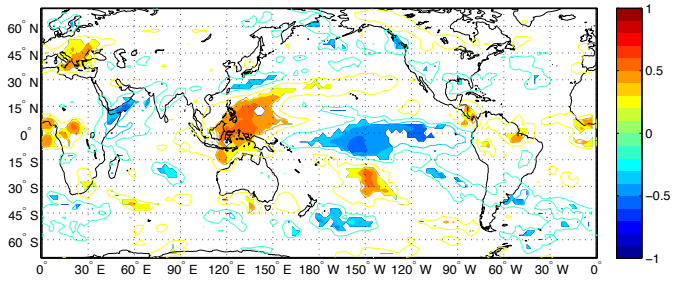

Figure 5.6: The map displays, at each grid point, the temporal correlation between the DJF seasonal averaged OLR at that grid point and the DPP index. See text for details. Contour interval is 0.2, and shading is applied when correlation is statistically significant at the 5% level.

5.4 Can El Nino favour the marginally stable wave four?

As well known, ENSO is the most important climatic signal on the inter-annual timescale, and it is the result of a coupled instability of the tropical atmospheric-oceanic system (Philander, 1990). Its positive phase, namely El Nino, is associated to a warming of the SST in the equatorial east pacific and to a displacement of the precipitation from the maritime continent toward the tropical central pacific. This leads to many changes also in the tropical and extratropical atmospheric circulation.

Many indexes (Trenberth, 1997) have been introduced for measuring the state of ENSO. Here we will identify its state from the SST anomalies in the Nino 3.4 region, which is a box extending over 5N–5S and 120W–170W. SST anomalies in this region are considered crucial for forcing changes in the atmospheric circulation, via anomalies in the tropical convection. Therefore, El Nino will be considered occurring if the three months running mean of the average SST anomaly in the Nino 3.4 region exceeds the threshold of +0.5 degrees for at least five consecutive months. Anomalies are computed with respect to the 1971–2000 base period. Nine El Nino years are selected by this metrics in the analysed period (82–83, 86–87, 87–88, 91–92, 94–95,

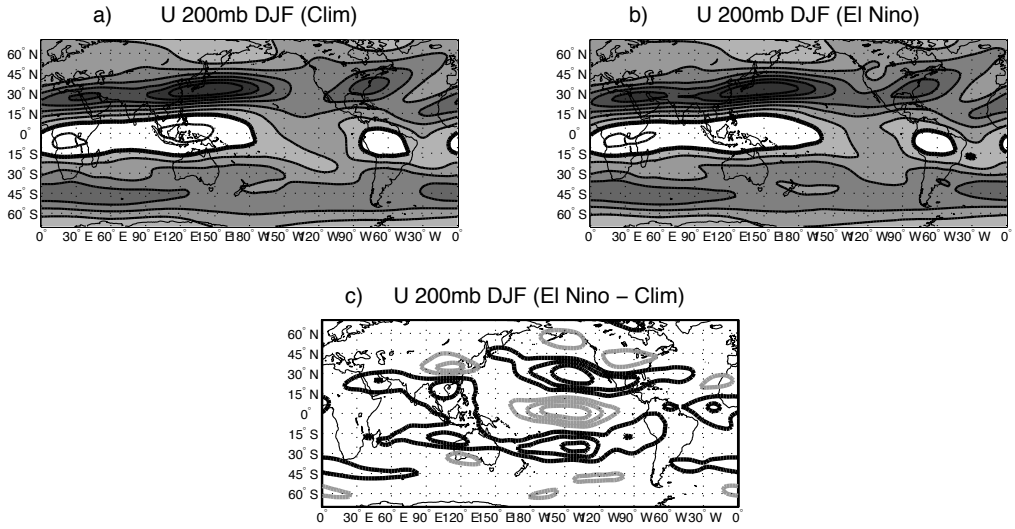

Figure 5.7: Climatological DJF zonal wind at 200mb (a) and composite of the same field during El Nino years (b). A darker shading is applied every 10 $\mathrm{m\,s^{-1}}$ on westerly wind regions. The difference between (b) and (a) is shown in fig (c), where c.i. is 2 $\mathrm{m\,s^{-1}}$ and dark (grey) lines refer to positive (negative) anomalies. The zero contour line is omitted.

97–98, 02–03, 04–05, 06–07). Composites of the DJF seasonal mean during the selected El Nino years will be used to picture the average state of the atmosphere associated to the positive phase of ENSO.

We start the analysis looking at how the upper tropospheric zonal wind is affected by El Nino. In Fig. 5.7a–b we plot the DJF seasonal mean zonal wind at 200mb and the composite of the same field during El Nino years, respectively. The difference between the composite and the climatological state is plotted in Fig. 5.7c. It is found that El Nino leads to easterly anomalies in the central tropical Pacific and to stronger westerly winds at the subtropical latitudes over the Pacific and Indian sectors of both hemispheres. This favours the development of a weak but well defined subtropical jet in the South Pacific. Moreover, the SH extratropical jet stream, which runs from South America to Australia, gets slightly reinforced and displaced toward the equator.

As discussed in sec. 1.2.2, the meridional curvature of the zonal wind is a relevant parameter controlling the Rossby stationary wavenumber (K_s) and the kinematic of Rossby waves. Because the anomalies in U at 200mb associated to El Nino have a meridional scale smaller than the width of the main jet stream, they could lead to significant changes in K_s. This is analysed in Fig. 5.8 where we compare the Rossby stationary wave number at 300mb computed on three different DJF mean states: the climatology, the composite over El Nino years, and the 97–98 season. The grey shading refers to regions where $K_s < 0$ and Rossby wave propagation is precluded. In the tropics and in the polar region this is due to time averaged easterly winds, while in the subtropics is the result of an inversion in the meridional gradient of the absolute vorticity ($\beta - U_{yy} < 0$). The arrows added to Fig. 5.8a–c indicate the location and the approximate extension of upper tropospheric wave guides. These are identified as zonal bands featuring, at each longitude, a meridional relative maximum in K_s. In the climatological mean state (Fig. 5.8a), we only find a very short wave guide confined to the eastern Indian ocean. For the average conditions associated to El Nino (Fig. 5.8b), as a result of the strengthening of the subtropical and extratropical jet streams, the climatological wave guide extends over the whole Indian ocean, and a secondary small wave guide develops in the west Pacific. These changes are even more evident when the mean state of the 97–98 austral summer is considered (Fig. 5.8c), so that the resulting overall picture resembles one circumglobal wave guide extending over the whole SH. El Nino therefore leads to kinematic conditions which are more favourable for the circumglobal coherent recirculation of energy in wave packets. As discussed in sec. 3.4, this is considered of primary importance for the maintenance of the coherence of quasi–stationary baroclinc waves.

The effect of El Nino might not be limited to kinematics. The warming of SST in the east pacific leads to an enhanced overall latent heat release in the tropics, which, via enhanced Hadley cell overturning (see sec. 1.5), increases the average extratropical baroclinicity. These thermal changes are

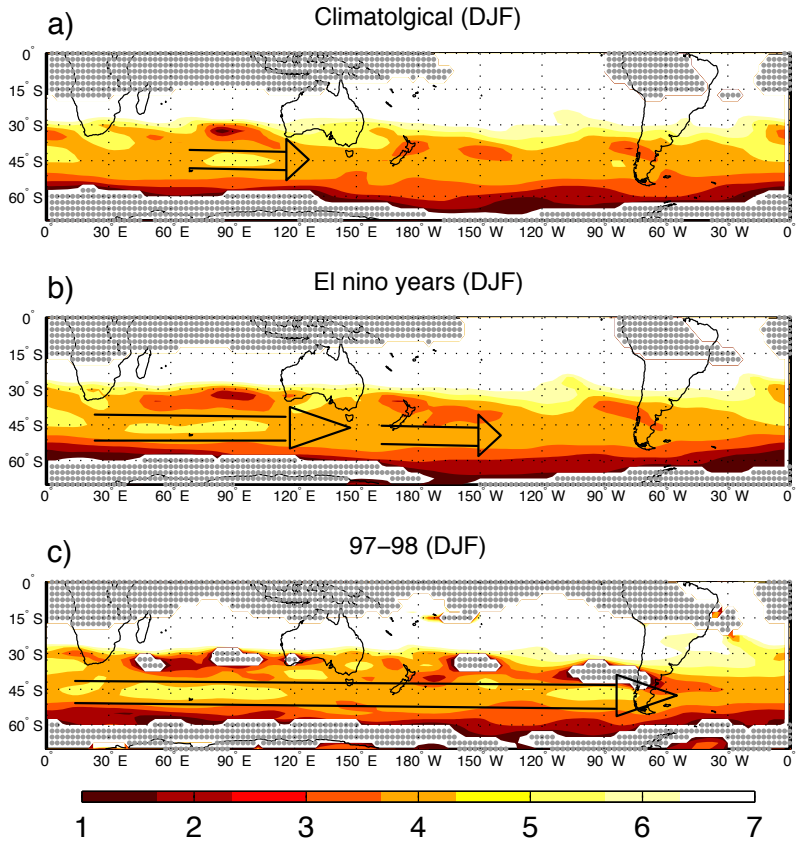

Figure 5.8: Rossby stationary wavenumber at 300mb computed for the DJF season on the following years: 1979-2009 mean state (a), the composite over only the El Nino years (b) and the 97–98 El Nino episode (c). The arrows approximately indicate the location of upper tropospheric wave guides.

confirmed in Fig. 5.9, which shows the meridional distribution of the anomalous DJF zonal mean temperature at 500mb in the composite of El Nino years, and during the 97–98 episode. Tropical and extratropical temperatures respectively increase and decrease, so that the time average baroclinicity of the system results effectively enhanced. This thermal forcing, which is particularly strong during the 97–98 episode, can favour the destabilisation of marginally stable waves, as the wave four, so that it can more efficiently grow by baroclinic processes.

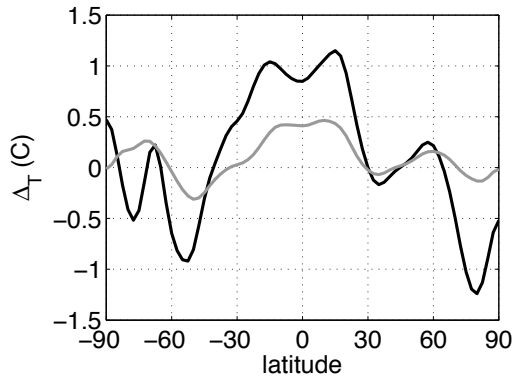

Figure 5.9: Anomalous meridional profile of the zonal mean temperature at 500mb during the 97–98 DJF season (black line) and the composite state over the nine El Nino events indicated in text (grey line). The anomaly is computed respect to the climatological 1979–2009 DJF values

5.5 Discussion

These results suggest that the two necessary conditions for the development of quasi–stationary activity found in the aquaplanet, namely a closed wave guide, which allows for the recirculation of energy, and a marginally stable baroclinic component, which provides the energy source maintaining the stationary wave, are favoured, in the real world, by the tropical forcing maintained by the positive phase of ENSO. Despite this does not rigorously prove the presence of a connection between El Nino and the development of slowly propagating patterns on k=4, it suggests a physically plausible mechanism, namely the destabilisation of a marginally stable component, which is worth further investigation. Analysing a longer time period using different reanalyses, so that more ENSO events are considered, might help to strengthen the connection on a statistical basis. Nonetheless, because of the weaker thermal constraints, due to the absence of satellite remote sensing, higher errors are known to affect reanalyses data in the SH prior to 1979 (Wang et al., 2006). Attention should be paid in considering whether upper tropospheric large scale fields are enough reliable for this purpose. Experi-

ments with an AGCM could be also considered. In particular, a parametric analysis of the dynamics and of the energetics of the extratropical SH quasi–stationary waves respect to changes of the SST in the NINO 3.4 region could be specifically performed. We will discuss in the next chapter whether the models examined in the thesis can be adequate for this purpose.

Low frequency patterns projecting on k=4 in the SH were identified thorough EOF decomposition by Kidson (1999), and later analysed by Revell et al. (2001). In particular, Revell et al. (2001) were looking for tropical energy sources sustaining the extratropical pattern by computing the divergent flow necessary to maintain the thermal wind balance of the rotational flow. As the divergent flow was found to be confined to the extratropics, they concluded that the pattern, which was interpreted as a barotropic Rossby wave, was not sustained by a direct tropical forcing. The extratropical nature of the wave is consistent with the interpretation given in this chapter. But in comparison to their work, we strongly pose the accent on the episodic slowly eastward propagating character of the pattern, which we find energetically consistent with the activation of a marginally stable baroclinic component. In particular, the barotropic Rossby wave paradigm would be inadequate for explaining the linkage with El Nino via increased Hadley cell overturning and strengthened extratropical baroclinicity.

We've shown that the pattern features a preferential eastward propagation. Nonetheless, during the analysed period, we also find three austral summers (79–80, 92–93, 02–03) where the wave four features a westward propagation and a relatively modest amplitude. During these years the tropics are as well characterised by El Nino, with the latter year featuring an event of moderate intensity and the others being instead rather weak (Trenberth, 1997). An increasing absolute value of the index during the course of the season is found again for the 79–80 and for the 02–03 episodes. As the phase speed of the pattern is in general very small, the occurrence of a slowly eastward or westward propagation could simply result because of small differences in the mean state of that season. Nonetheless, consistently with

our baroclinic paradigm, all the strongest signals are associated to a slowly eastward propagation of the pattern.

The sensitivity experiments performed on the aquaplanet model revealed that increasing the equatorial SST, while maintaining the equator to pole SST difference unchanged, is equivalent to increasing the average baroclinicity of the system, so that marginally stable components become progressively more unstable. Consistently, the warming of tropical SST, due to anthropogenic climate change (Trenberth et al., 2007), might force an increasing power in the quasi–stationary wave four. An inspection of Fig. 5.4 does not suggest that any strong trend in the propagating power index is occurring. Nonetheless, we note that since austral summer 04–05 the index has been featuring values notably higher than those at the beginning of the dataset. In the future, repeating the analysis on a longer time series will be of interest for understanding whether global warming could destabilise the quasi–stationary wave four. In the meanwhile, some preliminary indications could be gathered by applying the same analysis on the output from climate model simulations under climate change scenarios.

Chapter 6

Systematic errors in AMIP simulations

This chapter provides an analysis of the errors of the ECHAM5 AGCM, set–up in AMIP configuration, in simulating the quasi–stationary wave activity characterising the Southern Hemisphere austral summer. The model is tested at three different spatial resolutions, and the errors are individuated as differences from the statistics computed on NCEP–DOE reanalysis. In sec. 6.1, we first determine the error in the simulated mean state of the model. A simple but effective technique of estimating the spectral energetics of extratropical waves as a function of their meridional scale is introduced in sec. 6.2. We then move to applying this technique for analysing the overall error in the energetics of baroclinic waves (sec. 6.3), and, more specifically, in the energy sources of the quasi–stationary waves four and five (sec. 6.4). To increase the robustness of the results, a comparison with ERA–INTERIM reanalysis is also shown. The spatial structure of the quasi–stationary patterns forming in the model is identified in sec. 6.5 via EOF analysis. Finally, in sec. 6.6, we discuss how the errors in the representation of quasi–stationary patterns can be related to other systematic errors of the model.

6.1 Mean state Intercomparison

The mean state of the atmosphere is a climate property of primary importance, and it is the fundamental diagnostic used to identify systematic errors of climate models. Analysing the errors in the simulated mean state is particularly important when dealing with quasi–stationary processes, which, as we have seen in the previous chapters, are deeply influenced by the baroclinicity and by the wave guides of the time averaged state of the atmosphere.

We therefore now analyse the time mean state (DJF) of the atmosphere simulated by the ECHAM5 AGCM setup in AMIP configuration at three different spatial resolutions: T31L19, T42L31 and T106L31. The configuration of the model has been described in sec. 2.2.1 and the errors are identified as differences with the correspondent climate statistics computed on NCEP–DOE reanalysis. For each experimented resolution, three members ensemble averages are presented. The analysis is focused on the Southern Hemisphere and on few selected variables —namely [U], U 200mb, V 200mb – which are of importance for later interpreting the errors in the dynamics and in the energetics of the quasi stationary waves simulated by the models. A more detailed description of the model systematic error as a function of the model resolution can be found in Roeckner et al. (2006).

Fig. 6.1 shows the DJF zonal mean zonal wind found in NCEP–DOE reanalysis and simulated by the set of performed AMIP experiments. Some remarkable differences, which are strongly function of the model resolution, are found in both the tropical and the extratropical wind field between the reanalysis and the model climatology. In particular, the simulated upper tropospheric tropical atmosphere rotates eastward instead of westward. This is a known bias of the model, which can be also identified in the results presented in Roeckner et al. (2006). In the SH extratropics, the simulated baroclinic jet is stronger, narrower and more equatorward displaced than what is found in NCEP–DOE reanalysis. The error committed with respect to these features can be better evaluated in table 6.1, where fundamental parameters defining the jet's structure are objectively quantified. In particular we compare the

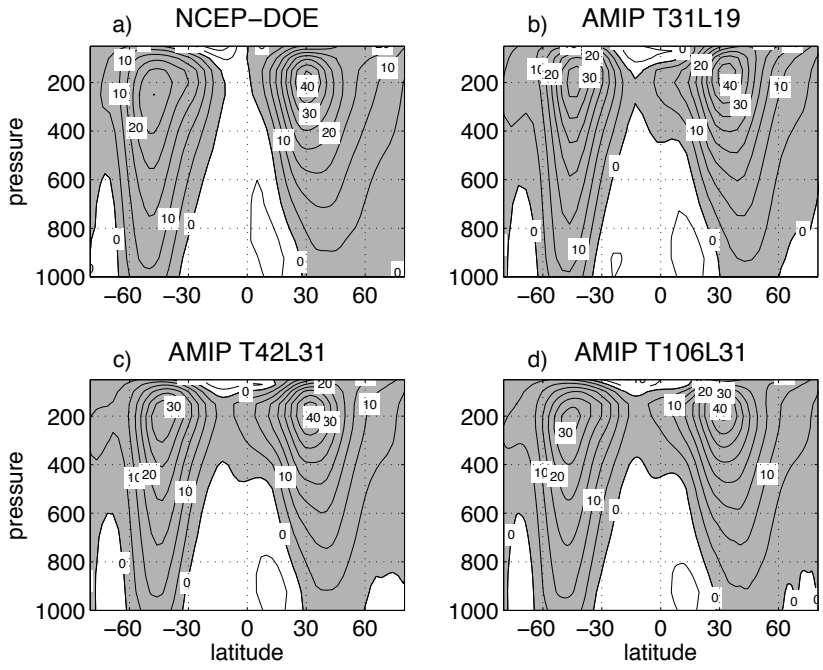

Figure 6.1: Meridional cross section of the climatological DJF zonal mean zonal wind computed on NCEP–DOE reanalysis (a), and on AMIP simulations at the resolutions (b) T31L19, (c) T42L31 and (d) T106L31. The reference period is 1979–2009. Contour interval is 5 $\mathrm{m\,s^{-1}}$ and westerly winds are shaded.

maximum wind speed in the SH jet (U_{max}), the latitude of the jet's maximum (φ_{max}), and the width of the jet (Δ_{jet}), which is defined as the latitudinal interval where the zonal wind, at the jet's level, is stronger than $U_{max}/2$.

Increasing the model resolution leads to remarkable improvements with regard to all the examined features of the extratropical SH jet. The highest improvement is observed in Δ_{jet}, whose relative error decreases from about 30% at T31L19 down to 3% at T106L31. A similar level of accuracy is reached in φ_{max}. The intensity of the jet is also substantially better captured by increasing the model resolution, despite the relative error remains higher than 5% even at T106L31.

	U_{max} (m/s)	φ_{max} (°)	Δ_{φ} (°)
T31L19	37.6 (25%)	42.7 S (10%)	22.3 (31%)
T42L31	34.9 (15%)	43.3 S (9%)	27.9 (14%)
T106L31	32.6 (8%)	45.4 S (4%)	31.4 (3%)
NCEP–DOE	30.1	47.5 S	32.5

Table 6.1: Comparison of fundamental parameters describing the SH jet between AMIP simulations and reanalyses: maximum wind speed (U_{max}), latitude of the jet's maximum (φ_{max}), and width of the jet (Δ_{φ}) defined as described in the text. The relative error is indicated in brackets.

The same comparison is now repeated for the DJF seasonal mean zonal wind at 200mb, which is shown in Fig. 6.2. This diagnostic is used to identify errors in the longitudinal distribution of the SH jet stream. At low resolution (T31L19) we observe that the jet is too zonally symmetric, and, rather than being confined to the Atlantic and Indian ocean sectors, it extends over the whole SH. Only slight weakening is found over the central Pacific. The T42L31 model correctly captures the weakening of the jet stream in the central pacific, but the jet remains too strong over the east and the west Pacific. Finally, the high resolution model gives a better picture of both the intensity and the location of the jet, despite the zonal confinement in the Atlantic–Indian sector is still not perfectly captured.

In chapter 5, we've discussed about the importance of the El Nino induced strengthening of the subtropical jet located east of Australia for enhancing the temporal coherence of the quasi–stationary wave four. The subtropical jet, despite being rather weak, can be also identified in the DJF climatology shown in Fig. 6.2a, where a relative maximum in U at 200mb is found just east of Australia. At T31L19 and T42L31 (see Fig. 6.2b–c) the model is not able to reproduce this specific feature and no zonal jet is in general observed over the subtropics. An improvement is instead found at T106L31 (Fig. 6.2d), as the model features a relative maximum in the zonal wind just north of

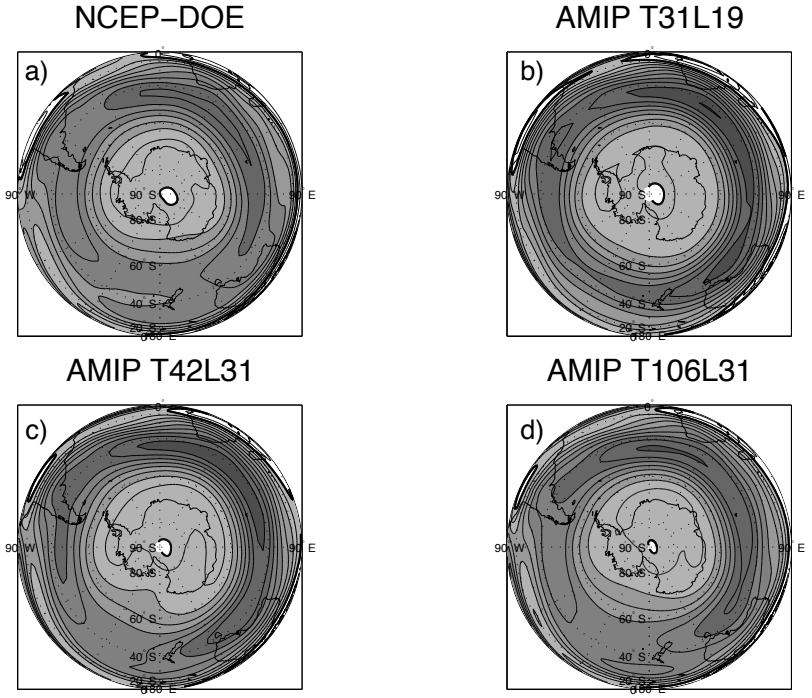

Figure 6.2: Climatological zonal wind at 200mb for the same data analysed in Fig. 6.1. Contour interval is 10 m/s, and a darker shading is applied every 20 m/s on westerly wind regions. The zero wind line is displayed thicker

New Zealand, whose location is roughly consistent with the subtropical jet found in reanalyses.

The climatological DJF meridional wind at 200mb, which is shown in Fig. 6.3a–d, is now used to evaluate whether AMIP simulations can correctly reproduce the stationary wave pattern of the SH. As expected from the elevated zonal symmetry of the SH boundary conditions, the amplitude of the stationary waves is rather weak, i.e. 1–6 meters per second. We find that the qualitative structure of the pattern is well captured, while the performance of the models in simulating the location and the intensities of the various centres of action should be evaluated on a case by case basis. For instance, the arrow added to Fig. 6.3b indicates a centre of action of positive meridional velocity which is absent in NCEP–DOE reanalysis. This feature is as well found at

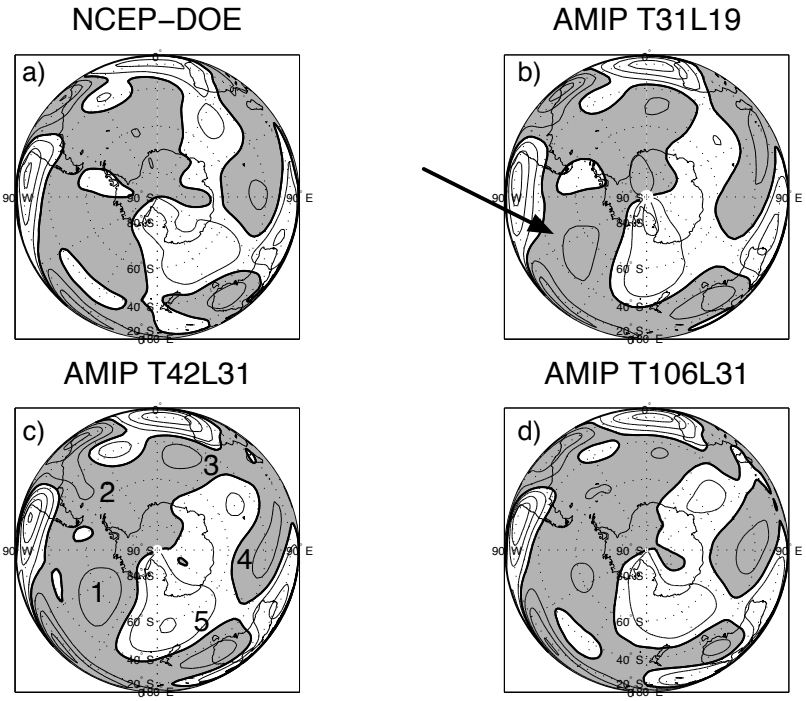

Figure 6.3: Climatological meridional wind at 200mb for the same data analysed in Fig. 6.1. Contour interval is 3 m/s. Positive values are shaded.

T42L31, where it participates to a kind of circumglobal wave five pattern, whose centres of action have been enumerated for clarity in Fig. 6.3c. In particular, the centres named 1, 2 and 3 are almost absent in NCEP–DOE reanalysis. With regard to this feature, a marked improvement is observed at T106L31. We will later discuss whether this systematic error might be generated by mechanisms similar to what sustains the quasi–stationary patterns of the aquaplanet model.

We have shown that low resolution models are affected by significant systematic errors in the simulation of the time mean zonal wind field. Marked improvements are instead found in the high resolution one. This is likely subsequent to a better representation of extratropical baroclinic processes. In fact, as discussed in sec. 1.2, the meridional heat transport associated to the growth of baroclinic waves and the horizontal momentum convergence,

in their barotropic decay, are the two fundamental processes determining the characteristics of the time mean extratropical thermal structure. This will be later verified, using the method introduced in the next section.

6.2 The Method

As Hayashi spectra (Hayashi, 1971, 1980) have proved to be a powerful technique for analysing extratropical atmospheric variability, they're now going to be used again for the evaluation of the errors of AGCMs. In Appendix C.3 and C.4, we give a detailed description of the method we've introduced to perform the analysis. This is based on the spectral kinetic energy balance (Hayashi, 1980) which has already been introduced in section 4.1.3 to prove the baroclinic nature of the wave five in the aquaplanet. Differently from the approach adopted for the aquaplanet, where global integrals of the energy conversion were considered, we now integrate the spectral energy balance meridionally in the 30S–60S latitude band and vertically between 1000mb to 100mb. If we call φ_N and φ_S respectively the northward and the meridional borders of integration, and p_t and p_b the upper and the lower pressure levels, the integrated spectral energy balance equation can be written as:

$$0 = \int_{\varphi_S}^{\varphi_N} \int_{p_t}^{p_b} ((< K \cdot K >_k^\nu + < K_0 \cdot K_k^\nu > - P_k^\nu(\alpha, \omega) + D_k^\nu) W_\varphi d\varphi dp) + F_k^\nu, \tag{6.1}$$

where

$$F_k^\nu = -\frac{\cos\varphi_N P_k^\nu(\phi, v)_{\varphi_N} - \cos\varphi_S P_k^\nu(\phi, v)_{\varphi_S}}{r[\sin(\varphi_N) - sin(\varphi_S)]} + \{P_k^\nu(\phi, \omega)_{top} - P_k^\nu(\phi, \omega)_{bot}\}_{\varphi_S}^{\varphi_N} \tag{6.2}$$

is the kinetic energy tendency due to fluxes of energy at the boundaries of the integration region, and

$$W_\varphi = \frac{\cos\varphi}{\sin\varphi_N - \sin\varphi_S}, \tag{6.3}$$

is the weight of the area element. This term is dominated by the equatorward dispersion of waves escaping out of the baroclinic band, as the propagation of waves toward the pole and toward stratosphere is in general much weaker.

Focusing on a zonal band allows not only to be consistent with the results shown in chapter 5, but also to analyse the spectral balance as a function of the meridional scale of the waves. Let's introduce the following operators: $\{\,\}$ is the meridional area weighted average in a latitudinal band, and $\tilde{}$ is the deviation from the meridional average. A generic field (ζ) can be therefore rewritten as $\zeta = \{\zeta\} + \tilde{\zeta}$. This simple approach allows to decompose the terms in eq. 6.1 between the contributions from the meridionally averaged wave, and from the waves not projecting on the meridional average. We will adopt the following conventions:

$$\int_{\varphi_S}^{\varphi_N}\int_{p_t}^{p_b} < K\cdot K >_k^\nu W_\varphi d\varphi dp =< \{\{K\}\cdot\{K\}>_k^\nu + \{< \tilde{K}\cdot\tilde{K} >_k^\nu\}$$

$$\int_{\varphi_S}^{\varphi_N}\int_{p_t}^{p_b} < K_0\cdot K_k^\nu > W_\varphi d\varphi dp =< \{\{K_0\}\cdot\{K\}_k^\nu > + \{< \tilde{K_0}\cdot\tilde{K_k^\nu} >\}$$

$$\int_{\varphi_S}^{\varphi_N}\int_{p_t}^{p_b} P_k^\nu(\alpha,\omega) W_\varphi d\varphi dp = P_k^\nu(\{\alpha\},\{\omega\}) + \{P_k^\nu(\tilde{\alpha},\tilde{\omega})\},$$

where the first and the second terms on the rhs are the contributions by the meridionally averaged wave and by the waves not projecting on the meridional average, respectively.

The decomposition is somehow arbitrary, as specific extratropical cyclones or wave packets will in general project on both the components, but it is however useful because it works as a filter on the meridional scale of the waves. In particular, as demonstrated in appendix C.4, if L is the width of the latitudinal band, and Δ_φ is the meridional wavelength of the disturbance we find that:

$$\Delta_\varphi \geq 2L \longrightarrow \text{energetics projects on the } \textit{mean} \tag{6.4}$$

$$\Delta_\varphi \leq L \longrightarrow \text{energetics projects on the } \textit{deviation from the mean} \tag{6.5}$$

Before moving to analysing the errors of the model, we now discuss three different approaches that can be used for describing the average kinetic energy in the 30S–60S latitudinal band in NCEP–DOE reanalysis. Vertical integration is also performed on eight pressure levels from 1000mb to 100mb. The total kinetic energy $\{(v^2+u^2)/2\}$, the kinetic energy due to meridional

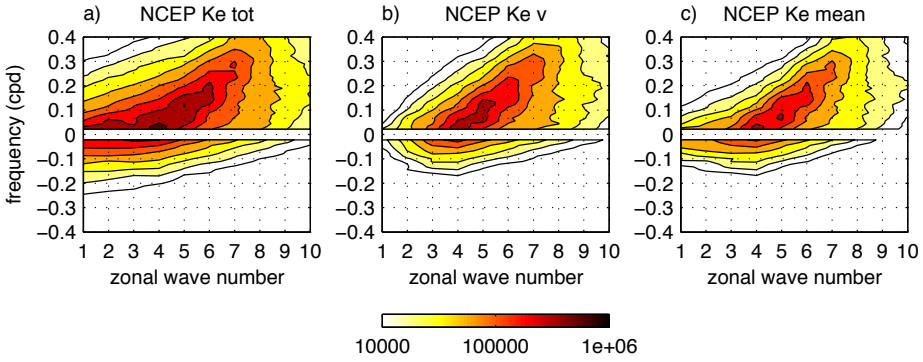

Figure 6.4: Kinetic energy spectra of the DJF wave activity in the 30S–60S latitudinal band as pictured by NCEP–DOE reanalysis. Three slightly different approaches are shown: (a) the total kinetic energy $\{(v^2+u^2)/2\}$, (b) the kinetic energy due to meridional motions $\{v^2\}/2$ and (c) the total kinetic energy of the meridionally averaged waves $(\{v\}^2+\{u\}^2)/2$. Units are $\mathrm{m^2\,s^{-2}}$ day, and four contours are plotted every order of magnitude

motions $\{v^2\}/2$ and the kinetic energy of the meridionally averaged waves $(\{v\}^2+\{u\}^2)/2$ are plotted in Fig. 6.4a–c and will be respectively named as method *a*, *b* and *c*. All the three diagnostics can identify the dispersion relation terminating on a quasi–stationary k=4 wave, which has been matter of investigation in chapter 5. Nonetheless the dispersion relation is clearer using methods *b* and *c*. This confirms that meridional velocity (method b) is an excellent diagnostic for identifying quasi–stationary marginally stable waves. Moreover the dispersion relation is constituted of waves featuring a meridional scale roughly comparable to the width of the extratropical baroclinic band (method c).

The similar distribution of PSD between the positive and the negative frequencies we observe on low zonal wavenumbers ($k < 4$) in Fig. 6.4a can be interpreted as meridional fluctuations in the jet stream latitude. The variability of the jet stream is obviously filtered considering only the kinetic energy by meridional motions (Fig. 6.4b), and is highly damped by previously applying a meridional average to the data (Fig. 6.4c). Because the jet stream is

spectrally equivalent to a zonal wave with almost fixed zonal nodes, its fluctuations appear as standing oscillations, which in Hayashi spectral analysis are represented by the sum of an eastward and a westward propagating wave of equal amplitude and period:

$$A\cos(kx)\cos(\omega t) = \frac{A}{2}(\cos(kx-\omega t) + cos(kx+\omega t)). \tag{6.6}$$

This explains the symmetry of the PSD between positive and negative frequencies found in Fig. 6.4a.

6.3 Extratropical waves

In the previous section it has been shown that the energetics of the meridionally averaged waves is a good diagnostic for identifying the quasi–stationary marginally stable waves of the system. This is therefore the first approach we will adopt for analysing the errors in the simulation of extratropical baroclinic processes. The analysis will be later complemented by looking at the waves not projecting on the meridional average, so that a comprehensive and objective picture of the energetics of extratropical waves can be gathered.

6.3.1 Energetics of the mean waves

Fig. 6.5 shows the kinetic energy spectra of the meridionally averaged waves in NCEP–DOE reanalysis and in AMIP simulations. The distribution of PSD found in the NCEP-DOE reanalysis is badly reproduced by the low resolution (T31L19) model. In particular, the simulated PSD is distributed along a too well defined dispersion relation which extends too far over the highest wavenumbers of the plotted spectrum. Moreover, it underestimates the PSD on $\nu < 0.1$ and $6 \leq k \leq 9$. This can be interpreted as a missing spectral broadening, which could result because of the bias in the upper tropospheric jet stream. As we've seen in Fig. 6.2a–b, the jet stream, instead of being confined into the Atlantic–Indian ocean sector, has an elevated zonal

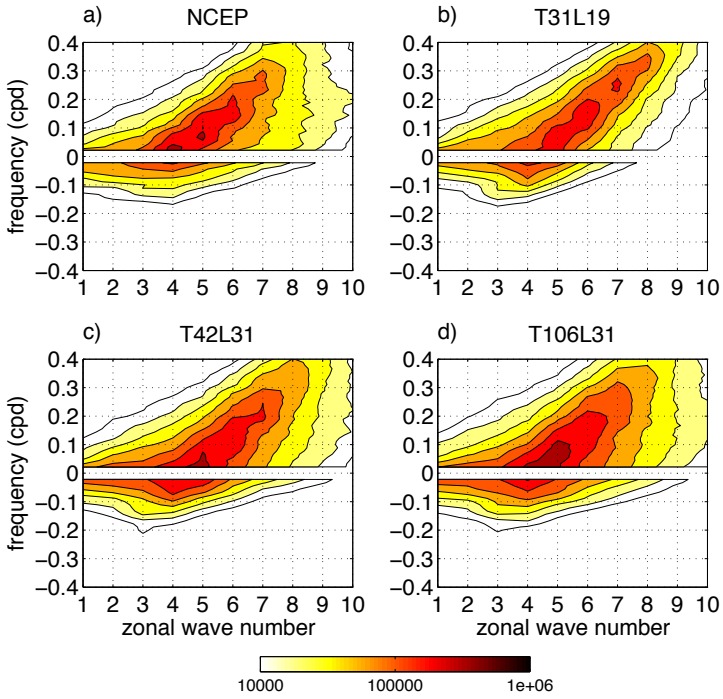

Figure 6.5: Intercomparison of kinetic energy spectra of the meridionally averaged waves in the 30S–60S latitudinal band between NCEP–DOE reanalysis (a), and AMIP simulations at the resolutions (b) T31L19, (c) T42L31 and (d) T106L31. Units and contours are as in Fig. 6.4.

symmetry and it extends over the whole hemisphere. Therefore, while in nature wave packets slow down over the Pacific sector (Chang and Yu, 1999), in the T31L19 model they can keep propagating eastward with a relatively unchanged group speed. This interpretation is consistent with what we observed in the aquaplanet, which has a zonally symmetric jet stream, and spectral power aligned over a very well defined dispersion relation.

The distribution of the PSD is much better captured at the resolutions T42L31 and T106L31, which correctly feature a minimum in the speed of the jet stream over the Pacific. We also note that the total kinetic energy increases with model resolution, which leads the T106L31 model to overestimate the total kinetic energy of extratropical atmospheric motions respect

to NCEP–DOE reanalysis.

We now focus our attention on the distribution of the PSD on the quasi–stationary components. The long wave end of the dispersion relation observed in NCEP–DOE reanalysis terminates on a k=4 wave which, as discussed in chapter 5, is quasi–stationary and marginally stable. Models fail to reproduce this feature. At the resolutions T31L19 and T42L31, the dominant quasi–stationary wave has $k = 5$, while the wave projecting on $k = 4$ is slightly westward propagating and it is less energetic than the wave five. Surprisingly, as the model resolution increases the error becomes even bigger, and at T42L31 the PSD specifically peaks on a quasi–stationary wave five. The T106L31 model performs substantially better, as the k=4 wave participates similarly to the k=5 wave to the kinetic energy budget of the low frequency part of the spectrum.

We now move on to analysing the sources of kinetic energy. Differently from what has been done in the previous chapters, the spectra will plotted using a linear scale. The difference between minima and maxima values is in fact too small to justify a logarithmic scale. Moreover, it is easier to perform qualitative comparisons between reanalyses and the model when a linear scale is employed.

In Fig. 6.6a–d we compare the spectra of the direct baroclinic energy conversion performed by the meridionally averaged waves ($P_k^\nu(\{\alpha\},\{-\omega\})$) in NCEP–DOE reanalysis and in AMIP simulations. All the models tend to overestimate the total baroclinic energy conversion which is pictured by NCEP–DOE reanalysis, even if we note an interesting progressive agreement with the reanalysis as the resolution increases. The distribution of the spectral power along a preferential dispersion relation resembles what has been observed for the kinetic energy spectra, but two features deserve further attention.

Using this diagnostic, which highlights the favourite spatial and temporal scales of baroclinic unstable processes, the dispersion relations are better defined. Dotted lines that approximately fit the distribution of spectral power

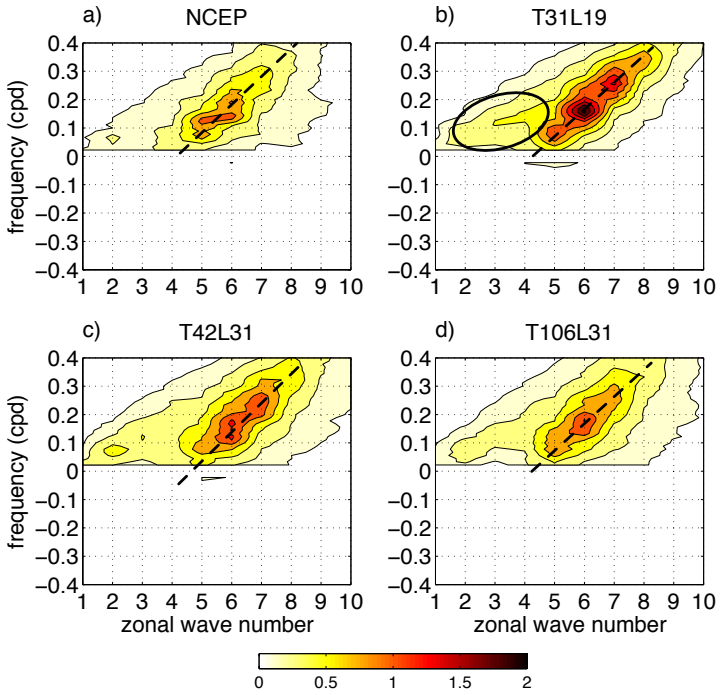

Figure 6.6: Intercomparison of the spectra of the baroclinic energy conversion by the meridionally averaged waves in the 30S–60S latitude band. A linear scale is adopted and c.i. is 0.25 W m^{-2} day. The 0.1 line is also added to the plots.

between k=5 and k=7 have been added to Fig. 6.6. This helps to visualising the wavenumber of the stationary component at the long wave end of the dispersion relation, which in NCEP–DOE reanalysis, in the T31L19 and T106L31 models roughly correspond to k=4, while at T42L31 it is more displaced toward wavenumber five. This is consistent with the bigger error in the spectral distribution of the kinetic energy found in Fig. 6.5c. But despite the linear extension of the dispersion relation would indicate a marginally stable wave four, all the models feature highest baroclinic conversion on a quasi–stationary wavenumber five. This is an unexpected behaviour and it might indicate that other processes, which are different from the purely extratropical baroclinic wave dynamics, are contributing to the maintenance of the quasi stationary wave five.

A second feature to be noted in Fig. 6.6 is the overestimation of the PSD on the spectral region indicated by an ellipse in Fig. 6.6b. This is particularly evident at the resolutions T31L19 and T42L31, and, despite being weaker, it can as well be identified at T106L31. The distribution of this anomalous spectral power reminds of the secondary dispersion relation found in the aquaplanet. Whether we can interpret this spectral power as baroclinic waves featuring a meridional scale smaller than the width of the 30S–60S latitudinal band will be later addressed in sec. 6.3.2.

In Fig. 6.7 we plot the spectra of the kinetic energy sources on the meridionally averaged wave by non linear wave–wave interactions ($< \{K\} \cdot \{K\} >_k^\nu$). In both NCEP–DOE reanalysis and AMIP simulations, the inverse kinetic energy cascade preferentially involves the low frequency waves of zonal wavenumbers four and five. Therefore, similarly to what has been found in the aquaplanet, it works to reinforce the quasi stationary components of the system. Increasing the model resolution improves the distribution of the non linear kinetic energy sources among spectral components, which is particularly very well captured at T106L31. Instead, the intensity of the inverse energy cascade increases with the resolution, and at T106L31 it is larger than the energy source found in NCEP–DOE reanalysis. This difference has not to be necessarily considered a systematic error of the ECHAM5 model. Inverse energy cascade depends on the interaction between large and small scale disturbances. Because the latter are weakly constrained by observations, and are rather determined by the dynamical evolution of the model, the intensity of the energy cascade pictured by Reanalyses might themselves be affected by the errors of the AGCM which is employed for generating the dataset. A sensitivity to the numerics and to the spatial resolution of the AGCM could be therefore expected. In fact, when inspecting ($< \{K\} \cdot \{K\} >_k^\nu$) in ERA–INTERIM reanalysis (not shown), which employs an atmospheric model of elevated horizontal resolution (T255), we see that the energy source on the quasi–stationary wave four is almost the double of what pictured by NCEP–DOE reanalysis, which has horizontal resolution T63.

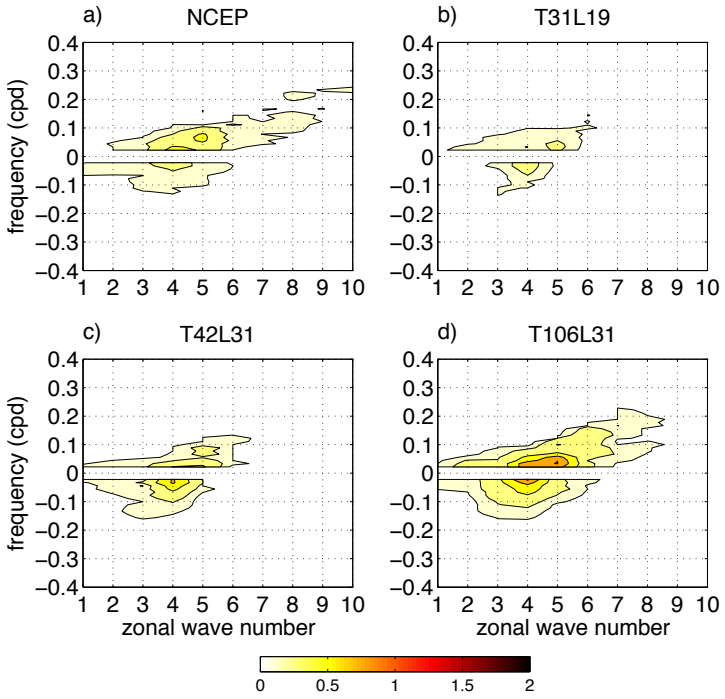

Figure 6.7: As in Fig. 6.6 but for the kinetic energy sources due to non linear interaction processes

The positive trend in the intensity of the energy cascade with increasing model resolution seems a robust property of the ECHAM5 model. A couple of explanations can be considered. As the inverse energy cascade depends on non linear interactions between triad of waves, the intensity of the cascade, assuming the efficiency of the interaction does not change, could grow with the total kinetic energy of extratropical waves. This would be consistent with the positive trend in the kinetic energy of the meridionally averaged waves with increasing model resolution that we found in Fig. 6.5b–d. Nonetheless, little differences are found in the kinetic energy of NCEP–DOE and ERA–INTERIM (not shown), so that this reasoning would not be alone sufficient for explaining the differences in the intensity of the energy cascade between the two reanalyses. This suggests another possible explanation. Models of low horizontal resolution could underestimate the non linear energy transfer because some waves, that would in reality participate to the non–linear in-

teractions, are not resolved by the model. Further analyses would be needed to verify the two interpretations, and to evaluate their relative contributions in determining the sensitivity of the energy cascade on the model resolution.

It is of interest to note that the amount of baroclinic energy conversion and of inverse energy cascade features an opposite trend with increasing model resolution, so that the energetics of the meridionally averaged waves are increasingly affected by non linear processes as resolution increases.

The sink of kinetic energy on the meridionally averaged wave by wave–mean flow barotropic interactions ($< \{K_0\} \cdot \{K\}_k^\nu >$) is not particularly meaningful and it has not been shown. Barotropic processes are in fact mainly associated to meridional angular momentum fluxes up or down gradient the angular velocity of the time mean flow (Peixoto and Oort, 1992). Angular momentum is transported by waves featuring a tilt in the horizontal plane so that decomposing this process between the meridionally averaged wave and the deviation from the meridional average has no particular meaning.

6.3.2 A secondary dispersion relation

We've noted, when discussing Fig. 6.6b–c, that the T31L19 and the T42L31 models feature moderate long wave (k=2–4) baroclinic energy conversion. As k=4 has been identified as the marginally stable baroclinic wave of the system, it is tempting to interpret these long baroclinic waves in analogy to the *secondary dispersion* relation we've found in the aquaplanet. In sec. 4.2, the secondary dispersion relation was associated to baroclinic waves whose meridional scale is smaller than the one of the waves in the main dispersion relation. The meridional decomposition introduced in sec. 6.2 is therefore useful to test this hypothesis.

Fig. 6.8 shows the baroclinic energy conversion on the waves not projecting on the meridional average. In NCEP–DOE reanalysis the spectral power is broadly distributed with little organisation along dispersion relations. As the baroclinic conversion by the meridionally averaged waves was instead organised on a well defined dispersion relation (see Fig. 6.5a), we deduce that

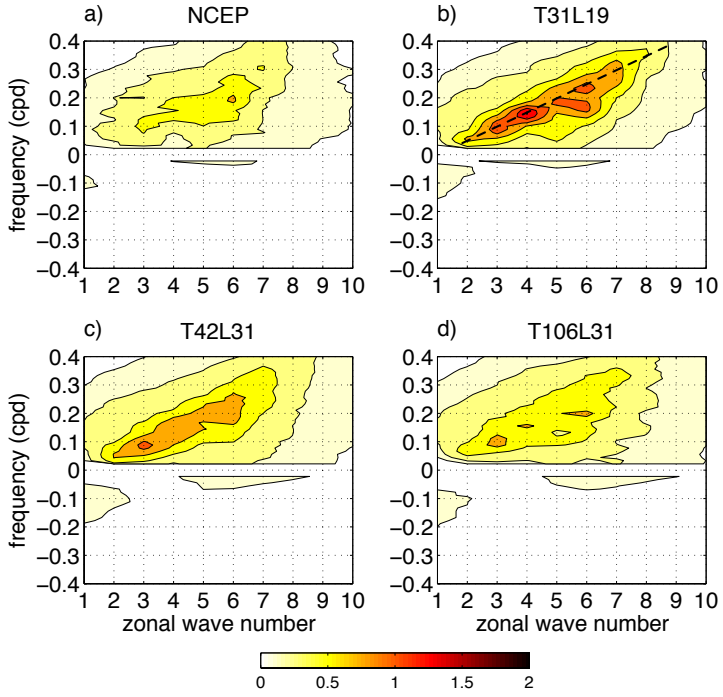

Figure 6.8: As in Fig. 6.6, but for the baroclinic energy conversion due to waves not projecting on the meridional average in the 30S–60S latitude band.

the zonally propagating baroclinic wave packets preferentially grow with a meridional scale comparable to the 30S–60S latitudinal band.

In AMIP experiments, and especially at the resolution T31L19, we instead find a well defined dispersion relation on k=2–7, which is for clarity identified by a dotted line in Fig. 6.8b. Its PSD distribution clearly involves different frequencies and wavenumbers respect to the dispersion relation characterising the meridionally averaged waves. Baroclinic wave packets featuring a meridional scale smaller than the 30S–60S latitudinal band are therefore relevant energetic structures of the T31L19 model. In analogy to the aquaplanet, we will call *main dispersion relation* the one associated to waves as large as the baroclinic band (dotted line in Fig. 6.6b), and *secondary dispersion relation* the one due to waves featuring a smaller meridional scale (dotted line in Fig. 6.8b). The secondary dispersion relation features a smaller group speed

and relatively higher phase speeds respect to the main one. The PSD that was enclosed by an ellipse in Fig. 6.5b can be now explained as the projection on the meridional average of the waves composing the secondary dispersion relation.

The amount of PSD on the secondary dispersion relation decreases with increasing model resolution. At T42L31 (see Fig. 6.8c) it is still well defined but it is also substantially weaker than at T31L19. By further increasing the resolution up to T106L31 the organisation of PSD along a dispersion relation is essentially lost and convergence toward NCEP–DOE reanalysis is found. Convergence was also found in the energy conversion on the meridionally averaged waves (see Fig. 6.6). Therefore, at least during Southern Hemisphere austral summer, there is a substantial improvement of the ECHAM5 model of representing the spatial scales and the intensity of extratropical baroclinic processes. This will better quantified in the next section.

6.3.3 Total Kinetic energy sources and sinks

In the previous sections, the baroclinic and the non linear kinetic energy sources have been separately analysed as a function of the meridional scale of the waves. Now, to get an overall picture of the energetics of the model, the total sources of kinetic energy in the baroclinic zonal band — no meridional decomposition is applied — is discussed. The total kinetic energy source is defined as the sum of the baroclinic conversion and of the non linear kinetic energy redistribution:

$$< K_{source} >_k^\nu = \int_{\varphi_S}^{\varphi_N} \int_{p_t}^{p_b} (< K \cdot K >_k^\nu + P_k^\nu(\alpha, \omega)) W_\varphi d\varphi dp \qquad (6.7)$$

Barotropic processes are in fact on average sinks rather than sources of kinetic energy (Lorenz, 1967).

A comparison of $< K_{source} >_k^\nu$ between NCEP–DOE reanalysis and AMIP experiments is plotted in Fig. 6.9a–d. In NCEP–DOE reanalysis and in the AMIP simulation performed at T106L31 the distribution of $< K_{source} >_k^\nu$ is

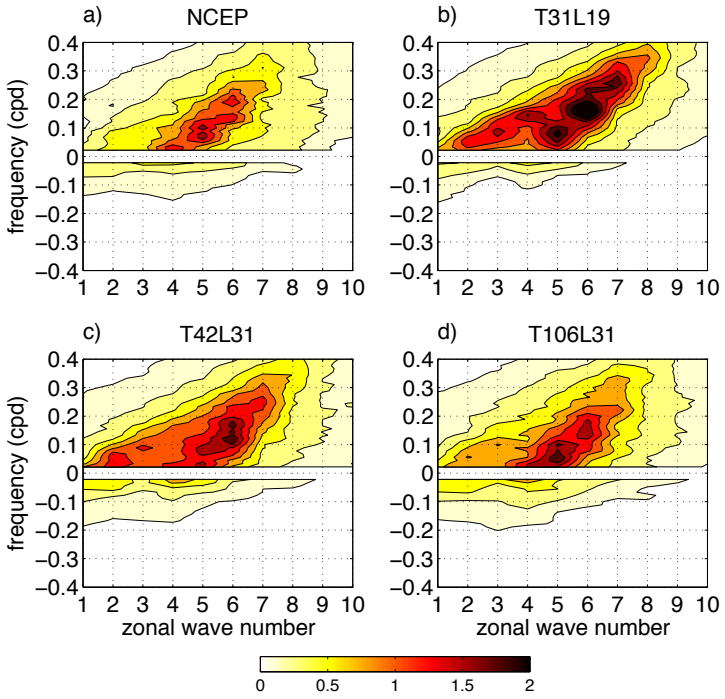

Figure 6.9: As in Fig. 6.6, but for the spectra of the total kinetic energy sources. This is defined as the sum of baroclinic energy conversion and non linear wave-wave kinetic energy redistribution.

predominantly organised along the main dispersion relation, and little evidence of a secondary branch of instability is found. The generation of kinetic energy along the secondary dispersion relation is instead a significant part of the error of the model at the resolutions T31L19 and T42L31. This is in line with the results shown in the previous sections. To better quantify the errors of the model, in Fig. 6.10b–d we plot the difference in the kinetic energy source between the performed AMIP experiments and the NCEP–DOE reanalysis. Moreover, the difference between ERA INTERIM and NCEP–DOE reanalyses is shown in Fig. 6.10a. This provides an indication of the uncertainty in our knowledge of the actual energetics of extratropical baroclinic disturbances developing in the SH austral summer. Apart for the low frequency waves four and five, the difference between the two reanalyses is clearly smaller than the error of the model. In particular, it is of interest to

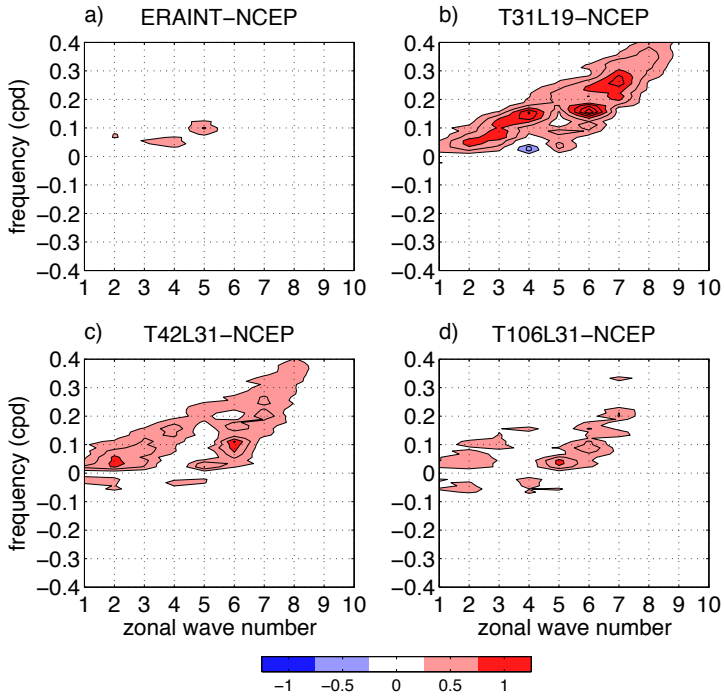

Figure 6.10: Difference, with respect to NCEP–DOE reanalysis, in the spectrum of the total kinetic energy source computed in the 30S–60S latitude of a) ERA–INTERIM reanalysis and AMIP experiments of resolutions T31L19 (b), T42L31 (c) and T106L31 (d).

note that the error of the T31L19 and T42L31 models is mainly distributed along the two previously identified dispersion relations (see Fig. 6.10b–c). The better overall performance of the high resolution model can be also seen in Fig. 6.10d, despite the kinetic energy generation, especially along the main dispersion relation, remains slightly higher than in NCEP–DOE reanalysis.

6.4 Energy balance for the low frequency waves four and five

Fig. 6.11 and Fig. 6.12 show the spectral contributions to the energetics of the k=4 and k=5 wave on the frequency domain, respectively. In par-

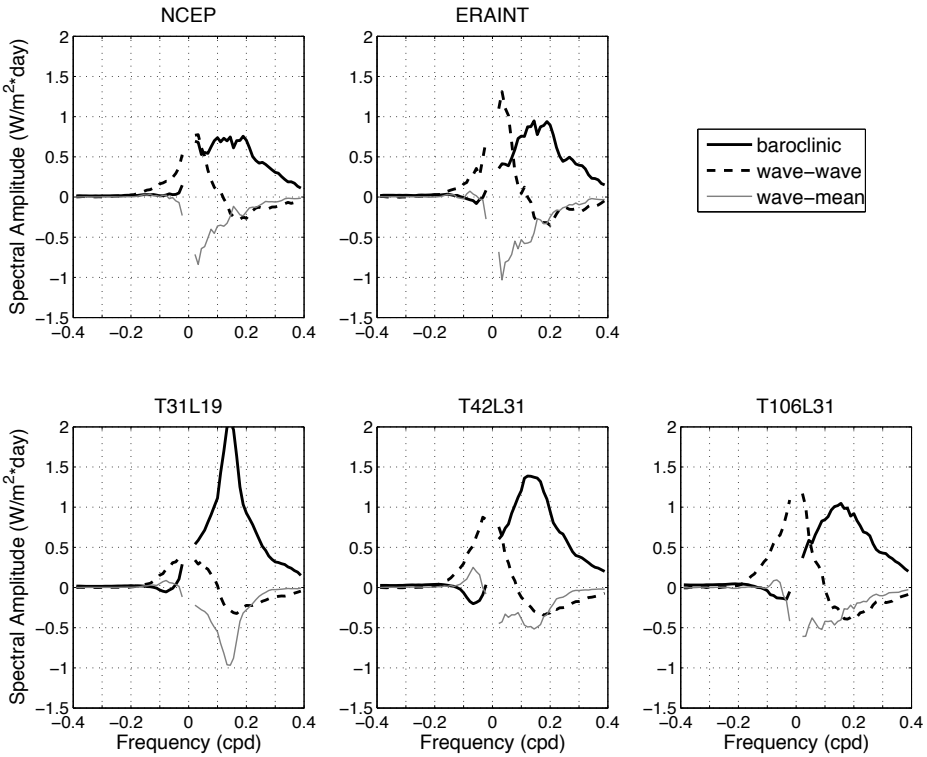

Figure 6.11: Total spectral kinetic energy sources and sinks on k=4 as a function of frequency. The analysed processes are: baroclinic direct energy conversion, non linear wave-wave interactions and barotropic wave mean flow interactions. The contributions are meridionally and vertically integrated in the 30S–60S latitudinal band and from 1000mb to 100mb.

ticular, we compare the energetics of the performed AMIP simulations with NCEP–DOE and ERA–INTERIM Reanalyses. The total contributions by baroclinic energy conversion, wave–wave interactions and barotropic wave–mean flow interaction in the 30S–60S latitude band are considered, and no meridional decomposition is applied. This approach allows to better compare the relative importance of the energy sources in the maintenance of the two waves. The choice of showing results from both Reanalyses, is related to the higher degree of uncertainty which characterises the energetics of such waves (see Fig. 6.10a).

The quasi–stationary k=4 wave in NCEP–DOE reanalysis (Fig. 6.11a) is on average equally maintained by baroclinic energy conversion and non linear wave–wave interactions. Instead, in ERA INTERIM we approximately find a doubling of the non linear transfer and an halving of the baroclinic conversion respect to NCEP–DOE. Nonetheless, as will be discussed in chapter 7, this does not preclude our interpretation of the wave four as a marginally stable baroclinic component. The higher relevance of non linear interactions in the model and in Reanalyses is a remarkable difference respect to the quasi–stationary waves observed in the aquaplanet which, for approximately zero phase velocity, are predominantly maintained by baroclinic conversion. Barotropic processes work instead to subtract kinetic energy from the wave and to increase the kinetic energy of the time mean flow.

The T31L19 model features a very strong peak in baroclinic energy conversion for $\nu \sim 0.15$ cpd, which is due to the already discussed activation of a secondary branch of instability. In this frequency range non linear interactions and barotropic processes are both working as kinetic energy sinks. Near $\nu \sim 0$ the kinetic energy sources by wave–wave interactions and by baroclinic conversion are similar, but the overall contributions are the half of what observed in NCEP–DOE reanalysis. A similar picture is also captured when considering higher resolutions, as the baroclinic conversion on the secondary dispersion relation remains the dominant feature of the energetics on k=4. Nonetheless, as resolution increases, the relative importance of non linear processes and baroclinic conversion near stationarity substantially changes. The contribution by non linear energy transfer grows and it largely overtakes the contribution of baroclinic conversion, which instead decreases with resolution. As a result, the energetics of the T106L31 model near $\nu \sim 0$ are much more similar to ERA–INTERIM than to NCEP–DOE reanalysis. Moreover, the dynamics of the quasi–stationary activity on $k = 4$ gets more and more dominated by non linear processes.

We now move the attention to the energetics of the waves projecting on k=5, which is shown in Fig. 6.12. In both the Reanalyses we find a maximum

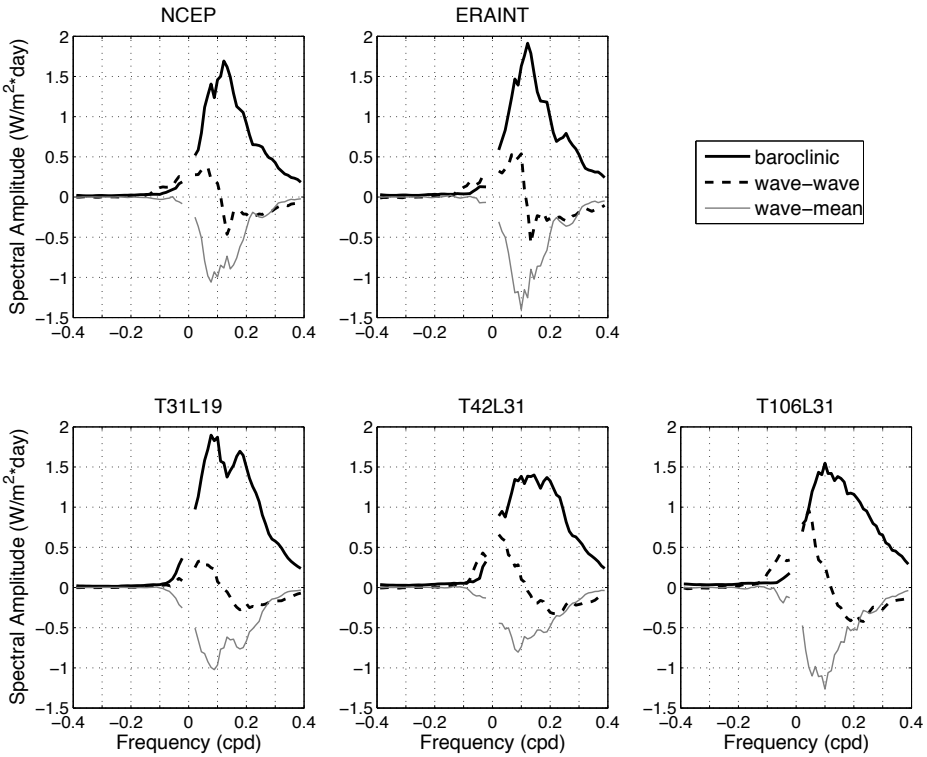

Figure 6.12: As in Fig. 6.11 but for the balance on k=5.

in baroclinic energy conversion at about $\nu \sim 0.1$ cpd, which is in large part compensated by an energy sink due to barotropic processes. This confirms that the k=5 wave is on average a properly unstable component. Non linear processes play instead a minor role. When considering the energetics of the k=5 wave in the AMIP simulation at T31L19 (Fig. 6.12b), a broad peak split into two relative maxima — one is located near $\nu \sim 0.1$ and one near $\nu \sim 0.2$ — is observed. The latter maximum is the result of instabilities along the secondary dispersion relation. As we increase the resolution of the model, the peak in baroclinic conversion on $\nu \sim 0.2$ cpd becomes progressively weaker so that the distribution get closer to reanalyses. High frequency ($\nu > 0.15$) baroclinic conversion is nonetheless overestimated by the model independently from its resolution.

When considering the distribution of power near $\nu \sim 0$, it is interesting

to note that the T31L19 and the T42L31 models feature an higher baroclinic conversion than what is found in both the Reanalyses. We can't simply interpret this difference saying that k=5 is the marginally stable component of the system instead of k=4, because, while in reanalyses the stationary wave four is located at the long wave end of the dispersion relation, the wave five in the models is not. In particular, we've seen the wave five is properly unstable and features maximum baroclinic energy conversion on a period roughly corresponding to 10–15 days. We conclude that the wave four is the marginally stable component in both reanalyses and models, but, for some reasons that can't be directly explained using the theory developed in the aquaplanet, models feature relevant quasi stationary activity on the wave five. The only exception to this reasoning applies at resolution T42L31. In particular, the whole baroclinic dispersion relation is displaced on more negative frequencies, so that considering the wave five quasi–stationary and marginally stable seems to be more appropriate.

Some hypothesis can be made for explaining the model errors in representing the Southern Hemisphere quasi–stationary waves. In the models, the wave four could be too stable, or the waveguides necessary for limiting the meridional dispersion of the wave missing so that the necessary conditions for the growth of the wave four are not satisfied. For what concerns the stationary activity on k=5, one possibility is that interannual variability in the seasonal mean state leads to a weaker average baroclinicity, so that the wave five becomes occasionally stationary and marginally stable. This would be consistent with the slower decrease in baroclinic conversion for decreasing ν found in models respect to reanalyses. Another possibility is that other mechanisms participate to the maintenance of the quasi–stationary wave five. Fig. 6.12b–d suggest that non linear processes, especially at T106, are important in reinforcing and in slowing down the propagation of the wave five. As a last hypothesis, the wave five could be mainly sustained by tropical convection, with direct baroclinic conversion and wave–wave interactions providing a positive feedback. A combination of the three suggested explanations —

i.e. interannual variability, non linear forcing, tropical convection — could as well be working. Analysing the spatial structure of the patterns gives some clues to identify what processes might be effectively occurring.

6.5 Spatial distribution of quasi–stationary wave activity

We now perform an EOF analysis which aims to identify the horizontal structure of the dominant quasi–stationary waves. This allow to get better insight into the spatial distribution of the error. The EOF analysis is applied to the 30 days low pass filtered meridional velocity at 200mb using the same approach adopted in chapter five for identifying the structure of the k=4 wave in NCEP–DOE reanalysis — see section 5.2.2 for a detailed description. Data from all the ensembles are taken in consideration in the EOF computation, and the results, which are presented in the form of homogenous correlation maps, are shown in Fig. 6.13. The EOF patterns obtained from NCEP–DOE reanalysis, which have already been discussed in chapter 5, are as well reported in the figure to ease the comparison. After a first inspection of Fig. 6.13, we find that in low resolution models the dominant modes of low frequency variability project on the zonal wave number five, while at the resolution T106L31 the model correctly captures the zonal scale of the pattern. Apart from these basilar informations, which are consistent with the previous spectral analysis of the energetics of extratropical waves, other useful considerations can be raised by inspecting Fig. 6.13.

At T31L19 the pattern is equatorward displaced of some degrees respect to what is found in NCEP–DOE reanalysis. This is consistent with the bias in the latitude of the main jet stream, which has been evidenced in table 6.1. The patterns are notably stronger over the Pacific sector, where the first two EOFs are approximately in spatial quadrature and exhibit an arching structure from Australia toward South America. EOF1 has a smaller amplitude over the Atlantic and the Indian ocean sectors than EOF2. This

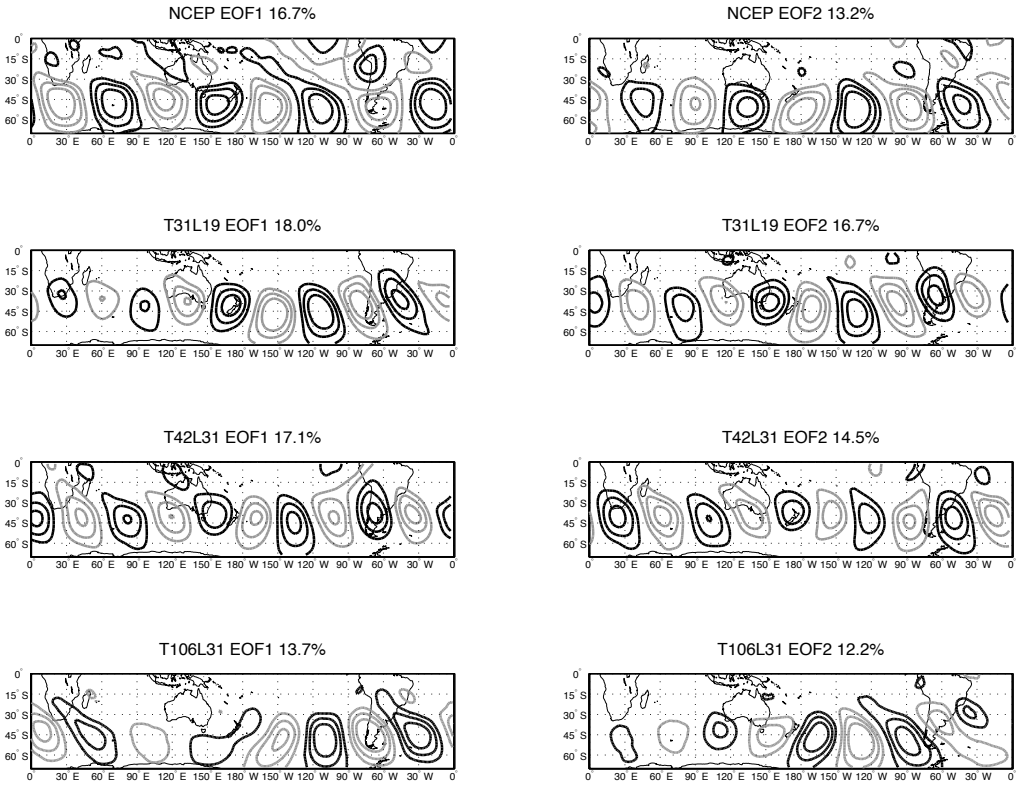

Figure 6.13: Spatial structure of DJF quasi–stationary wave activity in NCEP–DOE reanalysis, and in the set of performed AMIP experiments, as revealed by the first two EOF patterns of the time filtered meridional velocity at 200mb. EOFs are computed and plotted using the same method adopted in Fig. 5.2.

suggests that the longitudinal phase of the pattern associated to EOF2 leads to a more efficient circumglobal recirculation of energy.

The EOFs computed at T42L31 differ in some aspects from those found at T31L19. For instance, their amplitude is notably higher over the Indian ocean sector, and they are more uniformly distributed around the hemisphere than what is found at T31L19. An arching structure is still present but, while in EOF1 it is again located over the Pacific sector, in EOF2 it is eastward displaced of about 90 degrees, so that the turning point of the wave in EOF2 is found over South America instead than over the central Pacific. This breaks

the spatial quadrature between the two EOFs over the Pacific sector, and the two EOF patterns do not compose the orthonormal phases of a propagating wave.

The first two EOFs computed at T106L31 mainly project on k=4 but the patterns, instead of being confined to the extratropics and being equally distributed over the hemisphere, are essentially only composed of the Pacific arching wave ranging from Australia to South America. The trajectory is similar to what is found at T31L19, but the pattern is much more confined to the Pacific sector and little signature of circumglobal propagation is observed. Therefore, also the quasi–stationary waves generated by the model at T106L31 do not share the morphology of the k=4 wave slowly propagating in reanalyses.

When computing the lagged correlation between the first and the second PCs, we find very small values which are not statistically significant different from zero at the %5 level in any experiment. This implies that coherent modes of very slowly eastward propagation are not generated in the AMIP simulations.

A common feature which is shared by the three configurations of the model, is the projection of the first EOF on an arching wave over the Pacific ocean. This is a main difference respect to what is found in NCEP–DOE reanalysis, where such a wave is absent. The arching trajectory over the Pacific resembles the Pacific South American (PSA) pattern (Ghil and Mo, 1991; Lau et al., 1994; Kidson, 1999) with the exception that is has zonal wavenumber 4–5 instead of 3. The PSA is a well known low frequency dynamical mode contributing to the intraseasonal and interannual variability of the Southern Hemisphere during all the seasons with the exception of summer. It is therefore not surprising that we do not find such a pattern in reanalyses. The cross correlation function between PC1 and PC2, which is not significantly different from zero, is consistent with the interpretation of the PSA in terms of weather regimes given by Robertson and Mechoso (2003). According to this study, the atmosphere oscillates between the different phases of

the PSA pattern, without that the transitions lead to a coherent eastward propagation of the wave.

The dynamics of the PSA is still not very well understood, but it is mainly considered an internal mode of variability of the extratropical atmosphere (Lau et al., 1994; Robertson and Mechoso, 2003). Nonetheless, persistent PSA modes seem to be favoured by anomalous tropical convective activity due to El Nino and to the Madden Julian Oscillation (MJO) on the interannual and intraseasonal timescales, respectively (Karoly, 1989; Mo and Higgins, 1998; Mo, 2000). To investigate whether tropical convection might trigger or sustain the wave, we've computed, at each grid point, the lead–lag temporal correlations between the PCs and the OLR at that grid point. The OLR has been preprocessed by removing the harmonic components of period 12 and 6 months, so that the seasonal cycle is filtered. Moreover it has 30 days low pass filtered to keep the same temporal scales in the two signals. We do not find significant statistical correlations at the 5% level with OLR anomalies in the tropical region at any resolution. Only at T31L19, by examining lead–lag correlations, we found the patterns of the PCs are effectively emitted from the Australian region, so that convective bursts over the maritime continent and the western Pacific Ocean could be important for triggering the wave. These results confirm that the quasi–stationary patterns simulated by the model are mostly maintained by extratropical atmospheric dynamics.

The degree of zonal symmetries of the simulated PSA–like pattern is strongly affected by the resolution of the model. At T31 and T42 the pattern is part of a circumglobal signal, which suggests that the recirculation of energy in baroclinc wave packets might contribute in sustaining the mode. At T106 the signal is instead almost absent in the Indian Ocean sector, so that the relevance of the recirculation of energy seems less central. To discuss this hypothesis, we plot in Fig. 6.14 the Howmöller diagrams of the meridional velocity at 200mb meridionally averaged over the 30S–60S latitudinal band during the 92–93 austral summer. Data are taken from the three en-

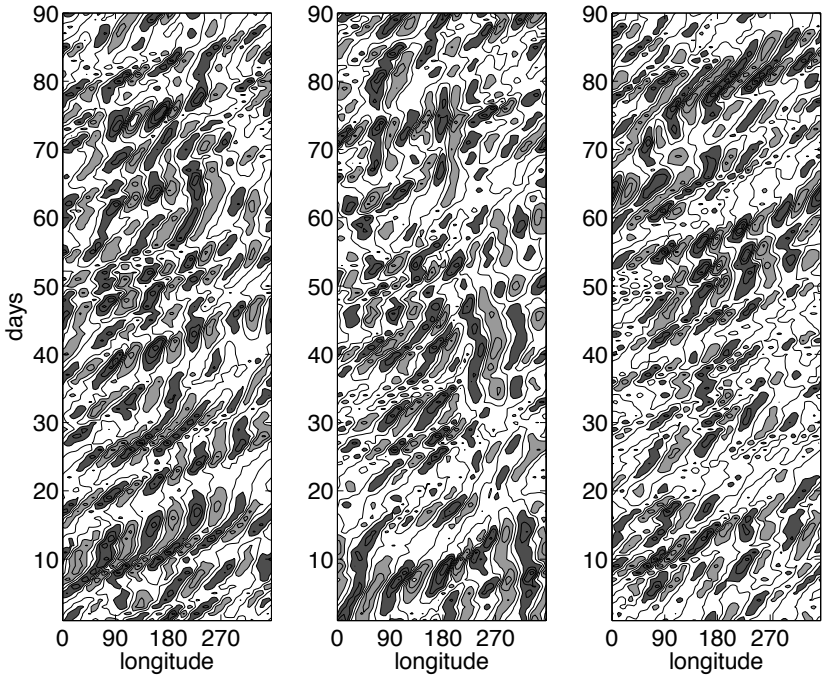

Figure 6.14: Comparison of Howmöller diagrams of v at 200mb meridionally averaged in the 30S–60S latitudinal band during the 92–93 austral summer. Data are taken from the three elements of the ensemble realised at the resolution T31L19.

sembles realised at the resolution T31L19. We've selected this year because, as can be seen in the first and, to a minor extent, in the third ensemble, we observe a remarkable stationary activity on $k = 5$ which is sustained by coherent circumglobal recirculation of wave packets. In the second ensemble stationary activity is instead weaker and it features a different longitudinal phase. The dependance of the intensity and of the phase of the pattern on the particular ensemble suggests that the stationary activity is unlikely the result of a stationary Rossby wave forced by some fixed convective patterns. On the contrary, consistently with the interpretation of the PSA given by (Mo and Higgins, 1998), tropical convection could catalyse the organisation of extratropical wave packets, so that a preferential longitudinal phase is maintained in the extratropical quasi–stationary activity.

The propagation of coherent quasi–stationary wave packets, as those pictured in Fig. 6.14, decreases with increasing model resolution, and they are hardly observed at T106L31. This is consistent with the EOFs being confined to the Pacific sector and with the smaller variance they explain respect to lower resolution models. It is speculated that the coherence of quasi–stationary extratropical motions is affected by the ratio of the energy supply by baroclinic conversion and by non linear energy transfer. As shown in Fig. 6.11d, stationary wave four activity at T106L31 is essentially maintained by non linear processes. While a baroclinic energy source is necessarily generating kinetic energy in phase with the wave itself, kinetic energy resulting from non linear interactions depends on the organisation of high frequency transients by the low frequency wave (Kug et al., 2010). This can be less tight to the wave structure, so that the coherence of the wave packet is more easily lost. Further research would be needed to better understand the relation between tropical convection, recirculating wave packets and the formation of stationary patterns.

6.6 Relations with the mean state

In this section we suggest possible connections between the errors in the mean state, in the energetics and in the spatial structure of the dominant quasi–stationary modes of variability, that we've shown to be affecting the model.

Looking at the Rossby stationary wavenumber (K_s) provides guidance in interpreting how errors in the mean state might affect the errors in the spatial scale of the quasi–stationary waves. The meridional distribution of K_s, which is computed on the zonal mean flow at 300mb, is presented in Fig. 6.15. K_s decreases with increasing latitude but it features a plateau with approximately constant values in correspondence of the jet stream between 35S and 50S. In this latitudinal band, which is crucial in determining the scale of the stationary patterns, K_s is between four and five in NCEP–DOE

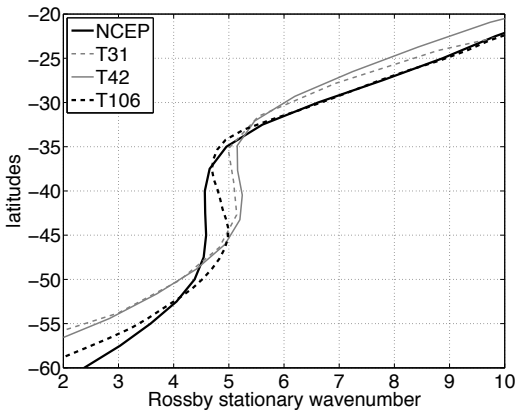

Figure 6.15: Meridional distribution of the Stationary Rossby wavenumber computed on the DJF climatological zonal mean flow in the Southern Hemisphere. Results from NCEP–DOE reanalysis and the performed AMIP simulations are compared.

reanalysis, while it is just above five in AMIP experiments at T31L19 and T42L31. At the latter resolution the model performs even slightly worse in this diagnostic. Some marked improvements are instead found at the resolution T106L31, despite a local maximum where $K_s \sim 5$ is still present near 45S. The errors in the zonal mean state are therefore consistent with the dominant quasi–stationary waves projecting on k=5 instead of k=4 in the low resolution models.

In Table 6.1 we showed that increasing the model resolution leads to a weaker but wider seasonal mean jet stream. These changes tend to compensate each other in the computation of K_s, which, as we've seen in Eq. 1.1, scales as $\beta/U+1/L^2$. The same considerations apply for the marginally stable wavenumber of a baroclinic theory, as Green's, if the meridional gradient of the absolute vorticity ($\beta - U_{yy}$) is considered in place of β. The intensity of the simulated jet stream always exceeds what is found in NCEP–DOE reanalysis, so that K_s is lowered by the bias in U. We therefore attribute to the too narrow meridional scale of the jet some faults in the misrepresentation of the spatial scale of the stationary waves. Another source of error

for the quasi–stationary wavenumber can result because of the bias in the latitude of the jet, which in the model is shifted toward the equator. For solely geometrical reasons, as the latitude decreases, the zonal Earth circumference increases, so that a same zonal wavelength progressively project on an higher zonal wavenumber on the sphere. Moreover, the dynamical influence of Earth rotation on atmospheric waves change with latitude. In particular, a strengthening of the β effect and a weakening of vorticity generation by stretching of atmospheric columns is found as latitude decreases. According to Green's model, such changes increase the marginally stable wavenumber of the system (see Eq. 1.4).

In Fig. 6.16 we further extend the analysis of the refractive properties of the time mean flow by comparing the horizontal distribution of K_s at 300mb. When considering the Atlantic and the Indian ocean sectors, the waveguide for a stationary wave four, which has been identified in NCEP–DOE reanalysis in the previous chapter, is substituted by a waveguide for a zonal wavenumber five in the AMIP experiments at the resolutions T31L19 and T42L31. The distribution of K_s in this region is instead reasonably well captured by the T106L31 model, which, as we discussed in section 6.3, is also better representing the energetics of extratropical baroclinic waves. This is not a coincidence. The waveguide is created by the local enhancement of the β effect due to the meridional curvature of the extratropical eddy–driven jet stream, which is predominantly maintained by the meridional heat transport and by the convergence of zonal momentum in growing baroclinic waves. The net effect of these processes is summarised in the barotropic wave–mean flow interaction term of the Lorenz energy cycle. Inspecting Fig. 6.11 and Fig. 6.12 we observed that, among the examined processes, the barotropic wave–mean flow energy transfer is the one which is better converging toward reanalyses as resolution increases. On the contrary, low resolution models feature a too vigorous Lorenz energy cycle, so that the excess in the barotropic conversion leads to the formation of a too strong and a too narrow extratropical jet, which in turn negatively affects the scale of quasi–stationary patterns.

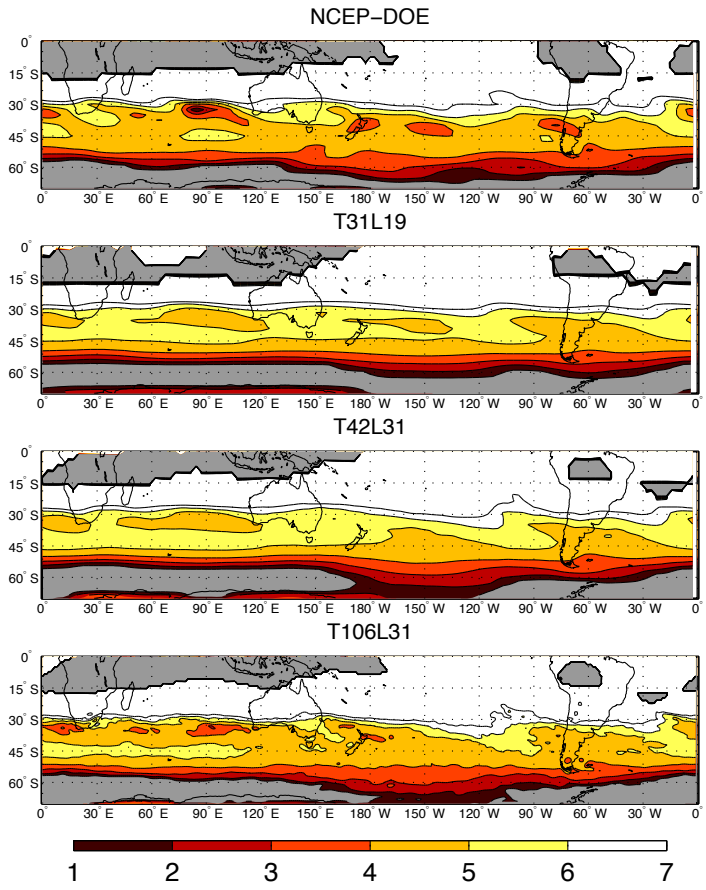

Figure 6.16: Horizontal distribution of the Rossby stationary wave number computed from the DJF climatological 300mb level flow in (a) NCEP–DOE reanalysis, and in AMIP simulations at the resolution (b) T31L19, (c) T42L31, (d) T106L31. Contour interval is one, and the stationary wavenumbers from 1 to 7 are represented. Grey shading refers to negative values of K_s^2

The considerations presented in discussing the distribution of K_s over the Atlantic–Indian sector do not hold over the Pacific, where in some areas relevant errors are found also at T106L31. In particular, K_s remains systematically higher than in reanalyses near New Zealand, as models fail to simulate the subtropical jet stream, and to the west of the South American continent. The latter region is particularly interesting, as very little changes

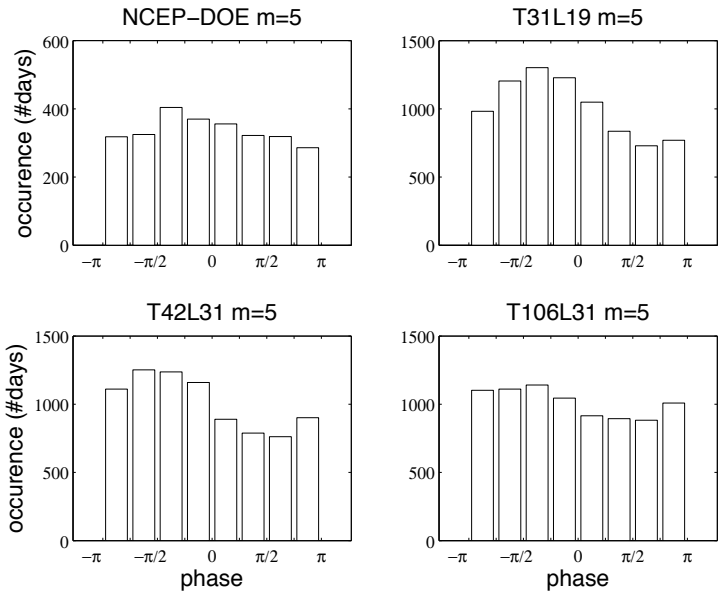

Figure 6.17: Distribution of the longitudinal phase of the zonal wave five in the daily v at 200mb meridionally averaged in the 30S–60S latitudinal band for a) NCEP–DOE reanalysis, and AMIP experiments at the resolutions b) T31L19, c) T42L31 and d) T106L31. The counting in figures b–d is higher because data from three ensembles, for each resolution, are considered.

occur with increasing the model resolution, and K_s remains systematically higher than in reanalyses. This error in the east–pacific is consistent with a leakage of extratropical waves from the baroclinic band toward the tropics over South America. As this is a typical feature of the PSA–like mode that dominates quasi–stationary activity in the models, it should be further investigated whether the error in the mean state might be a reason leading to the development of the PSA–like mode.

We have thoroughly discussed the anomalous power on an extratropical quasi–stationary wave five that AMIP experiments feature respect to Reanalyses. We now examine whether this error can be related to errors in the stationary waves of time mean flow. In Fig. 6.17a–d we plot the histogram of the phase of the zonal Fourier component with $k = 5$ computed on the meri-

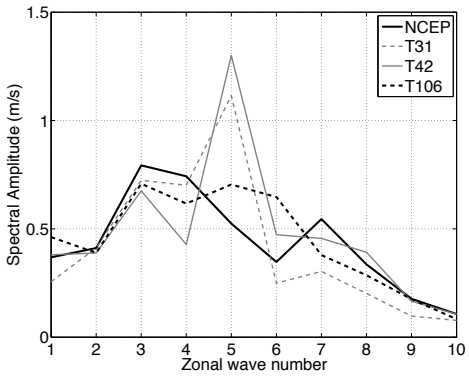

Figure 6.18: Zonal Fourier amplitudes of the climatological (DJF) stationary waves in v at 200mb. Data have been previously meridionally averaged in the 30S–60S latitudinal band. Results from NCEP–DOE reanalysis and the ensemble means of the performed AMIP experiments are compared.

dional velocity at 200mb meridionally averaged in the 30S–60S latitude band. In both NCEP–DOE reanalysis and AMIP experiments we can reject the hypothesis that the distribution is flat at the 5% confidence level. Nonetheless, the distributions in the T31 and in the T42 models exhibit a marked unimodal character, where the phases in the interval $[-\pi, 0]$ occurs about 30% more frequently than the phases in the interval $[0, \pi]$. This asymmetry could create a signal which persists in the mean state of the models. To verify this hypothesis, we show in Fig. 6.18 the amplitude of the zonal Fourier component $k = 5$ computed on the DJF time mean state of v at 200mb. As usual, a meridional average in the 30S–60S zonal band is previously applied to the data. A spike on the zonal wavenumber five characterises the error of the T31 and T42 models. Stationary wave amplitude on the zonal wavenumber four is instead underestimated by the T42 model. The distribution of the error on k is therefore consistent with the bias in the energetics of the waves we have identified in these models. This suggests that the recirculating wave packets, whose envelope projects on k=5, tend to form on some preferential phases in the low resolution models. Nonetheless, in both models and

Reanalyses, we find that no substantial vertical heat transport on k=5 sustain the extratropical stationary waves. This increases the confidence that the bias in the stationary wave pattern relies on an energy source which is external to extratropical dynamics and possibly features a preferential longitudinal phase. For instance, tropical convection could be feeding vorticity in a Rossby wave which, because of the errors in K_s, project on the zonal wavenumber five. The experiments suggested in the next chapter might help to get a better understanding of these processes.

Chapter 7

Conclusions

This thesis has been devoted to studying the statistical properties and a mechanism of formation of quasi–stationary waves in the extratropical atmosphere. Rossby theory, which describes the kinematics of neutral waves, is commonly adopted for interpreting these patterns. From an energetic perspective, Rossby waves require an external forcing — as the feeding of vorticity by tropical convection or the inverse energy cascade of barotropic kinetic energy — to be maintained against dissipation. By analysing the quasi–stationary waves forming in an aquaplanet model, we've been able to highlight the values and the limitations of the Rossby wave theory, which is in particular unsatisfying for describing the energetics of such waves. These limitations have been overcome by introducing a new paradigm that describes quasi–stationary waves as marginally stable baroclinic components. We've found that this new paradigm, which is of intrinsic interest also from a purely geophysical fluid dynamic perspective, also applies for the study of patterns in the Earth's climate and it provides some guidance for analysing the systematic errors of climate models.

In the simulations we have performed with an aquaplanet set up of the ECHAM5 model, using boundary conditions analogous to those in the Aquaplanet Intercomparison Project, a quasi–stationary wave, projecting on the zonal wavenumber five, peaks in the subtropics and features an impressive

temporal coherence. The kinematics of the wave is consistent with the picture of a nearly equivalent barotropic Rossby wave which is trapped in the upper tropospheric wave guide maintained by the jet stream at about 30° of latitude. Nonetheless, the wave features a weak, but well defined, baroclinic vertical structure, and it consistently converts potential into kinetic energy through direct baroclinic processes. The quantitative computation of the spectral sources of kinetic energy shows that non–linear interactions provide an amount of kinetic energy to the quasi–stationary wave five that is about one forth of the kinetic energy converted by baroclinic processes. Differently from the previously proposed barotropic mechanisms (Watanabe, 2005), we conclude that the wave five is an active baroclinic wave, and that the turbulent inverse energy cascade only works as a further positive feedback on the wave energy.

The Hayashi spectral analysis of the energetics of extratropical waves proved to be a powerful technique for identifying the stability of atmospheric waves and their organisation along preferential dispersion relations. Using this technique, the wave five appears as a spectral peak of nearly zero frequency belonging to a well defined dispersion relation, with eastward group velocity, on the zonal wave numbers $k = 3$–7. Moreover, the wave five is the longest component on the dispersion relation which is converting available potential energy into kinetic energy through baroclinic processes. The distribution of the spectral power is reminiscent of the dispersion relation of the normal modes of linear baroclinic models as Green's. By including the β effect, the Green's model contain the dynamics of both Rossby waves and baroclinic unstable waves, and the transition between the two regimes occurs at a marginally stable wave that has the phase speed of the zonal wind at the surface. Quasi–stationarity and marginal stability are two properties that can therefore coexist in the same wave. The average baroclinicity of the system, which can be controlled by modifying the equator to pole SST difference (Δ_T), determines the spatial scale of the marginally stable wave. Consistently with Green's model, decreasing Δ_T makes the wave five

progressively stable and westward propagating, and new quasi–stationary patterns on the wavenumbers six and seven, which are still baroclinic in the energetics, are found for $\Delta_T = 15$ and $\Delta_T = 11$, respectively. This proofs that quasi–stationary waves in the aquaplanet can be interpreted as marginally stable baroclinic waves, which kinematically behave as equivalent barotropic Rossby waves, but are energetically sustained by direct baroclinic energy conversion. As far as we know, it is the first time that the transition between long Rossby waves, and short unstable baroclinic waves, passing through the quasi–stationary marginally stable component, has been identified in a non linear AGCM.

Extratropical baroclinicity can be also changed by solely modifying tropical SST. In particular, increasing tropical SST leads to a stronger hydrological cycle which, by an increased latent heat release, warms the mid–tropospheric tropical atmosphere and stimulates an enhanced meridional heat transport in the Hadley cell overturning. This ultimately warms the subtropics and forces an increased extratropical baroclinicity. The intensity of the simulated tropical hydrological cycle can be itself dependent on the specific parameterisation of convection employed in the model. To analyse this sensitivity, the aquaplanet experiments have been also repeated using the Tiedtke (1989) convective scheme, which closes the parameterisation on large scale low level moisture convergence instead that on Convective Available Potential Energy (CAPE) (Nordeng, 1994). The dependance of the amplitude of the quasi–stationary wave on Δ_T is similar to what is shown in Fig. 4.6, but the maxima occur at values of Δ_T which are lower of about 2–4 degrees. Therefore, when low resolution aquaplanet models are considered, the Tiedtke (1989) scheme forces a slightly higher extratropical baroclinicity. It would be of interest to further compare the two schemes to determine whether a convergence in the average extratropical baroclinicity is found for increasing model resolution.

Using a space–time instead than a spectral approach, the quasi–stationary wave five belongs to an eastward propagating wave packet, which can coher-

ently recirculate around the globe, in such a way that the phase of the k=5 component remains essentially stationary. This is consistent with the dispersion relation observed in Hayashi spectra. The wave packet coherence is maintained by the upper tropospheric wave guide, and it is probably positively affected by the proximity of the wave guide to the subtropics. In idealised experiments, Chang and Yu (1999) found that the meridional advection of zonal momentum in the Hadley cell works to restore the potential vorticity gradient in the jet stream, which would be otherwise smoothed by the mixing of air due to extratropical wave motions. The proximity of the wave guide to the tropics also allows for a vigorous interaction between tropical and extratropical dynamics, and a wave five pattern in the tropical convection is found to be phase–locked with the extratropical wave. To investigate the nature of the interaction, we've setup an experiment in which the forcing of extratropical waves by the tropical convection is suppressed. This *symmetrised convection experiment* has demonstrated that the extratropical wave organises the tropical convection on k=5, which in turns provides a positive feedback on the extratropical wave itself. Therefore, the classical Rossby paradigm, in which tropical convection is forcing extratropical patterns, is here substituted by a tropical–extratropical resonance.

We conclude that two conditions are necessary for the development of coherent and strong quasi–stationary wave patterns: the existence of an upper tropospheric wave guide, which allows the recirculation of energy in baroclinic wave packets, and a marginally stable baroclinic component, which feeds kinetic energy into a quasi–stationary wave.

We then moved to applying the theoretical framework developed in the aquaplanet to the study of quasi–stationary patterns forming in the Earth's climate. Because a relatively high degree of zonal symmetry is probably necessary for satisfying the above stated conditions, we decided to focus on the Southern Hemisphere austral summer. The examination of NCEP–DOE reanalysis, over the 1979–2009 period, reveals that the spectral power of the upper tropospheric waves propagating in the extratropical baroclinic band

is organised along a clear dispersion relation, that has statistical properties analogous to what is found in the aquaplanet. The only difference is that it ends on a quasi–stationary wavenumber four instead of five, which implies the SH has an higher average baroclinicity than the aquaplanet. We believe that this is not a consequence of a different zonal average SST, which is in fact relatively similar, but of the warm pool in the west Pacific, where SST are locally higher than in the aquaplanet. A dispersion relation ending on the quasi–stationary wave five is in fact recovered in aquaplanet experiments forced by the observed DJF zonal mean SST. Therefore, the average extratropical baroclinicity, is controlled by the highest, rather than the average, tropical SST. This is not surprising when considering that tropical convection, which controls the tropical thermal structure and therefore the Hadley cell overturning, is itself mostly occurring over the warmest tropical waters. SST changes over cold surface waters, where little convection on average occurs, are therefore less prone to influence extratropical atmospheric dynamics.

The formation of a coherent and intense quasi–stationary wave four is episodic and it only develops during some austral summer seasons. According to the paradigm of the marginally stable quasi–stationary baroclinic wave, this can be related to the wave four being to stable for the average Southern Hemisphere conditions. Big uncertainties are found in the energetics of the wave four as pictured from different reanalyses. In NCEP–DOE reanalysis we find a similar contribution by baroclinic conversion and non linear energy transfer, while in ERA–INTERIM reanalysis the baroclinic conversion is less than the half of what is provided by non linearities. Despite this difference in the average energetics, both reanalyses indicate a remarkable increase in the quasi–stationary k=4 baroclinic conversion in the course of the seasons featuring the growth of the wave four. Non linear energy transfer remains instead roughly unchanged. This is therefore consistent with the picture of the destabilisation of a marginally stable baroclinic component.

Statistically significant correlations are found between the OLR pattern

that is typical of ENSO and the change in the wave four power in the course of the season, with El Nino being associated to a stronger wave four. In particular, an extremely intense and very coherent slowly eastward propagating wave four develops during the 97–98 austral summer, which corresponds to the strongest El Nino event on record. Because of the rather small number of episodes, the connection between ENSO and the formation of a slowly propagating wave four in the Southern Hemisphere can't be considered fully demonstrated by the results shown in the thesis. Nonetheless, an interaction between the tropical thermal forcing due to El Nino and the extratropical formation of the wave four, is entirely consistent with the baroclinic framework we are proposing for interpreting quasi–stationary features. During El Nino years, the anomalously warm tropical equatorial SST leads to an increased tropical latent heat release, which warms the mid–tropospheric atmosphere up to subtropical latitudes. This thermal change increases the extratropical baroclinicity, so that, similarly to what is found in the aquaplanet, the almost stable baroclinic wave four could be destabilised.

The final aim of thesis was to analyse the error of climate models with respect to the formation of quasi–stationary patterns, so that we tested the ability of the ECHAM5 model, setup in AMIP configuration, to reproduce the quasi–stationary baroclinic wave four we identified in the Southern Hemisphere austral summer. We find that at the three tested resolutions — namely T31L19, T42L31 and T106L31 — the model gives an unsatisfying simulation of the quasi–stationary wave four. In particular, the quasi–stationary waves simulated by the model differ from the wave four found in Reanalyses in three features: the zonal wavenumber, the slowly eastward propagating character and the extratropical confinement. We will now give a better discussion of these errors.

At low and medium resolution (i.e. T31L19 and T42L31) we find that quasi–stationary activity projects on the zonal wavenumber five instead of four. In this regard, a remarkable improvement is found at resolution T106L31, which approximately captures the right zonal scale of the pattern. We reckon

that these improvements can be linked, using Rossby theory, to a better simulation of the atmospheric extratropical mean state. At low resolution, the extratropical jet stream is found to be too narrow, too barotropic and too equatorward displaced, but as the model resolution increases, these basilar statistical properties of the extratropical atmosphere get closer to Reanalyses values. All these features affect the Rossby stationary wavenumber, which we've shown to provide guidance in identifying wave guides and the spatial scale of the stationary atmospheric patterns.

We find that the systematic errors of the time mean jet stream can be linked to errors in the energetics of extratropical baroclinic waves. In particular, consistently with the jet stream being too barotropic, we find that low resolution models feature a too vigorous Lorenz's energy cycle. An intriguing and unexpected result is that the extra baroclinic conversion is about equally distributed along two spectral regions that we named the *main* and the *secondary* dispersion relations. The former is composed of waves as large as the baroclinic band, and the latter features waves of smaller meridional scale. Because in Reanalyses the baroclinic activity predominantly develops along the main dispersion relation, the relative error along the secondary dispersion relation is particularly elevated. It is not clear what leads to the activation of this secondary branch of instability, and it would be of interest to understand whether it is also affecting other models or whether it is specifically forming in the low resolution configurations of ECHAM5. Extending the analysis to other AGCMs could help answering these questions. Anyway, if it were possible to stabilise the secondary branch of instability, improvements in the model systematic error could be expected. Boer and Lambert (2008), by comparing AMIP simulations performed with different AGCMs, found that a stronger eddy kinetic energy dissipation is on average associated to a stronger baroclinic energy conversion. Therefore, it would be of interest to determine how spectral energetics of extratropical baroclinic waves depend on the parameters controlling the energy dissipation of the model.

We already noted that the spatial scale of quasi–stationary waves is bet-

ter captured at T106L31 respect to T31L19 and T42L31. Increasing the horizontal resolution of the model seems to positively affect the simulation of the observed quasi–stationary wave activity. However, the vertical resolution should be increased consistently with the horizontal one. Roeckner et al. (2006) found that the systematic error of the extratropical SH mean state, and in particular the latitude of the SH jet stream, is notably dependent on the relative ratio between the horizontal and the vertical resolution of the model. Using QG scaling arguments, they justified this dependance with the existence of a range of preferential relative ratios, that are associated to a better simulation of extratropical baroclinic processes. Applying the diagnostics developed in this thesis to a wider set of AMIP experiments, where horizontal and vertical resolutions are independently changed, would help to effectively address this issue.

We have so far concluded that the error in the simulated mean state, via Rossby theory, can be linked to the error in the spatial scale of quasi–stationary patterns, and that the error in mean state might itself partially result from a mis–representation of the energetics of baroclinic processes. However, this solely perspective does not explain why the T42L31 model features the highest anomalous power on the quasi–stationary wave five, despite it captures the overall energetics and the mean state better than the T31L19 model. The baroclinic paradigm developed in the aquaplanet is of value for interpreting this error. At the resolution T42L31, the spectral distribution of the total kinetic energy along the main dispersion relation is entirely slightly displaced toward more negative frequencies (westward propagation). This applies on a wide range of spatial scales (k=4–7), which includes quasi–stationary and eastward propagating components. Therefore, the error does not simply regard the quasi–stationary wave activity but it is systematically affecting the baroclinic waves of the model. We speculate that this particular ratio between the horizontal and the vertical resolution might not be adequate for correctly capturing baroclinic processes. This could explain why Roeckner et al. (2006) found no significant improvements in the simulated

mean state of the model passing from T42L19 to T42L31.

We found that ERA–INTERIM and NCEP–DOE reanalyses feature a remarkable different intensity in the non linear kinetic energy transfer on the quasi–stationary waves k=4 and k=5. It would be important, for better validating climate models, to reduce this uncertainty. Nonetheless, we also observe a trend toward stronger non linear interactions in the ECHAM5 model as resolution is increased. This suggests that Reanalyses might themselves be affected by the systematic error of their atmospheric models. The weaker non linearity of NCEP–DOE reanalysis could be in particular explained by its coarser horizontal resolution. These results suggest that investigating AMIP experiments of different resolutions and numerics could be considered an interesting methodological approach for *analysing* the error of Reanalyses.

The improved simulation of the mean state with the model resolution is especially evident on the Atlantic and the Indian oceans, where the stronger baroclinic activity and the extratropical jet stream are mainly confined. Only minor improvements are instead found over the Pacific. It would be important to increase the understanding in what controls the mean state over this region, and what could be the dynamical consequences of its bad simulation. For instance, the analysis of Rossby stationary wave number reveals that such a mean state is inadequate for confining quasi–stationary waves to extratropical latitudes. This could explain the anomalous structure of the simulated quasi–stationary waves, which feature, independently from resolution, an arching wave over the Pacific. Because of this arching structure, which is especially strong at T31L19 and T106L31, we find it is particularly difficult to interpret the errors of the model by simply applying the theory developed in the aquaplanet. Moreover, different mechanisms could be participating in maintaing these patterns. At T31L19 we found that tropical convection over maritime continent could be important for triggering the wave. On the contrary, at T106L31 the pattern directly originates in the central Pacific, and an extratropical non–linear process, such as atmospheric blocking (Renwick and Revell, 1999), could be forcing the wave. The quasi–

stationary activity found at T42L31 is instead more closely resembling the quasi–stationary waves found in the aquaplanet, but we still miss an explanation justifying why its longitudinal phase remains approximately fixed instead of being slowly propagating. We speculate that tropical convection could be important for fixing the longitudinal phase, and it could be interesting to adapt the *symmetrised convection experiment* to the study of tropical–extratropical interaction in the Earth's climate.

We finally conclude that the marginally stable baroclinic paradigm is a new intriguing approach for interpreting the formation of quasi–stationary extratropical atmospheric waves. This is of value for analysing the atmospheric variability in the Southern Hemisphere climate, and for identifying the errors committed by state of the art climate models. From a dynamical perspective, many other processes can in the real world sustain such waves, and trying to explain all the cases using the aquaplanet model would be an unsuccessful attempt of over simplification. What is important to stress is instead the value of the theory for explaining the energetics of quasi–stationary waves, and for linking their properties to the average baroclinicity of the system. This is also of interest for climate change science, as the marginally stable condition can be affected by the increase in SST. Therefore, future quasi–stationary wave patterns could result remarkably different from those observed nowadays, provided that an almost stable baroclinic component is destabilised by the increased greenhouse forcing.

Appendix A

Notation

φ	latitude
λ	longitude
p	pressure
u	zonal wind field
v	meridional wind field
T	temperature
ξ	vorticity
D	divergence
$\vec{V}$	horizontal wind vector (u, v)
ψ	streamfunction
ϕ	geopotential
α	specific volume
ρ	density
ω	vertical velocity on pressure levels
K	kinetic energy of horizontal motions
$\vec{F}$	momentum drag vector (F_u, F_v)
Q^ν	1D quadrature spectrum
P^ν	1D cospectrum
P_k^ν	2D cospectrum

$[a]$	zonal average
a^*	deviation from zonal average
$\overline{a}$	time average
a'	deviation from time average
$\{a\}$	meridional area weighted average
$\tilde{a}$	deviation from meridional average
f	Coriolis parameter
β	meridional derivative of f
W_φ	weight of the area element

Appendix B

Acronyms

AGCM Atmospheric General Circulation Model

AMIP Atmospheric Model Intercomparison Project

AOGCM Atmosphere–Ocean General Circulation Model

APE AquaPlanet Experiment

CAPE Convective Available Potential Energy

DOE Department Of Energy

ECMWF European Centre for Medium–Range Weather Forecast

ENSO El Nino Southern Oscillation

EOF Empirical Orthogonal Function

FFT Fast Fourier Transform

GCM General Circulation Model

MJO Madden Julian Oscillation

NCEP National Center for Environmental Prediction

NOAA National Oceanic Atmospheric Administration

OLR	Outgoing Longwave Radiation
PDF	Probability Distribution Function
PSD	Power Spectral Density
QG	Quasi–Geostrophic
SST	Sea Surface Temperature
SIC	Sea Ice Concentration
TOA	Top Of the Atmosphere
WKBJ	Wentzel–Kramers–Brillouin–Jeffreys

Appendix C

Spectral analysis

There is fundamental difference between performing a *spectral analysis* and an *harmonic analysis*. Harmonic analysis aims to identifying the dominant Fourier components of a *specific* time series. This can be performed by computing a Fast Fourier Transform (FFT), and by identifying the frequencies where the squared module of the FFT is higher. On the contrary, spectral analysis focuses on inferring the power spectral density of a stochastic process by analysing finite time series which are particular realisations of the stochastic process itself (Bloomfield, 1976). The two analysis are therefore conceptually very different, despite in practice they result to be strictly connected. A remarkable result shows that a good estimator of the power spectral density (PSD) of a stochastic process is obtained by smoothing the Fourier Transform of the actual available realisations (Priestley, 2001). In the thesis, by adopting the methods introduced by Hayashi, spectral analysis is used for estimating the average spectral properties of the energetics and the kinematics of the waves propagating in the atmosphere. The Hayashi spectra are computed by smoothing the FFTs and details about the smoothing process will be giving in sec. C.2. In the next section we define what are the cospectrum and the quadrature spectrum of a bivariate stochastic process, as these spectral quantities are fundamental for performing the quadrature spectrum analysis involved in Hayashi spectra.

C.1 Co and quadrature spectra

Two stochastic processes X_r and X_s form a bivariate stationary stochastic process (X_r,X_s) if the following conditions are satisfied:

1. X_r and X_s are each stationary stochastic processes, so that their means (μ_r, μ_s) and their variances (σ_r, σ_s) are independent of time
2. The cross–covariance function $R^\tau(X_r, X_s)$ between X_r and X_s is only a function of the lag τ.

Under these conditions, the co–spectrum P^ν and the quadrature spectrum Q^ν between X_r and X_s are respectively defined as the real and the imaginary part of the Fourier transform in the lag of the cross–covariance matrix $R^\tau(X_r, X_s)$:

$$P^\nu - iQ^\nu = \frac{1}{2\pi} \sum_{\tau=-\infty}^{\infty} R^\tau \exp(-i2\pi\nu\tau) \tag{C.1}$$

$$R^\tau = \int_{-1/2}^{1/2} (P^\nu - iQ^\nu) e^{i2\pi\nu\tau} 2\pi d\nu, \tag{C.2}$$

where the inverse transform has been shown for completeness. $C^\nu = P^\nu - iQ^\nu$ is also called the complex cross–spectrum of X_r and X_s. In the *lag correlation method* the observed finite realisations of X_r and X_s are used for estimating R^τ, so that P^ν and Q^ν can be directly computed by applying Eq. C.1. In the FFT method, which is the one adopted in the thesis and which will be now explained, a rather different approach is instead used. An advantage of introducing such a method is that it allows to easily interpret the physical meaning of P^ν and Q^ν.

Let's introduce two real–valued deterministic processes $u_r(t)$ and $u_s(t)$:

$$u_r(t) = \sum_\nu U_r \cos(2\pi\nu t) \tag{C.3}$$

$$u_s(t) = \sum_\nu U_s \cos(2\pi\nu t + \delta_\nu), \tag{C.4}$$

where the summation is performed over a finite set of frequencies, $U_r^2/2$ and $U_s^2/2$ are the variance of each frequency component, and δ_ν is the phase

difference between the two signals at frequency ν. The couple $(u_r(t), u_s(t))$ can be considered as a particular realisation of a stationary bivariate process featuring a discrete spectrum of frequencies (ν_n, n=1,...,N).

The discrete co–spectrum and the quadrature spectrum between u_r and u_s can be explicitly computed:

$$P^\nu(u_r, u_s) = +\frac{U_r U_s}{2}\cos(\delta_\nu) \tag{C.5}$$

$$Q^\nu(u_r, u_s) = -\frac{U_r U_s}{2}\sin(\delta_\nu). \tag{C.6}$$

To proof that these results apply, we now show that using the definitions C.5 and C.6 the cross–spectrum $P^\nu(u_r, u_s) - iQ^\nu(u_r, u_s)$ constitute a Fourier couple of the cross covariance function R^τ between $u_r(t)$ and $u_s(t)$ (see C.2). This is proved in the following lines:

$$R^\tau = \frac{1}{T}\int_0^T [u_r(\tau)u_s(t+\tau)]dt = \tag{C.7}$$

$$= \sum_\nu \frac{1}{T}\int_0^T U_r U_s[\cos^2(2\pi\nu t)\cos(2\pi\nu\tau + \delta_\nu) - \tag{C.8}$$

$$+ \cos(2\pi\nu t)\sin(2\pi\nu t)\sin(2\pi\nu\tau + \delta_\nu)]dt =$$

$$= \sum_\nu \frac{U_r U_s}{2}\cos(2\pi\nu\tau + \delta_\nu) = \tag{C.9}$$

$$= \sum_\nu P^\nu(u_r, u_s)\cos(2\pi\nu\tau) + Q^\nu(u_r, u_s)\sin(2\pi\nu\tau) = \tag{C.10}$$

$$= \sum_\nu \Re[(P^\nu(u_r, u_s) - iQ^\nu(u_r, u_s))\exp(i2\pi\nu\tau)], \tag{C.11}$$

where trigonometric addition formulas have been used in the computation, and the orthogonality of cosine functions allowed to take the summation on ν outside of the integral.

By inspecting Eq. C.5 and Eq. C.6, we deduce that $P^\nu \neq 0$ and $Q^\nu = 0$ implies that the two signals feature a coherent in phase ($\delta_n \sim 0$) or antiphase ($\delta_n \sim -\pi$) oscillation at frequency ν. On the contrary, $P^\nu = 0$ and $Q^\nu \neq 0$ requires the two signals to feature a coherent in quadrature ($\delta_n \pm \pi/2$) oscillation at frequency ν. Both P^ν and Q^ν will be non zero if the oscillations of the two fields are coherent but with an arbitrary phase difference.

The arguments presented for the deterministic signals can be directly extended for estimating the cross–spectrum of arbitrary stochastic time series $v_r(t)$ and $v_s(t)$. By applying a temporal FFT, they can be rewritten as:

$$v_r(t) = \sum_\nu a_r^\nu \cos(2\pi\nu t) + b_r^\nu \sin(2\pi\nu t) \tag{C.12}$$

$$v_s(t) = \sum_\nu a_s^\nu \cos(2\pi\nu t) + b_s^\nu \sin(2\pi\nu t), \tag{C.13}$$

where the a and b terms refer to the amplitudes of the cosine and sine coefficients of the Fourier decomposition, respectively. From Eq. C.5 and C.6 we know that

$$P^\nu(\cos(p), \cos(p)) = P^\nu(\sin(p), \sin(p)) = 1/2 \tag{C.14}$$

$$-Q^\nu(\cos(p), \sin(p)) = Q^\nu(\sin(p), \cos(p)) = 1/2 \tag{C.15}$$

$$P^\nu(\cos(p), \sin(p)) = P^\nu(\sin(p), \cos(p)) = 0 \tag{C.16}$$

$$Q^\nu(\cos(p), \cos(p)) = Q^\nu(\sin(p), \sin(p)) = 0, \tag{C.17}$$

where $p = 2\pi\nu t$. Therefore:

$$P^\nu(v_r, v_s) = \frac{1}{2}\overline{(a_r^\nu a_s^\nu + b_r^\nu b_s^\nu)} \tag{C.18}$$

$$Q^\nu(v_r, v_s) = \frac{1}{2}\overline{(b_r^\nu a_s^\nu - a_r^\nu b_s^\nu)}., \tag{C.19}$$

where the overline indicates an average over neighbouring frequency bins or over different ensembles. The formulas C.18 and C.19 constitute the FFT method of cospectral estimation.

C.2 Hayashi spectra

Hayashi (1971) proposed a generalised method to decompose the variance of a longitude–time field $u(\lambda, t)$ in the spectrum of the eastward and westward propagating waves of u:

$$[\overline{u^2}] = \sum_k \sum_\nu H_k^\nu(u) \cdot \Delta_\nu, \tag{C.20}$$

where $\overline{u}$ and $[u]$ stand for the temporal and zonal average of u respectively, $H_k^{\pm\nu}$ is the Hayashi spectral power of the eastward ($+\nu$) and westward ($-\nu$) propagating waves and Δ_ν is the frequency interval between neighbouring Fourier bins. The method is a generalisation of Deland (1964) quadrature spectral analysis and it is based on a zonal Fourier transform followed by a quadrature spectral analysis between the temporal series of the sine and the cosine coefficients of the zonal expansions. The Hayashi power spectrum is defined as:

$$H_k^{\pm\nu}(u) = (P^\nu(C_k, C_k) + P^\nu(S_k, S_k) \pm 2Q^\nu(C_k, S_k))/4, \tag{C.21}$$

where P^ν and Q^ν are the 1D cospectrum and quadrature spectrum on the time variable (see eq. C.18 and C.19), while $C_k(t)$ and $S_k(t)$ are the cosine and sine zonal Fourier coefficients of $u(\lambda, t)$:

$$u(\lambda, t) = u_0(t) + \sum_{k=1}^{N} C_k(t)\cos(k\lambda) + S_k(t)\sin(k\lambda) \tag{C.22}$$

The spectral contributions to the longitude–time covariance ($[\overline{uu'}]$) between two fields $u(\lambda, t)$ and $u'(\lambda, t)$, can also be rewritten in terms of 1D co– and quadrature spectra between the cosine and sine zonal expansion of u and u':

$$[\overline{uu'}] = \sum_k \sum_\nu P_k^\nu(u, u') \cdot \Delta_\nu \tag{C.23}$$

$$\begin{aligned} P_k^{\pm\nu}(u, u') =& (P^\nu(C_k, C'_k) + P^\nu(S_k, S'_k) \pm \\ & Q^\nu(C_k, S'_k) \mp Q^\nu(S_k, C'_k))/4, \end{aligned} \tag{C.24}$$

where $P_k^{\pm\nu}(u, u')$ is a 2D cospectrum, C_k and S_k refer to u while C'_k and S'_k refer to u'.

Hayashi's formulas have been criticised by Pratt (1976) because standing waves are not resolved but are seen as a couple of eastward and westward propagating waves of equal amplitude, thus limiting the only meaningful quantity to the difference between the power in the eastward and westward components. A variety of different approaches were thus developed to overcome this problem (Pratt, 1976; Hayashi, 1977; Fraedrich and Böttger, 1978).

Nevertheless we decided to attain to the first Hayashi formulation because in aquaplanet models there is no preferential phase and standing wave activity is of limited interest. Standing variance would just contain, depending on the formulation, noise or spectral power of quasi–stationary waves alternating an eastward to a westward propagation.

In the aquaplanet each spectrum is obtained as an average of 20 spectra computed on non overlapping 6 months long time windows. In the analysis of the Southern Hemisphere DJF variability, spectra are obtained by averaging 30 spectra computed on the DJF season of each year. In both cases, spectra have been further averaged over 3 neighbouring frequency bins.

C.3 Kinetic energy balance

The zonal and meridional momentum equations expressed in spherical geometry, flux form, and using pressure as a vertical coordinate are:

$$\frac{\partial u}{\partial t} = \left[-\frac{\partial uu}{\partial x} - \frac{\partial vu}{\partial y} - \frac{\partial \omega u}{\partial p} + \frac{\tan\varphi}{r} uv \right] + f\varphi v - \frac{\partial \phi}{\partial x} + F_u \tag{C.25}$$

$$\frac{\partial v}{\partial t} = \left[-\frac{\partial uv}{\partial x} - \frac{\partial vv}{\partial y} - \frac{\partial \omega v}{\partial p} - \frac{\tan\varphi}{r} uv \right] - f\varphi u - \frac{\partial \phi}{r\partial \varphi} + F_v, \tag{C.26}$$

where (C.27)

$$\frac{\partial(\quad)}{\partial x} = \frac{\partial(\quad)}{r\cos\varphi\partial\lambda} \tag{C.28}$$

$$\frac{\partial(\quad)}{\partial y} = \frac{\partial\cos\varphi(\quad)}{r\cos\varphi\partial\varphi}. \tag{C.29}$$

A description of the adopted notation can be found in appendix A. The terms in square brackets are the non linear convergence of zonal and meridional momentum due to advection processes and they will be referred to as C_u and C_v, respectively. A prognostic equation for the kinetic energy is obtained by multiplying Eq. C.25 and Eq. C.26 by u and v, respectively, and by adding them together:

$$\frac{\partial K}{\partial t} = \frac{\partial(u^2+v^2)/2}{\partial t} = uC_u + vC_v - \vec{V}\cdot\nabla\phi + \vec{V}\cdot\vec{F}. \tag{C.30}$$

The term $-\vec{V} \cdot \nabla\phi$, which represents the kinetic energy generation by ageostrophic motions down gradient of the geopotential field, can be rewritten in a form of deeper interpretative value for the energetics of the system:

$$-\vec{V} \cdot \nabla\phi = \phi\nabla \cdot \vec{V} - \nabla \cdot (\vec{V}\phi) \tag{C.31}$$

$$= -\phi\frac{\partial\omega}{\partial p} - \nabla \cdot (\vec{V}\phi) \tag{C.32}$$

$$= \omega\frac{\partial\phi}{\partial p} - \nabla \cdot (\vec{V}\phi) - \frac{\partial}{\partial p}(\phi\omega) \tag{C.33}$$

$$= -\alpha\omega - \left[\frac{\partial\phi u}{\partial x} + \frac{\partial\phi v}{\partial y} + \frac{\partial\phi\omega}{\partial p}\right], \tag{C.34}$$

where the continuity equation $\nabla \cdot \vec{V} + \frac{\partial\omega}{\partial p} = 0$ and the hydrostatic equation $\frac{\partial\phi}{\partial p} = -\alpha$ have been used in the first and in the last step, respectively. The first term of Eq. C.34 is the direct baroclinic energy conversion of potential into kinetic energy, and the second is the convergence of geopotential energy which is associated to the spatial redistribution of kinetic energy by the propagation of waves. The latter term therefore vanishes when the kinetic energy balance is integrated over the whole atmosphere.

If we now take the temporal and zonal average of eq. C.30, we can use relation C.23 to rewrite the balance equation in cospectral format. The resulting spectral balance for a component of frequency and wavenumber (k, ν) is:

$$0 = \frac{\partial K_k^\nu}{\partial t} = N_k^\nu - P_k^\nu(\alpha, \omega) - \left[\frac{\partial P_k^\nu(\phi, v)}{\partial y} + \frac{\partial P_k^\nu(\phi, \omega)}{\partial p}\right] + D_k^\nu, \tag{C.35}$$

where D_k^ν is the spectrum of kinetic energy sinks due to dissipation processes, K_k^ν is the kinetic energy spectrum, and N_k^ν is the non linear energy transfer spectrum. The explicit expressions for K_k^ν and N_k^ν are:

$$K_k^\nu = (P_k^\nu(u, u) + P_k^\nu(v, v))/2, \tag{C.36}$$

$$N_k^\nu = -P_k^\nu(u, \frac{\partial uu}{\partial x}) - P_k^\nu(v, \frac{\partial uv}{\partial x}) - P_k^\nu(u, \frac{\partial uv}{\partial y}) + P_k^\nu(v, \frac{\partial vv}{\partial y}) \tag{C.37}$$

$$+ \frac{\tan\varphi}{r}[P_k^\nu(u, uv) + P_k^\nu(v, uu)] - P_k^\nu(u, \frac{\partial u\omega}{\partial p}) + P_k^\nu(v, \frac{\partial v\omega}{\partial p}). \tag{C.38}$$

N_k^ν is positive when non linear interactions between atmospheric motions of different spatial and temporal scales maintain an average convergence of momentum which is in phase with the velocity field associated to the spectral component (k, ν). The energy transfer can occur or among triads of waves which are related in frequencies (and in wavenumbers) as ν, μ, $\nu \pm \mu$ (k, l, $k \pm l$), or due to the interaction of the wave (k, ν) with the time mean flow. The two processes are physically very different. In the former we talk of non linear wave–wave interactions, which on average leads to a kinetic energy flux from fast–short toward long–slow waves (Pedlosky, 1979). In the latter we talk of barotropic wave–mean flow interactions, which on average leads to damp the waves and to reinforce the time mean jets (Lorenz, 1967). It is therefore of interest to separate the two processes:

$$N_k^\nu =< K \cdot K >_k^\nu + < K_0 \cdot K_k^\nu >, \tag{C.39}$$

where $< K \cdot K >_k^\nu$ and $< K_0 \cdot K_k^\nu >$ refer to the energy transfer by wave–wave and by wave–mean flow interactions, respectively. By definition $< K \cdot K >_k^\nu$ can be computed as:

$$< K \cdot K >_k^\nu = -P_k^\nu(u, \frac{\partial u'u'}{\partial x}) - P_k^\nu(v, \frac{\partial u'v'}{\partial x}) - P_k^\nu(u, \frac{\partial u'v'}{\partial y}) + \tag{C.40}$$

$$+ P_k^\nu(v, \frac{\partial v'v'}{\partial y}) + \frac{\tan\varphi}{r}[P_k^\nu(u, u'v') + P_k^\nu(v, u'u')] + \tag{C.41}$$

$$- P_k^\nu(u, \frac{\partial u'\omega'}{\partial p}) + P_k^\nu(v, \frac{\partial v'\omega'}{\partial p}), \tag{C.42}$$

where the primes refer to deviations from the time mean state, so that only the convergence of momentum by wave–wave interactions is considered. Once $< K \cdot K >_k^\nu$ and N_k^ν are known, the barotropic energy transfer can be simply computed as a residual:

$$< K_0 \cdot K_k^\nu >= N_k^\nu - < K \cdot K >_k^\nu \tag{C.43}$$

Combining Eq. C.35 to Eq. C.39, we get the final form of the spectral kinetic energy balance at a given latitude:

$$0 =< K \cdot K >_k^\nu + < K_0 \cdot K_k^\nu > -P_k^\nu(\alpha, \omega) - \left[\frac{\partial P_k^\nu(\phi, v)}{\partial y} + \frac{\partial P_k^\nu(\phi, \omega)}{\partial p}\right] + D_k^\nu. \tag{C.44}$$

When dealing with the global energetics, Eq. C.44 has to be integrated over the whole atmosphere. The term in bracket disappears and Eq. 4.3, which is used to proof the baroclinic nature of the wave five in the aquaplanet, is therefore recovered.

C.4 Meridional decomposition

To focus the attention on baroclinic process, it can be useful to meridionally integrate Eq. C.44 just over the latitudes corresponding to the extratropical baroclinic band. In this case, the term in brackets is in general different from zero and it gives the kinetic energy tendency in the region due to fluxes of kinetic energy at the boundaries of the latitudinal band. This is mostly associated to waves escaping out of the baroclinic zone and propagating toward the tropics.

When focusing on a zonal band it is also possible to analyse the contributions to the kinetic energy balance as a function of the meridional scale of the waves. This can be accomplished by meridionally decomposing the fields between the meridional average in the band and the deviation from the mean:

$$a = \{a\} + \tilde{a}, \tag{C.45}$$

where a is a generic field, and $\{a\}$ and $\tilde{a}$ are respectively the meridional average and the deviation from the mean in the latitude band. We will refer to these two components as the *mean wave* and the *deviation wave*, respectively.

To demonstrate that this decomposition works as a filter on the meridional scale, let's compute the kinetic energy of a wave in a one layer zonal channel of coordinates $x \in [0, 1]$ and $y \in [-1/2, 1/2]$. The wave is defined by the following streamfunction:

$$\psi(x, y) = \sin(2\pi k x)\cos(\pi l y), \tag{C.46}$$

where k and l are respectively the zonal and meridional wavenumber of the

wave. The zonal and meridional motions associated to this perturbation are:

$$u(x,y) = -\frac{\partial \psi}{\partial y} = \pi l \sin(2\pi k x)\sin(\pi l y) \tag{C.47}$$

$$v(x,y) = \frac{\partial \psi}{\partial x} = 2\pi k \cos(2\pi k x)\cos(\pi l y) \tag{C.48}$$

For the sake of simplicity, we will now focus the attention on the kinetic energy by meridional motions, as similar results can be obtained when zonal motions are considered. The total kinetic energy (K_v), the kinetic energy due to the mean wave ($\{K_v\}$) and the kinetic energy due to the deviation wave ($\tilde{K_v}$) respectively are:

$$K_v = \int_0^1 \int_{-1/2}^{1/2} v^2 dy\, dx = \frac{k\pi}{2}\left[\frac{2}{\pi l}\cos(\pi l/2)\sin(\pi l/2) + 1\right] \tag{C.49}$$

$$\{K_v\} = \int_0^1 \int_{-1/2}^{1/2} \{v\}^2 dy\, dx = \frac{4k}{\pi l^2}\sin\left(\frac{\pi l}{2}\right)^2 \tag{C.50}$$

$$\tilde{K_v} = \int_0^1 \int_{-1/2}^{1/2} \tilde{v}^2 dy\, dx = \int_0^1 \int_{-1/2}^{1/2} (v - \{v\})^2 dy\, dx = K_v - \{K_v\} \tag{C.51}$$

In Fig. C.1 we plot the relative projection of K_v into $\{K_v\}$ and into $\tilde{K_v}$ as a function of l. For $l \leq 1$ the kinetic energy mainly projects on the mean wave, while as l increases the projection on the deviation wave becomes predominant. In particular for $l \geq 2$, which implies a meridional wavelength smaller than the width of the latitudinal band, the deviation wave explains more than the 90% of the total kinetic energy by meridional motions. Therefore the kinetic energy of the waves as large as the latitudinal band preferentially project on the mean wave, while the energy of the wave featuring a smaller meridional scale preferentially project on the deviation wave.

The average sources and sinks of kinetic energy indicated in Eq. C.44, which are all cospectral quantities of the form $P_k^\nu(a,b)$, can be rewritten adopting the above introduced meridional decomposition. If we sum over all the frequencies and wavenumbers of $P_k^\nu(a,b)$ and further apply a meridional

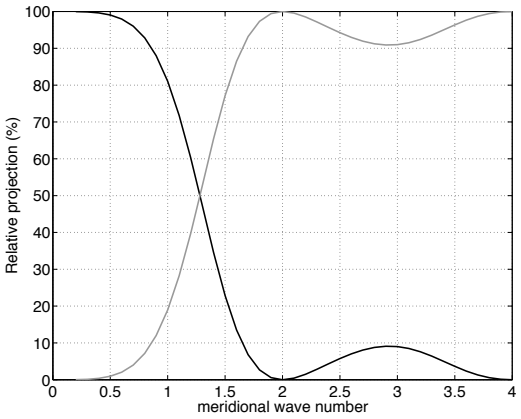

Figure C.1: Relative projection of the kinetic energy due to meridional motions of a wave into the kinetic energy (black line) of the meridionally averaged component and (grey line) of the component not projecting on the meridional average. The relative contributions are shown as a function of the meridional wavenumber of the wave.

average over a latitudinal band, we obtain:

$$\{\sum_{k,\nu} P_k^\nu(a,b)\} = \{\overline{[ab]}\} = \overline{[\{(\{a\}+\tilde{a})(\{b\}+\tilde{b})\}]} = \overline{[\{a\}\{b\}]} + \overline{[\{\tilde{a}\tilde{b}\}]}$$
$$= \sum_{k,\nu} P_k^\nu(\{a\},\{b\}) + \sum_{k,\nu}\{P_k^\nu(\tilde{a},\tilde{b})\}, \tag{C.52}$$

where Eq. C.23, the relations $\{\tilde{a}\} = 0$ and $\{\{a\}\} = \{a\}$, and an exchange between the meridional and the temporal and zonal averages, have been used in the computation. The contribution to the cospectral power due to waves as large as (smaller than) the latitudinal band is mostly given by $P_k^\nu(\{a\},\{b\})$ ($\{P_k^\nu(\tilde{a},\tilde{b})\}$), respectively.

Appendix D

Lanczos filter

Digital filters aim to predictably change the power spectrum of a discrete time series x_t. The frequency response function $R(\nu)$, which gives the linear relationship between the power spectral density of the input $X(\nu)$ and output $Y(\nu)$ signals, objectively defines the filter in the frequency domain:

$$Y(\nu) = R(\nu) \cdot X(\nu). \tag{D.1}$$

The general formal of a linear filter in the time space can be obtained by applying an anti–Fourier transform to Eq. D.1, and by further using the convolution theorem (Priestley, 2001) for rewriting the rhs as the convolution between a window function w_k and the input time series:

$$y_t = \sum_{k=-\infty}^{k=\infty} w_k x_{t-k}, \tag{D.2}$$

where y_t is the filtered time series and the weights w_k, which constitute the window function, are the anti–Fourier transform of $R(\nu)$.

In theory, a filter can be simply designed in the frequency space by choosing the desired $R(\nu)$, and then directly applied in the time space once the appropriate set of corresponding w_k are computed. But for practical usage, the series in Eq. D.2 has to be replaced by a finite summation over k, and only a finite number of weights have to be retained in the window function.

When step response functions are desired, truncating w_k creates an oscillation in $R(\nu)$, which is called the Gibbs phenomenon, that badly affects the properties of the designed filter. The approach introduced by Lanczos (Lanczos, 1956; Duchon, 1979) allows to minimise this phenomenon.

A low pass Lanczos filter in the time space is defined as follows:

$$w_k = \frac{\sin 2\pi f_c k}{\pi k} \frac{\sin \pi k/n}{\pi k/n}, \quad k = -n, \ldots, 0, \ldots, n \tag{D.3}$$

$$y_t = \sum_{k=-n}^{k=n} w_k x_{t-k} \tag{D.4}$$

where f_c is the cut-off frequency and n is linked to the length of the window $(2n + 1)$. These are the only two parameters needed for determining the properties of the filter. The first term on the rhs of eq. D.3 is the window function of an ideal low pass filter, while the second term is the correction introduced by Lanczos for minimising the Gibbs phenomenon. As shown by Duchon (1979), increasing n generally improves the performance of the filter as the transition between the retained and the filtered components in the response function becomes steeper.

Three different settings of the lanczos low pass filter, which are differing in the cut–off frequency (f_c) and in the filter length (n), have been adopted in the thesis:

- $f_c = (7\,\text{days})^{-1}$ and $n = 29$
- $f_c = (10\,\text{days})^{-1}$ and $n = 50$
- $f_c = (30\,\text{days})^{-1}$ and $n = 50$.

The respective response functions, which have been directly computed by filtering a white noise signal and by evaluating the fraction of the retained spectral power as a function of frequency, are plotted in Fig. D.1.

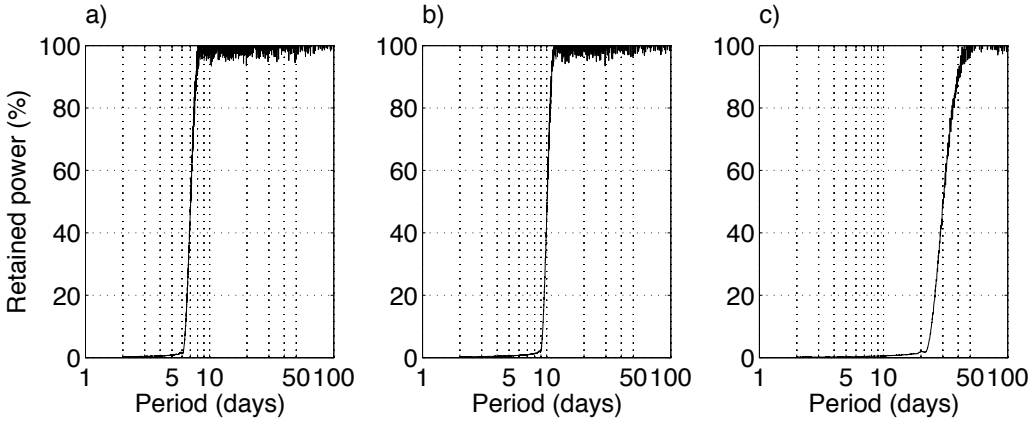

Figure D.1: Fraction of retained power after filtering a white noise signal with a low pass Lanczos filter featuring the following parameters: a) $f_c = (7\,\text{days})^{-1}$ and $n = 29$, b) $f_c = (10\,\text{days})^{-1}$ and $n = 50$, c) $f_c = (30\,\text{days})^{-1}$ and $n = 50$

Acknowledgments

I wish to dearly thank Antonio Navarra for giving me the opportunity of choosing my research project, for supervising my activity, and for teaching me the importance of looking toward sufficiently challenging scientific results. I am extremely grateful to Valerio Lucarini for his precious scientific collaboration, for his constant enthusiasm and positive thinking and for the time he dedicated to discuss together the issues I've had to face during this research. I would like to sincerely acknowledge Chiara Cagnazzo and Silvio Gualdi who carefully read a preliminary draft of the thesis and gave useful comments for its improvement. My gratitude goes also to Beppe Fogli for teaching me how to deal with the atmospheric model, and to Annalisa Cherchi for helping in the set–up of the AMIP experiments. I thank CMCC and Ca'Foscari University for their financial support, and all the colleagues for making CMCC an enjoyable working place.

I'm truly grateful to the department of Meteorology of the University of Reading for kindly hosting me for a six months period, which highly increased my scientific curiosity and enriched my knowledge in atmospheric dynamics. A very special thank goes to Mike Blackburn, for the many stimulating discussions, and to John Methven and Brian Hoskins for their useful comments on the stability of waves in linear models of the atmosphere. I'm also grateful to Dave Williamson for first introducing me to the problem of quasi–stationary waves in aquaplanet models.

I acknowledge NOAA and ECMWF for making available the reanalyses data. I wish to thank Andrea Storto for kindly helping in the retrieval of

ERA–INTERIM data, while NCEP–DOE reanalysis data was provided by the NOAA/OAR/ESRL PSD, Boulder, Colorado (USA) from their website.

These three years of work would not have been as happy without the kind support and friendship from all the students of the *second floor* and from the housemates of *Via Gigli* and *Via degli Angeli*, whom I warmly thank for sharing the joy of living in Bologna together. I'm finally indebted to my parents, Babbo e Mamma, whom I sincerely thank for the affection I've always been feeling extremely warm, and for giving me kind support and help throughout the difficulties.

Bibliography

Ambrizzi, T. and B. Hoskins, 1997: Stationary rossby-wave propagation in a baroclinic atmosphere. *Q. J. Roy. Meteor. Soc.*, **123**, 919–928.

Basdevant, C., B. Legras, R. Sadourny, and M. Béland, 1981: A Study of Barotropic Model Flows: Intermittency, Waves and Predictability. *J. Atmos. Sci.*, **38**, 2305–2326.

Benzi, R., P. Malguzzi, A. Speranza, and A. Sutera, 1986: The statistical properties of general atmospheric circulation: observational evidence and a minimal theory of bimodality. *Quart. J. R. Met. Soc.*, **112**, 661–674, doi:10.1002/qj.49711247306.

Berbery, E. and C. Vera, 1996: Characteristics of the southern hemisphere winter storm track with filtered and unfiltered data. *J. Atmos. Sci*, **53**, 468–481.

Blackburn, M., J. Methven, and N. Roberts, 2008: Large-scale context for the UK floods in summer 2007. *Weather*, **63**, 280–288, doi:10.1002/wea.322.

Blackmon, M. L., Y.-H. Lee, and J. M. Wallace, 1984: Horizontal Structure of 500 mb Height Fluctuations with Long, Intermediate and Short Time Scales. *J. Atmos. Sci.*, **41**, 961–980.

Bloomfield, P., 1976: *Fourier analysis of time series: an introduction*. Wiley Series in Probability and Mathematical Statistics.

Boer, G., 2000: *Analysis and verification of model climate, chap 3. Numerical modelling of the Global Atmosphere*. NATO Science Series.

Boer, G. and S. Lambert, 2008: The energy cycle in atmospheric models. *Clim. Dynam.*, **30**, 371–390.

Bourke, W., 1972: An efficient, one-level, primitive-equation spectral model. *Mon. Weather Rev.*, **100**, 683–689.

Branstator, G., 1992: The Maintenance of Low-Frequency Atmospheric Anomalies. *J. Atmos. Sci.*, **49**, 1924–1946.

Branstator, G., 2002: Circumglobal Teleconnections, the Jet Stream Waveguide, and the North Atlantic Oscillation. *J. Climate*, **15**, 1893–1910.

Cai, M. and M. Mak, 1990: Symbiotic Relation between Planetary and Synoptic-Scale Waves. *J. Atmos. Sci.*, **47**, 2953–2968.

Catto, J. L., L. C. Shaffrey, and K. I. Hodges, 2010: Can Climate Models Capture the Structure of Extratropical Cyclones? *J. Climate*, **23**, 1621–1635.

Chang, E. K. M. and D. B. Yu, 1999: Characteristics of wave packets in the upper troposphere. part i: Northern hemisphere winter. *J. Atmos. Sci.*, **56**, 1708–1728.

Charney, J. G., 1971: Geostrophic turbulence. *J. Atmos. Sci.*, **28**, 1087–1095.

Chen, T., 2002: A North Pacific Short-Wave Train during the Extreme Phases of ENSO. *J. Climate*, **15**, 2359–2376.

Deland, R. J., 1964: Travelling planetary waves. *Tellus*, **16**, 271–273.

Dell'Aquila, A., V. Lucarini, P. M. Ruti, and S. Calmanti, 2005: Hayashi spectra of the northern hemisphere mid-latitude atmospheric variability in the NCEP–NCAR and ECMWF reanalyses. *Clim. Dynam.*, **25**, 639–652, doi:10.1007/s00382-005-0048-x.

Dell'Aquila, A., P. M. Ruti, S. Calmanti, and V. Lucarini, 2007: Southern hemisphere midlatitude atmospheric variability of the NCEP-NCAR and ECMWF reanalyses. *J. Geophys. Res.*, **112**, D08 106, doi: 10.1029/2006JD007376.

Ding, Q. and B. Wang, 2005: Circumglobal Teleconnection in the Northern Hemisphere Summer. *J. Climate*, **18**, 3483–3505.

Duchon, C., 1979: Lanczos Filtering in One and Two Dimensions. *J. Appl. Meteorol.*, **18**, 1016–1022.

Eady, E. T., 1949: Long waves and cyclone wave. *Tellus*, **1**, 33–52.

Efron, B. and R. Tibshirani, 1993: *An introduction to the bootstrap*. Chapman and Hall.

Fraedrich, K. and H. Böttger, 1978: A wavenumber-frequency analysis of the 500 mb geopotential at 50N. *J. Atmos. Sci.*, **35**, 745–750.

Frierson, D., I. Held, and P. Zurita-Gotor, 2006: A gray-radiation aquaplanet moist GCM. Part I: Static stability and eddy scale. *J. Atmos. Sci.*, **63**, 2548–2566.

Ghil, M. and K. Mo, 1991: Intraseasonal oscillations in the global atmosphere. Part II: Southern Hemisphere. *J. Atmos. Sci.*, **48**, 780–790.

Green, J. S. A., 1960: A problem in baroclinic stability. *Quart. J. Roy. Meteor. Soc.*, **86**, 237–251, doi:10.1002/qj.49708636813.

Gruber, A. and A. Krueger, 1984: The status of the NOAA outgoing longwave radiation data set. *Bull. Amer. Meteor. Soc*, **65**, 958–962.

Hayashi, Y., 1971: A generalized method of resolving disturbances into progressive and retrogressive waves by space fourier and time cross-spectral analyses. *J. Meteor. Soc. Japan*, **49**, 125–128.

Hayashi, Y., 1977: On the coherence between progressive and retrogressive waves and a partition of space-time power spectra into standing and traveling parts. *J. Appl. Meteorol.*, **16**, 368–373.

Hayashi, Y., 1980: Estimation of Nonlinear Energy Transfer Spectra by the Cross-Spectral Method. *J. Atmos. Sci.*, **37**, 299–307.

Hayashi, Y., 1982: Space-time spectral analysis and its applications to atmospheric waves. *J. Meteor. Soc. Japan*, **60**, 156–171.

Hayashi, Y. and D. G. Golder, 1977: Space-Time Spectral Analysis of Mid-Latitude Disturbances Appearing in a GFDL General Circulation Model. *J. Atmos. Sci.*, **34**, 237–262.

Held, I., 2000: The general circulation of the atmosphere. *Proc. Prog. Geophys. Fluid Dyn.*

Held, I., 2005: The gap between simulation and understanding in climate modeling. *Bull. Amer. Meteor. Soc*, 1609–1614.

Held, I. and A. Hou, 1980: Nonlinear axially symmetric circulations in a nearly inviscid atmosphere. *J. Atmos. Sci.*, **37**, 515–533.

Held, I. M., M. Ting, and H. Wang, 2002: Northern winter stationary waves: Theory and modeling. *J. Climate*, **15**, 2125–2144.

Hendon, H. H. and D. L. Hartmann, 1985: Variability in a Nonlinear Model of the Atmosphere with Zonally Symmetric Forcing. *J. Atmos. Sci.*, **42**, 2783–2797.

Holton, J. R., 2004: *An Introduction to Dynamic Meteorology*. Elsevier Academic Press, 535 pp.

Hoskins, B. and K. Hodges, 2005: A new perspective on southern hemisphere storm tracks. *J. Atmos. Sci*, **18**, 4108–4129.

Hoskins, B. J. and T. Ambrizzi, 1993: Rossby Wave Propagation on a Realistic Longitudinally Varying Flow. *J. Atmos. Sci.*, **50**, 1661–1671.

Hoskins, B. J. and D. J. Karoly, 1981: The Steady Linear Response of a Spherical Atmosphere to Thermal and Orographic Forcing. *J. Atmos. Sci.*, **38**, 1179–1196.

Hoskins, B. J. and M. J. Revell, 1981: The Most Unstable Long Wavelength Baroclinic Instability Modes. *J. Atmos. Sci.*, **38**, 1498–1503.

Inatsu, M. and B. Hoskins, 2004: The zonal asymmetry of the southern hemisphere winter storm track. *Journal of Climate*, **17**, 4882–4892.

Jin, F. and B. Hoskins, 1995: The direct response to tropical heating in a baroclinic atmosphere. *J. Atmos. Sci*, **52**, 307–319.

Kalnay, E., et al., 1996: The NCEP/NCAR 40-year reanalysis project. *Bull. Amer. Meteor. Soc*, **77**, 437–471.

Kanamitsu, M., W. Ebisuzaki, J. Woollen, S. Yang, J. J. Hnilo, M. Fiorino, and G. L. Potter, 2002: NCEP-DOE AMIP-II reanalysis (R-2). *Bull. Amer. Meteor. Soc*, **83**, 1631–1643.

Karoly, D., 1989: Southern hemisphere circulation features associated with El Niño-Southern Oscillation events. *Journal of Climate*, **2**, 1239–1252.

Kemball-Cook, S., B. Wang, and X. Fu, 2002: Simulation of the Intraseasonal Oscillation in the ECHAM-4 Model: The Impact of Coupling with an Ocean Model. *J. Atmos. Sci*, **59**, 1433–1452.

Kidson, J. W., 1999: Principal Modes of Southern Hemisphere Low-Frequency Variability Obtained from NCEP-NCAR Reanalyses. *J. Climate*, **12**, 2808–2830.

Kiladis, G., 1998: Observations of rossby waves linked to convection over the eastern tropical pacific. *J. Atmos. Sci.*, **55**, 321–339.

Kiladis, G. and S. Feldstein, 1994: Rossby wave propagation into the tropics in two gfdl general circulation models. *Clim. Dynam.*, **9**, 245–252.

Kiladis, G. and K. Weickmann, 1992: Extratropical forcing of tropical pacific convection during northern winter. *Mon. Weather Rev.*, **120**, 1924–1938.

Kiladis, G. N., M. C. Wheeler, P. T. Haertel, K. H. Straub, and P. E. Roundy, 2009: Convectively coupled equatorial waves. *Rev. Geophys.*, **47**, RG2003, doi:10.1029/2008RG000266.

Kug, J.-S., F.-F. Jin, J. Park, H.-L. Ren, and I.-S. Kang, 2010: A general rule for synoptic-eddy feedback onto low-frequency flow. *Clim. Dynam.*, **35**, 1011–1026, doi:10.1007/s00382-009-0606-8.

Lanczos, C., 1956: *Applied Analysis*. Prentice-Hall, 539 pp.

Lander, J. and B. Hoskins, 1997: Believable scales and parameterizations in a spectral transform model. *Mon. Weather Rev.*, **125**, 292–303.

Larichev, V. D. and I. M. Held, 1995: Eddy Amplitudes and Fluxes in a Homogeneous Model of Fully Developed Baroclinic Instability. *J. Phys. Oceanogr.*, **25**, 2285–2297.

Lau, K., P. Sheu, and I. Kang, 1994: Multiscale low-frequency circulation modes in the global atmosphere. *J. Atmos. Sci.*, **51**, 1169–1193.

Lau, N. C., 1988: Variability of the observed midlatitude storm tracks in relation to low-frequency changes in the circulation pattern. *J. Atmos. Sci.*, **45**, 2718–2743.

Lee, S. and I. Held, 1993: Baroclinic wave packets in models and observations. *J. Atmos. Sci.*, **50**, 1413–1428.

Liebmann, B. and C. Smith, 1996: Description of a complete (interpolated) outgoing longwave radiation dataset. *Bull. Amer. Meteor. Soc*, **77**, 1275–1277.

Lim, G. H. and J. M. Wallace, 1991: Structure and Evolution of Baroclinic Waves as Inferred from Regression Analysis. *J. Atmos. Sci.*, **48**, 1718–1732.

Lin, C. A. and A. C. M. Chan, 1989: Baroclinic instability and the summer southern hemisphere wavenumber 5 circulation. *Geophys. Astro. Fluid.*, **47**, 19–42, doi:10.1080/03091928908221815.

Lin, J. L., 2007: The Double-ITCZ Problem in IPCC AR4 Coupled GCMs: Ocean Atmosphere Feedback Analysis. *J. Climate*, **20**, 4497.

Lin, J. L., K. M. Weickmann, and G. N. Kiladis, 2006: Tropical intraseasonal variability in 14 IPCC AR4 climate models. Part I: Convective signals. *Journal of Climate*, **19**, 2665–2690.

Lin, S. J. and R. B. Rood, 1996: Multidimensional flux-form semi-lagrangian transport. *Mon. Weather Rev.*, **124**, 2046–2068.

Lindzen, R. S. and M. Fox-Rabinovitz, 1989: Consistent vertical and horizontal resolution. *Mon. Weather Rev.*, **117**, 2575–2583.

Lohmann, U. and E. Roeckner, 1996: Design and performance of a new cloud microphysics scheme developed for the ECHAM4 general circulation model. *Clim. Dyn.*, **12**, 557–572.

Lorenz, E. N., 1967: *The nature and theory of the general circulation of the atmosphere*. World Meteorological Organization, 161 pp.

Louis, J., 1979: A parametric model of vertical eddy fluxes in the atmosphere. *Boundary-Layer Meteorology*, **17 (2)**, 187–202.

Lucarini, V., S. Calmanti, A. Dell'Aquila, P. M. Ruti, and A. Speranza, 2007: Intercomparison of the northern hemisphere winter mid-latitude atmospheric variability of the IPCC models. *Clim. Dynam.*, **28**, 829–848, doi:10.1007/s00382-006-0213-x.

Lucarini, V. and F. Ragone, 2010: Energetics of PCMDI/CMIP3 Climate Models: Net Energy Balance and Meridional Enthalpy Transport. *Rev. Geophys.*, doi:10.1029/2009RG000323.

Mo, K., 2000: Relationships between low-frequency variability in the southern hemisphere and sea surface temperature anomalies. *Journal of Climate*, **13**, 3599–3610.

Mo, K. and R. Higgins, 1998: The pacific–south american modes and tropical convection during the southern hemisphere winter. *Mon. Weather Rev.*, **126**, 1581–1596.

Navarra, A. and V. Simoncini, 2010: *A Guide to Empirical Orthogonal Functions for Climate Data Analyisis*. Springer, 173 pp.

Neale, R. J. and B. J. Hoskins, 2001: A standard test for AGCMs including their physical parametrizations: I: the proposal. *Atmos. Sci. Lett.*, **1**, 101–107.

Nordeng, T. E., 1994: Extended versions of the convective parameterization scheme at ecmwf and their impact on the mean and transient activity of the model in the tropics. Tech. memo., European Centre for Medium-Range Weather Forecasts, 41 pp.

North, G., T. Bell, and R. Cahalan, 1982: Sampling errors in the estimation of empirical orthogonal functions. *Mon. Weather Rev.*, **110**, 699–706.

Parrish, D. F. and J. C. Derber, 1992: The national meteorological center's spectral statistical-interpolation analysis system. *Mon. Weather Rev.*, **120**, 1747–1763.

Pedlosky, J., 1979: *Geophysical Fluid Dynamics*. Springer-Verlag, 624 pp.

Peixoto, J. and A. Oort, 1992: *Physics of Climate*. Aip Press, 520 pp.

Philander, S. G., 1990: *El Nino, La Nina, and the southern oscillation*. Academic Press, Inc., 295 pp.

Pratt, R. W., 1976: The Interpretation of Space-Time Spectral Quantities. *J. Atmos. Sci.*, **33**, 1060–1066.

Priestley, M. B., 2001: *Spectral analysis and time series*. Academic Press, Inc., 890 pp.

Randall, D. A., et al., 2007: *Cilmate Models and Their Evaluation In: Climate Change 2007: The Physical Science Basis. Contribution of Working Group I to the Fourth Assessment Report of the Intergovernmental Panel on Climate Change*. Cambridge University Press.

Rao, V. and A. D. Carmo, 2002: Seasonal variations in the southern hemisphere storm tracks and associated wave propagation. *J. Atmos. Sci*, **59**, 1029–1040.

Rayner, N. A., D. E. Parker, E. B. Horton, C. K. Folland, L. V. Alexander, D. P. Rowell, E. C. Kent, and A. Kaplan, 2003: Global analyses of sea surface temperature, sea ice, and night marine air temperature since the late nineteenth century. *J. Geophys. Res*, **108**, 4407.

Renwick, J. A. and M. J. Revell, 1999: Blocking over the South Pacific and Rossby Wave Propagation. *Mon. Wea. Rev*, **127**, 2233–2247.

Revell, M., J. Kidson, and G. Kiladis, 2001: Interpreting low-frequency modes of southern hemisphere atmospheric variability as the rotational response to divergent forcing. *Mon. Weather Rev.*, **129**, 2416–2425.

Rhines, P. B., 1975: Waves and turbulence on a beta-plane. *J. Fluid Mech.*, **69**, 417–443.

Richter, I. and X. Shang-Ping, 2008: On the origin of equatorial atlantic biases in coupled general circulation models. *Clim. Dynam.*, **31**, 587–598.

Robert, A. J., 1982: A semi-Lagrangian and semi-implicit numerical integration scheme for the primitive meteorological equations. *J. Met. Soc. Japan*, **60**, 319–325.

Robertson, A. and C. Mechoso, 2003: Circulation regimes and low-frequency oscillations in the south pacific sector. *Mon. Weather Rev.*, **131**, 1566–1576.

Robinson, W. A., 1991: The dynamics of low-frequency variability in a simple model of the global atmosphere. *J. Atmos. Sci.*, **48**, 429–441.

Roeckner, E., et al., 2003: The atmospheric general circulation model ECHAM5. Part I: Model description. Tech. Rep. 349, Max Planck institute for Meteorology.

Roeckner, E., et al., 2006: Sensitivity of simulated climate to horizontal and vertical resolution in the ECHAM5 atmosphere model. *J. Climate*, **19**, 3771–3791.

Ruti, P. M., V. Lucarini, A. Dell'Aquila, S. Calmanti, and A. Speranza, 2006: Does the subtropical jet catalyze the midlatitude atmospheric regimes? *Geophys. Res. Lett.*, **33**, L06 814, doi:10.1029/2005GL024620.

Salby, M. L., 1982: A Ubiquitous Wavenumber-5 Anomaly in the Southern Hemisphere During FGGE. *Mon. Weather Rev.*, **110**, 1712–1721.

Sardeshmukh, P. D. and B. J. Hoskins, 1988: The generation of global rotational flow by steady idealized tropical divergence. *J. Atmos. Sci.*, **45**, 1228–1251.

Schneider, T., 2004: The tropopause and the thermal stratification in the extratropics of a dry atmosphere. *J. Atmos. Sci.*, **61**, 1317–1340.

Schneider, T., 2006: The general circulation of the atmosphere. *Annu. Rev. Earth Planet. Sci.*, **34**, 655–688.

Schneider, T. and C. C. Walker, 2006: Self-Organization of Atmospheric Macroturbulence into Critical States of Weak Nonlinear Eddy Eddy Interactions. *J. Atmos. Sci.*, **63**, 1569–1586.

Schwierz, C., S. Dirren, and H. C. Davies, 2004: Forced Waves on a Zonally Aligned Jet Stream. *J. Atmos. Sci.*, **61**, 73–87.

Sheng, J. and Y. Hayashi, 1990a: Estimation of Atmospheric Energetics in the Frequency Domain during the FGGE Year. *J. Atmos. Sci.*, **47**, 1255–1268.

Sheng, J. and Y. Hayashi, 1990b: Observed and Simulated Energy Cycles in the Frequency Domain. *J. Atmos. Sci.*, **47**, 1243–1254.

Simmons, A., S. Uppala, D. Dee, and S. Kobayashi, 2007: ERA-Interim: New ECMWF reanalysis products from 1989 onwards. *ECMWF Newsletter*, **110**, 25–35.

Simmons, A., J. Wallace, and G. Branstator, 1983: Barotropic wave propagation and instability, and atmospheric teleconnection patterns. *J. Atmos. Sci.*, **40**, 1363–1392.

Simmons, A. J. and B. J. Hoskins, 1978: The life cycles of some nonlinear baroclinic waves. *J. Atmos. Sci*, **35**, 414–432.

Slingo, J., K. Sperber, J. Boyle, J. Ceron, and M. Dix, 1996: Intraseasonal oscillations in 15 atmospheric general circulation models: Results from an AMIP diagnostic subproject. *Clim. Dynam.*, **12**, 325–357.

Stone, P. H., 1978: Baroclinic adjustment. *J. Atmos. Sci.*, **35**, 561–571.

Straub, K. and G. Kiladis, 2003: Extratropical forcing of convectively coupled kelvin waves during austral winter. *J. Atmos. Sci.*, **60**, 526–543.

Tiedtke, M., 1989: A comprehensive mass flux scheme for cumulus parameterization in large scale models. *Mon. Wea. Rev*, **117**, 1779–1800.

Ting, M., 1994: Maintenance of northern summer stationary waves in a GCM. *J. Atmos. Sci*, **51**, 3286–3380.

Tompkins, A. M., 2002: A prognostic parameterization for the subgrid-scale variability of water vapor and clouds in large-scale models and its use to diagnose cloud cover. *J. Atmos. Sci.*, **59**, 1917–1942.

Trenberth, K. E., 1984: Some Effects of Finite Sample Size and Persistance on Meteorological Statistics. Part 1: Autocorrelations. *Mon. Wea. Rev*, **112**, 2359–2368.

Trenberth, K. E., 1991: Storm tracks in the southern hemisphere. *J. Atmos. Sci.*, **48**, 2159–2178.

Trenberth, K. E., 1997: The definition of el niño. *Bull. Amer. Meteor. Soc*, **78**, 2771–2777.

Trenberth, K. E., et al., 2007: *Observations: Surface and Atmospheric Climate Change. In: Climate Change 2007: The Physical Science Basis. Contribution of Working Group I to the Fourth Assessment Report of the Intergovernmental Panel on Climate Change*. Cambridge University Press.

Valdes, P. and B. Hoskins, 1989: Linear stationary wave simulations of the time-mean climatological flow. *J. Atmos. Sci.*, **46**, 2509–2527.

Vautard, R. and B. Legras, 1988: On the Source of Midlatitude Low-Frequency Variability. Part II: Nonlinear Equilibration of Weather Regimes. *J. Atmos. Sci.*, **45**, 2845–2867.

W Randel, I. H., 1991: Phase speed spectra of transient eddy fluxes and critical layer absorption. *J. Atmos. Sci.*, **48**, 688–697.

Waliser, D., K. Lau, and J. Kim, 1999: The influence of coupled sea surface temperatures on the Madden–Julian oscillation: A model perturbation experiment. *J. Atmos. Sci*, **56**, 333–358.

Wang, X. L., V. R. Swail, and F. W. Zwiers, 2006: Climatology and Changes of Extratropical Cyclone Activity: Comparison of ERA-40 with NCEP–NCAR Reanalysis for 1958–2001. *J. Climate*, **19**, 3145–3166.

Washington, W. and C. Parkinson, 2005: *An Introduction to Three-Dimensionl Climate Modelling*. University Science Books, 354 pp.

Watanabe, M., 2005: On the presence of annular variability in an aquaplanet model. *Geophys. Res. Lett.*, **32**, L05 701, doi:10.1029/2004GL021869.